The Luminosity Function of Quasars at Redshifts Greater Than Four

Thesis by

Julia Dusk Kennefick

In Partial Fulfillment of the Requirements
for the Degree of
Doctor of Philosophy

California Institute of Technology
Pasadena, California

1996
(Submitted October 19, 1995)

Acknowledgements

I would like to thank my thesis advisor, George Djorgovski, for his guidance and encouragement over the last five years. It has been a privilege to work with someone who enjoys astronomy so much, and who dedicates so much of his time to his students. My thanks also go to Reinaldo de Carvalho, whose patience and wonderful sense of humor have made the last three years very enjoyable. Reinaldo, I promise I listened to all of, or at least most of, the advice you gave me. I owe a debt of gratitude to Dave Thompson. Thanks for showing me the ropes and being an all around good guy.

I also wish to thank the SKICAT development team, including Nick Weir, for giving me an introduction to this great package, and especially Joe Roden, for being so cheerful when helping me out with the little problems and for listening to my suggestions. Thanks also to the Sky Survey team, especially Neill Reid, and the scanning team at STScI. I would like to thank the staff at Palomar Observatory for making it a great place to observe.

Thanks to Betsy, Micki, Eric, Leonard, and Jeremy for all of their help on the DPOSS quasar project. Thanks also to Maarten Schmidt and Mike Irwin for helpful discussions. Limin Lu has my gratitude for his help with quasar absorption systems, as does Mike Pahre for letting me steal his completeness estimate programs.

I was supported in part by a fellowship from the National Physical Science Consortium. I wish to thank everyone at the NPSC, most of all Nan Snow. I also acknowledge support from the Kingsley Foundation.

Thanks to all of the graduate students in Robinson for their support and good cheer. Thanks especially to Dave and Lin for being such great office mates. My deepest thanks and warm wishes go to Todd and Suzanne for their friendship and encouragement.

I cannot express how much I owe to my mother and father. Thank you for your never failing love and support. Thanks also to Jim, Jo, and John for teaching me all that I know.

Most of all, thanks to Daniel.

Abstract

We present results from two multicolor surveys for quasars at $z > 4$, one utilizing a widefield photographic technique aimed at detecting bright quasars, and a second survey for faint quasars using CCD imaging.

In order to test our multicolor survey techniques, we also conducted a CCD survey aimed at recovering $z > 4$ quasars previously found in a photographic survey by Irwin, McMahon, & Hazard, but not fully documented in the literature. We report spectra, redshifts, finding charts, magnitudes and coordinates for ten such $z > 4$ quasars.

The bright quasar survey utilizes a digital version of the Second Palomar Sky Survey. The plates are taken in the photographic JFN bands and calibrated to the Gunn-Thuan gri system, making these data suitable for a multicolor search for quasars in the redshift range of $4.0 \lesssim z \lesssim 4.8$. Here we describe the search techniques and report the discovery of ten quasars. So far, we have covered an effective area of 681 square degrees over the magnitude range $16.5^m \leq r \leq 19.6^m$. Adopted selection criteria were applied objectively to the data sets, allowing the survey completeness to be estimated through Monte Carlo simulations, and quasar space densities at high redshift to be calculated. At our median redshift of $z = 4.35$, we find that quasar space densities are down by a factor of 7 from $z = 2.0$, and we see no evidence for luminosity dependent density evolution from $z = 2$ to $z = 4$.

The original motivation for the faint CCD survey was to detect quasar clustering at high-redshift in order to constrain theories of structure formation at early stages in the history of the universe. Therefore, the majority of data reported

are centered on fields containing known $z > 4$ quasars and a few are centered on blank control fields. We have selected a complete, rigorously defined sample of 39 quasar candidates from an area of 0.69 square degrees and have examined seven of these spectroscopically, confirming none as high-redshift quasars. However, we have surveyed enough area to constrain the $z > 4$ quasar luminosity function at $M_B < -24.0^m$ and discuss future prospects for detecting quasar clustering at high-redshift using these techniques. Additional color selected candidates outside the final sample were observed spectroscopically after an initial examination of the data. Among them we discovered a faint quasar with a peculiar spectrum at $z = 3.60$.

Contents

List of Figures

List of Tables

Chapter 1

Introduction

This thesis is concerned with investigating the quasar luminosity function at redshifts $z > 4$. In recent years, several groups have been successful at discovering significant numbers of quasars at very high redshift, some finding evidence for a decline in the space density of quasars beyond $z \sim 3$, while others advocate a constant density from $z = 2$ to $z = 4$. We have conducted two surveys for $z > 4$ quasars with the aim of addressing this apparent discrepancy.

The first quasar was identified in 1963 as the optical counterpart to the strong radio source 3C 273, with a redshift of 0.16 (Schmidt 1963). In the same volume of *Nature*, Hoyle & Fowler (1963) suggested that gravitational collapse could be a possible source of the tremendous energies of these strong radio sources. In December, 1963, the first *Texas Symposium on Relativistic Astrophysics* was held to discuss the nature of these quasi-stellar sources and their implications for the theory of general relativity (Robinson et al. 1965). A consensus was reached that quasars were a puzzle, but most considered the redshifts of quasars to be cosmological and, due to their variability, this meant that quasars were releasing large amounts of energy (10^{45} erg sec^{-1}) from a very small region. Nuclear reactions were considered an unlikely source, and the conclusion was made that some type of gravitational energy was required, giving impetus to the re-emergence of general relativity as a respectable field and helping institute the new field of relativistic astrophysics (Kennefick 1996a). Lynden-Bell (1969) was the first to suggest that

quasars are powered by accretion onto a massive black hole (or "Schwarzschild throat," as he called it), a theory that is still dominant today.

Quasars were immediately recognized as powerful cosmological tools. As the most luminous objects in the universe, they can be detected to greater distances or look back times than any other class of object. Many surveys for quasars have been conducted, and they are now known out to redshifts of $z \sim 5$ when the universe was only $5 - 10\%$ of its present age. Their mere existence places strong constraints on theories of galaxy and structure formation, as they would need some time to form and turn on (Turner 1991, Small & Blandford 1992, Haehnelt & Rees 1993). The evolution of the space density of quasars as given by the quasar luminosity function (QLF) has important implications for theories of galaxy formation and evolution, as a decline in the number of quasars might be an indication of not only the birth of quasars but of galaxies as well. Studies of quasar clustering probe the evolution of large scale structure over very large look back times. Quasars can also be used as probes of intervening matter throughout the history of the universe through studies of their absorption spectra. Observations of the gravitational lensing of quasars provide a measure of the masses of the intervening galaxies or clusters, and serve as probes of dark matter. Quasars themselves are good laboratories of relativistic astrophysics as we try to discern their nature. Good reviews on the current status of quasar studies are given in Hartwick & Schade (1990), Warren & Hewett (1990), Crampton (1991), Hewett & Foltz (1994), and Shaver (1995).

Systematic surveys for quasars have relied on their distinctive spectral energy distributions and broad emission lines. Sandage (1965) reported the discovery of the first radio quiet quasars. These objects had blue (ultraviolet excess) colors similar to the radio sources he was attempting to optically identify, but were not sources of radio emission. Sandage pioneered the first systematic surveys for quasars using the ultraviolet excess (UVX) method (Sandage & Veron 1965, Sandage & Luyten 1967). Quasar optical continuua can be approximately described by a power law ($f_\nu \propto \nu^\alpha$) with an index of $\alpha = -0.5$ to -1.0, resulting in a $(U - B)$ color that is much bluer than normal stars. A feature of UVX surveys

(as well as other color based surveys) is that the colors are affected by emission lines as they are redshifted through the various filters, resulting in a completeness that varies with redshift. The completeness can be calculated by combining the photometric errors of the survey with the expected variations of the $(U-B)$ color with redshift. Many surveys have been based on the UVX method, including the Palomar Bright Quasar Survey (Schmidt & Green 1983) and a more recent survey by Boyle et al. (1988) of eight UK Schmidt fields that was used to construct a sample of 420 faint ($B < 20.9^m$) quasars. The UVX method becomes ineffective at $z > 2.2$ when the Lyα line moves from the U to the B band. Koo & Kron (1982) extended the UVX method to larger redshifts by using four passbands, $UBRI$. Warren et al. (1991a) extended the multicolor method out to $z = 4.5$ using six passbands, u, v, b, r, or, and i, and the highest redshift quasar currently known, PC 1247+3406 at $z = 4.897$, was discovered in a multicolor transit survey (Schneider et al. 1991b).

Another common search technique is to use the broad emission lines seen in the spectra of quasars as a selection criterion in spectroscopic searches. Slitless spectroscopic surveys, where all objects in a field are detected as a low resolution spectrum, have typically used widefield Schmidt objective prism or grism (grating-prism) plates. In early surveys, the plates were inspected by eye, introducing selection biases that were difficult to characterize. More recent surveys have used objective, automated selection procedures to identify candidates, eliminating a major source of uncertainty. The Large Bright Quasar Survey (LBQS, Foltz et al. 1987) used APM scans of UK Schmidt direct and objective prism plates, resulting in the discovery of ~1000 quasars at $16^m < m_J < 18.5^m$. Crampton et al. (1989) have conducted a slitless survey at the CFHT which now consists of more than 300 objects complete to $m = 20.5^m$. The slitless technique is very effective at high redshifts, where the Lyα line and the drop blueward of the line caused by Lyα forest absorption is a strong signature. Osmer (1982) carried out a slitless survey optimized to find quasars at $3.7 < z < 4.7$ over 5 square degrees from their Lyα emission. From his null result, he concluded that there must be

a decline in the number of quasars beyond $z \sim 3$. Schneider et al. (1994) have concluded a CCD transit grism survey for quasars over 61.5 square degrees, recovering 90 quasars at $z > 2.7$, and found a decline in the number of quasars beyond $z = 2.7$ (Schmidt et al. 1995).

Usher & Mitchell (1978) have shown that samples of quasars selected by their variability can be nearly complete. Trevese et al. (1989) carried out a variability study in an area surveyed by other methods, showing that 70% of quasars are variable at the level of $\sigma = 0.1^m$. Hawkins & Véron (1993) have conducted a survey for quasars from their variability over 30 UK Schmidt plates, recovering 127 objects. Other survey techniques include proper motion studies, which are mainly useful in assessing the completeness of surveys utilizing other techniques, X-ray selected surveys (Henry et al. 1994), and, of course, radio selected surveys.

It became apparent early in the study of quasars that they are not distributed uniformly in space. This was established firmly by Schmidt (1968) who concluded that the density of quasars was increasing towards higher redshifts (pure density evolution). Mathez (1976) later showed that the quasar number-magnitude relation could also be interpreted as an increase in the luminosity of the quasars with redshift (pure luminosity evolution). Boyle et al. (1988) model the $z < 2.2$ QLF by a double power law function, and propose that a break seen at lower luminosities can be explained by pure luminosity evolution. However, Hewett et al. (1993) have analyzed a sample of 1049 quasars and AGN from the LBQS, adopting a modified form of the Boyle et al. (1988) double power law. They conclude that the shape of the QLF does change with redshift and cannot be explained by pure luminosity evolution. Hawkins & Véron (1995) have computed the QLF from a complete sample of 127 quasars selected on the basis of optical variability, and conclude that it can be modeled as a featureless single power law with constant slope out to $z \sim 3$. Both the Hewett et al. and Hawkins & Véron studies show positive evolution in the QLF out to $z = 2$, with a decreased rate or leveling off of the evolution beyond, out to redshifts of $z \sim 3$. It has now been well established that the apparent number of quasars increases out to $z \sim 2$, and then flattens off

between redshifts of 2 and 3. There is still some debate about what happens at redshifts beyond $z \sim 3$, with some groups seeing evidence for a decline in the space density (Warren et al. 1994, Schmidt et al. 1995) and others claiming that there is no decrease between $z = 2$ and $z = 4$ (Irwin et al. 1991).

The first quasar with a redshift larger than four was Q0046−293 with $z = 4.01$ (Warren et al. 1987a). This was the first of three quasars with $z > 4$ found in a wide field multicolor survey for high redshift quasars using APM scans of UK Schmidt photographic plates (Warren et al. 1991ab). The survey, using the u, b, v, or, r, and i bands, is effective over the range $2.2 \leq z \leq 4.5$ and covers two plate fields for an effective area of 46 square degrees. Selection biases for multicolor surveys can be very complicated, and Warren et al. (1994, refered to as WHO throughout) have made an extensive effort to model these biases using a Monte Carlo method employing synthetic quasar spectra with various spectral properties such as continuum slope and emission line strengths. Effects of quasar variability were also considered. The careful characterization of their survey allowed them to compute the QLF at $2.2 \leq z \leq 4.5$, which they model by a double power law function. They found that quasar space densities evolve from $z = 2.0$ to $z = 3.3$, with their being more bright quasars at $z = 3.3$ than at $z = 2.0$, but similar numbers of faint quasars. Space densities then decrease from $z = 3.3$ by a factor of $e^{-3.33(z-3.3)}$ (for $q_0 = 0.5$).

Shortly after the discovery of Q0046−293, Schmidt et al. (1987) announced the discovery of a quasar at $z = 4.04$ using a completely different technique, a CCD grism survey. The Palomar Transit Grism Survey (PTGS, Schneider et al. 1994), effective at $z > 2.7$ and covering 61.5 square degrees, has resulted in the discovery of nine quasars with $z > 4$. Schmidt et al. (1995, refered to as SSG throughout) have derived the $z > 2.7$ QLF from 90 quasars detected by their Lyα emission in the course of the PTGS. They found that quasar space densities decrease by a factor of 2.7 per unit redshift beyond z=2.7.

The WHO and SSG surveys covered a limited area, and given the steepness of the QLF at bright magnitudes, were not sensitive to intrinsically bright quasars at

$z > 4$. Irwin et al. (1991, refered to as IMH throughout) have reported preliminary results for a wide field multicolor photographic survey for bright $z \gtrsim 4$ quasars. The survey covers ~1000 square degrees in the UK Schmidt B_J, R, and I bands for an effective redshift range of $4.0 \lesssim z \lesssim 5.0$ and another ~1000 square degrees in B_J and R effective at $z \gtrsim 4.2$. The survey has resulted in the discovery of 27 quasars at $z > 4$ (Irwin, private communication). Assuming an estimate of their sample incompleteness, IMH concluded that the space densities of bright $z > 4$ quasars show no evolution from $z = 2$ to $z = 4$, and suggested that SSG could be missing some weak-lined objects from their sample. The apparent discrepancy could also be explained if the space densities of bright high redshift quasars evolve differently than the fainter ones, which is just what was found by WHO, who concluded that their survey results were consistent with the IMH result, assuming that the space density of bright quasars increases from $z = 2$ to $z = 3.3$ and then declines beyond $z = 3.3$, having similar space densities at $z = 2$ and $z = 4.3$.

An added complication to this picture is the selection biases encountered in multicolor searches for quasars. IMH have yet to report the characterization of their survey, making comparisons to other work difficult and unreliable. Another issue is the transformation from line flux or apparent magnitude to rest frame M_B magnitudes which are needed for comparison to surveys utilizing different techniques and to surveys at lower redshifts.

According to the work of WHO and SSG, there is a decline in quasar space densities beyond $z \sim 3$. There is still some disagreement as to whether the space densities of high redshift quasars with different luminosities evolve differently (luminosity dependent density evolution). This thesis is aimed primarily at answering this question through multicolor surveys for quasars at $z > 4$ at the bright and faint ends of the QLF. The same basic multicolor method is employed in all of the surveys discussed below and is illustrated in Figure 1.1. This technique uses the BRI or similar passbands to detect the presence of the Lyα line and the continuum drop across the line due to the Lyα forest. When stellar objects in the fields are plotted in $(B - R)$ *vs.* $(R - I)$ color-color diagrams, quasars stand out from

the locus of stars, making them relatively easy to select as candidates for follow-up sprectroscopy.

The following chapters report the results of three surveys designed to recover quasars at redshifts $z > 4$. Chapter 2 describes a 681 square degree survey for bright ($M_B < -27^m$) quasars using digitized scans of photographic plates from the Second Palomar Observatory Sky Survey (DPOSS). This survey is sensitive to roughly the same magnitude and redshift ranges as the IMH survey. A careful characterization of the survey has allowed us to compute reliable space densities for bright $z > 4$ quasars and fits in nicely with the SSG work. In Chapter 3, we report preliminary results for a 0.69 square degree CCD search for faint ($M_B < -24^m$) quasars originally designed to detect quasar marked protoclusters at $z > 4$. This area is just large enough to detect one quasar at these magnitudes, and has allowed us to place contraints on the number of faint quasars at $z > 4$.

Reliable quasar space densities are not the only outcome of such searches. The individual quasars discovered are desirable for use in other studies as discussed above. In order to increase the sample size of our protocluster search, we wanted to observe the unpublished quasars of IMH and engaged in a program designed to rediscover the quasars found in their multicolor survey. The results of this effort are reported in Chapter 4.

These chapters were written initially as papers for publication in astronomical journals, and some of the background material is repeated in the introductions to each chapter. In Chapter 5, we discuss some conclusions that can be drawn from these surveys.

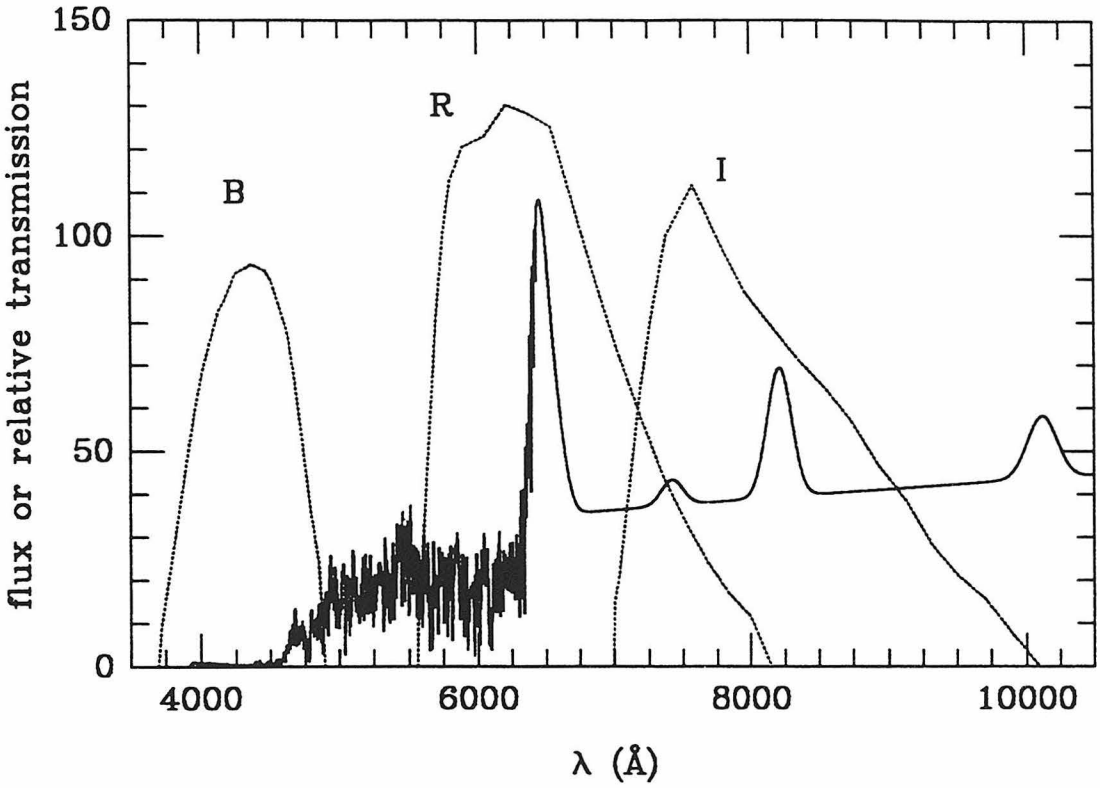

Figure 1.1: Model Quasar Spectrum with *BRI* Filter Curves

A model quasar spectrum with redshift $z = 4.3$ generated as described in Sec. 2.3.1 to aid in estimating the completeness of the surveys described in this text. *BRI* filter curves are also shown. Multicolor techniques at $z > 4$ are effective due to the lack of flux in the B band caused by the extreme absorption of the Lyα forest, giving a clear color-color signature.

Chapter 2

The DPOSS Search for z > 4 Quasars*

ABSTRACT

We are conducting a survey to identify $z > 4$ quasars using a digital version of the Second Palomar Sky Survey. The plates are taken in the photographic JFN bands and calibrated to the Gunn-Thuan gri system, making these data suitable for a multicolor search for quasars in the redshift range of $4.0 \lesssim z \lesssim 4.8$. Here we describe the search techniques and report the discovery of ten quasars (nine previously unknown). Coordinates, finding charts, and spectra for the quasars are given. In addition, we describe the adopted candidate selection procedures developed in light of these initial discoveries. The selection criteria have been applied objectively to the data sets, allowing us to estimate the survey completeness through Monte Carlo simulations, and calculate quasar space densities at high redshift. So far, we have covered 27 plate fields, for an effective area of 681 deg^2, over the magnitude range $16.5^m \leq r \leq 19.6^m$. Follow-up spectroscopy is complete for large portions of the color-color space. At our median redshift of $z = 4.35$, we find that quasar space densities are down by a factor of seven from $z = 2.0$, and we see no evidence for luminosity dependent density evolution from $z = 2$ to $z = 4$. We discuss how these findings compare to other surveys for quasars at high redshift.

---

* Adapted from two papers entitled "The Discovery of Five Quasars at $z > 4$ Using the Second Palomar Sky Survey," by J.D. Kennefick et al., 1995, *AJ*, 110, 78 and "The Luminosity Function of $z > 4$ Quasars from the Second Palomar Sky Survey," by J.D. Kennefick, S.G. Djorgovski, and R.R. de Carvalho, accepted for publication in the Astronomical Journal.

2.1 Introduction

Quasars provide a unique tool in studies of galaxy and large scale structure formation throughout the history of the universe. It became apparent early in the study of quasars that they are not distributed uniformly in space, but increase in number (or luminosity) towards higher redshifts (Schmidt 1968). The shape and evolution of the quasar luminosity function (QLF) at $z < 2.2$ has now been well established (Boyle et al. 1988, Hewett et al. 1993), showing a continued increase in the number of quasars out to these redshifts. It is reasonable to expect that the number of quasars should eventually start to decrease as we probe to earlier epochs, as these massive objects would need some time to form and turn on (Haehnelt & Rees 1993). Such a decline could mark the epoch of galaxy formation, and would constrain models of structure formation and the nature of quasars themselves.

To address this problem, several groups have undertaken searches for quasars in the range $2.2 < z < 5.0$ with much success. Schneider et al. (1994) have completed a 62 deg^2 CCD grism survey for quasars at $z > 2.7$, and have computed the QLF at $2.7 < z < 4.7$ from 90 quasars discovered through their Lyα emission (Schmidt et al. 1995, hereafter SSG). Warren et al. (1994, hereafter WHO) have computed the QLF at $2.2 < z < 4.5$ using quasars discovered in the course of a 47 deg^2 multicolor survey of UK Schmidt plates. While these two surveys were successful at finding quasars at $z > 4$, they were not sensitive to bright ($M_B < -27^m$) quasars at these redshifts due to their limited area coverage. Irwin et al. (1991, hereafter IMH) are conducting a $\sim$2500 deg^2 multicolor survey for bright ($R < 19^m$) $z > 4$ quasars using APM scans of UK Schmidt plates, and have discovered 27 objects at these redshifts (M. Irwin, private commumication).

The SSG and WHO groups do see evidence for a decline in the space density of quasars at redshifts beyond $\sim$3 while IMH argue for no evolution in the QLF from $z = 2$ to $z = 4$ and suggest that the discrepancy could be due to the possible insensitivity of the SSG grism survey to objects with weak Lyα emission. The

SSG and IMH surveys are sensitive to quasars of different luminosities, and so it has been suggested that the faint quasar population could evolve differently from the bright population, with their being relatively more bright objects at higher redshifts. However, IMH have yet to publish completeness estimates and selection probabilities for their survey, making any comparisons uncertain.

In order to establish the space density of bright ($M_B < -27^m$) quasars at $z > 4$, as well as provide additional $z > 4$ quasars for use in other studies, we have been conducting a multicolor survey using catalogs from the Second Palomar Observatory Sky Survey (POSS II; Reid et al. 1991). Digitization of POSS II is now in progress at STScI in collaboration with Caltech. These scans will constitute the Palomar-STScI Digital Sky Survey, or DPOSS (Djorgovski et al. 1992a; Lasker et al. 1992; Reid & Djorgovski 1993). This work has been greatly facilitated by the use of SKICAT, a software package designed to reduce the plate scans into object catalogs, classify the objects, and allow for the easy manipulation of the final catalogs (Weir 1994, Weir et al. 1995c). The POSS II plates are taken in the JFN bands and calibrated to Gunn-Thuan gri, making the data suitable for a multicolor search for $4.0 < z < 4.8$ quasars. The multicolor technique exploits the fact that at these redshifts the Lyα line lies in the r passband, and the continuum drop across the line due to the Lyα forest results in a large $(g - r)$ color, moving quasars outside of the stellar locus in color-color diagrams. So far, we have covered 27 DPOSS fields, for an effective area of 681 deg^2, and have discovered 10 quasars at $z > 4$. We are assigning a prefix of "PSS" to the quasar names to denote their discovery using the Palomar Sky Survey.

In Section 2.2, we outline the survey techniques, including catalog construction and calibration, and describe the candidate selection process developed in light of our initial findings. The new PSS quasars are reported in Section 2.2.5. The adopted objective selection procedures have allowed us to calculate our survey

completeness, which is given in Section 2.3. In Section 2.4, we compute the co-moving space density of quasars at $z > 4$ and compare our results to other surveys at these redshifts. These results are discussed further in Section 2.5. Following SSG, we adopt a $H_0 = 50$ km s^{-1} Mpc^{-1}, $q_0 = 0.5$ cosmology throughout.

2.2 The Survey

2.2.1 Survey Material

The photographic plates used in this work were obtained at the Palomar 48-inch Oschin Schmidt telescope during the course of POSS II, an all northern sky survey in three bands, JFN (Reid et al. 1991). Each plate covers a field of $6.6° \times 6.6°$ and the fields are spaced $5°$ apart, allowing for $\sim 1.6°$ of overlap between adjacent fields. The plates are processed into digitized scans containing 23040^2 pixels with a scale of $1.0''$/pixel.

To date, we have chosen candidates from 27 fields (Table 2.1). Fields were selected where plates of sufficient quality had been obtained in all three bands, JFN, and where $b > 30°$ in order to minimize contamination of the candidate lists by red stars. After correcting for plate overlaps, calibration spots, regions containing bright stars, and classification errors (discussed below), the total effective area covered by our survey so far is 681 deg^2.

2.2.2 Object Catalogs

Once the plates are scanned by STScI, the scans are processed into object catalogs at Caltech using the SKICAT software package (cf. Weir 1994 for a detailed description). The first step in plate processing is to perform the photographic density to intensity conversion by measuring the 16 sensitometry spots for the plate and interactively fitting a density-to-intensity curve. The scans are broken up into 2048^2 pixel overlapping 'footprints', and object detection and measurement is performed using FOCAS (Jarvis & Tyson 1979; Valdes 1982). Object detection is complete down to $\sim 20.5^m$ in r, $\sim 21.5^m$ in g, and $\sim 20.0^m$ in i.

For a multicolor survey of this type, it is important to have a very accurate, objective classification procedure to minimize the contamination of the candidate

lists by red galaxies. One of the major advantages of the SKICAT software is its application of machine learning techniques to the classification process in the form of decision tree algorithms. These algorithms are formed by using measurements of a training set of classified objects and inferring a set of rules for accurately classifying each example. The training sets were formed by matching CCD data, which have higher resolution and reach to fainter magnitudes, and so are more reliably classified, to a subset of the plate data, forming a set of classified plate objects. Separate sets of classification rules have been formed for the J and F plates. No classifier has yet been constructed for the N plates. Weir et al. (1995a) report that the decision tree classifiers achieve 90% completeness with 10% contamination down to $r \sim 19.6^m$ and $g \sim 20.5^m$. We have performed independent tests of the classification using CCD data obtained at the Palomar 200-inch telescope in plate areas different from that in which the classifiers were trained. Our results confirm the findings of Weir et al. Due to the large $(g - r)$ colors expected for the quasars, we rely on F plate classifications, and therefore adopt $r = 19.6^m$ as the limit of our survey.

2.2.3 Catalog Calibration

We use CCD exposures in the Gunn-Thuan (Thuan & Gunn 1976; Kent 1985) g, r, and i bands to calibrate the J, F, and N plate data, respectively (Figure 2.1). These bands were chosen to provide a reasonable match to the emulsion plus filter combinations of these plates. CCD images are obtained at the Palomar 60-inch telescope in a systematic observational program to provide calibration for DPOSS. On photometric nights, six to eight standard stars are observed with a range of air masses and colors. The consistency of the photometry for these nights is insured by requiring that the magnitude residuals of the standard stars show no temporal trends and have a standard deviation below 0.03^m.

CCD images of Abell clusters which lie in a survey field of interest (at this time mainly toward the North and South Galactic Poles) are obtained in each of the *gri* bands. These CCD images serve not only as calibration data, but also in the forming of training data sets for object classifiers (see above). Abell clusters are used in order to maximize the number of galaxies at a range of magnitudes so that the classifiers will be trained properly. Typical exposure times are 900 seconds in g and 600 in r and i. The CCD images are reduced using the CCDRED facility in IRAF, including debiasing, edge-trimming, and flat-fielding. The FOCAS package is used for object detection, measurement, and classification.

In order to apply appropriate color information from the CCD's to the plate, both g and r images are used in the calibration of J and F plates, and g and i for N plates. Galaxies are used in the calibrations in order to minimize the non-linear effects of the density-to-intensity transformation, as most of their pixels have densities in the linear portion of the density-to-intensity curve. We obtain a linear transformation from the instrumental J plate magnitudes to the calibrated g magnitudes, and from F to r and N to i. The slope in the magnitude transformation is always very close to one, implying that our initial density-to-intensity relation is taking out the nonlinearities in the plate data. FOCAS total magnitudes are used for the calibration, as they have been found to represent the most accurate measure of the true magnitude of an object (Weir 1994). Estimates of the systematic errors for the survey are given by Weir (1995b) as 0.05^m in r and 0.10^m in g. The random errors for each band have been calculated from the scatter in a plot of magnitude difference *vs.* magnitude of objects that lie in the overlap region of two adjacent plates. The median σ of the random errors, obtained from at least four plate pairs, are plotted as a function of magnitude in Figure 2.2. For a complete discussion of the plate photometry and accuracy, see Weir (1994) and Weir et al. (1995b).

For plates where we have been unable to obtain calibrating CCD data, if the survey field overlaps with a field where the calibration is known, the F plate data was calibrated to Gunn r by matching the objects in the overlap region of the two F plates and fitting a linear transformation to the data. For three fields, no calibrating CCD data was available for the field itself or surrounding fields. Calibrating CCD images are still being obtained, but in the mean time, galaxy counts were used to estimate the r band magnitudes for these three fields. Weir (1995b) shows that the level and slope of the number of galaxies per magnitude per deg^2 is very consistent between plates of a given passband, thus allowing us to roughly calibrate the data. This could introduce further systematic errors, but as no quasars have been confirmed in these three fields, it has little effect on the conclusions drawn below. The g and i band magnitudes for fields with no calibration were estimated by visually aligning the stellar loci of the data to those where CCD calibration is available.

2.2.4 Candidate Selection

Once final catalogs for each band are constructed for each survey field, the three catalogs are matched together by their right ascension and declination, forming a SKICAT "Matched Catalog," which can then be filtered using SKICAT catalog management tools. To allow us to assess our survey completeness, the candidate selection procedure has been made objective by setting rigid selection requirements for the candidates. For consideration as a candidate, we only require that an object be detected and classified as a star on the F plate, and have a magnitude of $16.5^m < r < 19.6^m$. We then consider four cases, one where the object has been detected on all three plates, and three where the object is missing from one of or both the J and N plates.

Colors are computed using both FOCAS total and core magnitudes. Total magnitudes are computed by adding the flux within an area that has been "grown"

to twice the detection area, while core magnitudes contain flux from the brightest 3×3 pixel region in the object. This 3×3 pixel region corresponds roughly to an equivalent aperture of radius ∼1.7″. The objects are divided into half-magnitude bins according to their total r magnitudes for plotting in color-color diagrams. In Figure 2.3, the top panel shows the color-color diagram using the total magnitude, while in the bottom panel, the core magnitude is used. As can be seen, the photometric scatter is greatly reduced by considering core colors, as would be expected due to the enhanced signal-to-noise.

For objects detected on all three plates, JFN, core color-color diagrams are constructed in half total-magnitude bins. The stellar loci are then aligned visually to a standard location based on well calibrated data, and objects are selected as candidates if they lie in specific areas of the color-color space. This selection area varies slightly with magnitude in accordance with the scatter due to photometric and classification errors. The left panel of Figure 2.4 contains color-color diagrams for the stellar objects contained in four survey fields, along with the candidate selection lines and the discovered PSS quasars. Objects are selected as candidates if they lie to the right of these lines in the color-color diagrams. The right panel contains the same selection lines along with colors computed from model quasar spectra over the range $4 < z < 5$ (discussed below). The selection areas were chosen on the basis of the position of the stellar locus, the positions of the quasars discovered so far in our survey, and the expected location of quasars in the space based on the model quasar colors, with the aim of including as many quasars as possible while keeping the number of candidates for follow-up spectroscopy reasonable. Images of the candidates from the J, F, and N plates are inspected to insure that their extreme colors are real and not due to some plate defect or object blending.

For objects detected on the J and F plates, but with no N plate detection, color-magnitude diagrams ($(g-r)$ *vs.* r)) are constructed and candidates selected

with $(g-r)$ colors greater than some limit. This limit again depends on magnitude and corresponds to the $(g-r)$ color of the vertical portion of the selection lines in Figure 2.4. An added requirement is that the objects have $r > 18^m$, since quasars at $4 < z < 5$ should have fairly small $(r-i)$ colors, and, if the objects are very bright on the F plate, they should be detectable on the N plate as well. Images of the candidates from each plate are then inspected before adding these objects to the candidate list.

Images of all objects detected on the F and N plates only within our considered magnitude range are inspected. They are with rare exception found to be mismatches. These objects account for only $\sim 0.1\% - 0.3\%$ of the objects classified as stars in F, assuring us that mismatching is a negligible source of imcompleteness for our survey. Those objects that truly have no J detection are then added to the candidate lists. Objects detected in F only make up $< 1.0\%$ of the objects classified as stars in F. Most of these objects are plate defects or dust particles. Some are high proper motion stars. We require that these objects have $r > 18^m$ for the reasons stated above. Those objects deemed real are also added to the candidate lists.

Although these selection criteria are somewhat arbitrary, they have been applied objectively, and so have allowed us to establish our selection function and completeness. After applying our selection criteria to the object catalogs, we have selected 170 objects for follow-up spectroscopy. Objects with JFN detections account for 155 of the candidates while there are nine with J and F detections, three with F and N detections, and three with F detections only. To date, we have obtained spectra for 85 of these candidates, although follow-up spectroscopy is complete for large portions of the selection area. The spectroscopy is discussed in more detail in Section 2.3.3. We have found ten quasars so far, nine of them previously unknown, and one known quasar, BRI 0103+00 (Smith et al. 1994b).

Nine of them were detected in JFN and one in F and N only. The locations of the quasars in color-color space are shown in the left panel of Figure 2.4.

2.2.5 The PSS Quasars

We are assigning the quasar names the prefix PSS to denote their discovery using the Palomar Sky Survey, followed by the truncated coordinates in the form hhmm+ddmm (J2000). Coordinates, redshifts, and r band magnitudes for all ten quasars are given in Table 2.2. The J2000 coordinates for the objects are estimated using astrometric solutions provided by STScI and are supposed to be good to 0.5″ r.m.s. accuracy (Lasker et al., *priv. comm.*). Finding charts produced by SKICAT for all ten quasars are given in Figure 2.5 and spectra for the PSS quasars are given in Figure 2.6. For a spectrum of the previously known quasar BRI 0103+0032, see Figure 4.2a. As a measurement of the discontinuity across the Lyα line, we have computed the continuum depression, parameterized by Oke & Korycanski (1982) as:

$$D_A = \langle 1 - [f_\nu(\text{observed})/f_\nu(\text{continuum})] \rangle,$$

for each spectrum as outlined by Schneider et al. (1989). D_A is measured between rest wavelengths of 1050Å and 1170Å. A power law was assumed to estimate the continuum flux. The value of D_A for each spectrum is listed in Table 2.2. The value of D_A for BRI 0103+0032 is taken from Smith et al. (1994b). The observed equivalent widths (EW) for the Lyα/N V blend were measured by summing the flux under the line. The continuum was defined by extrapolating the continuum redward of the line to the point on the blue side of the line where the flux drops off. Because of the difficulty in defining the continuum, the EW values (Table 2.3) are quite uncertain.

Candidate spectroscopy was performed at the Palomar 200 inch telescope using the Double Spectrograph (DBSP) and COSMIC II during the fall of 1994

and the winter and spring of 1995, all under nonphotometric conditions. Spectra of six candidates were obtained at the Keck 10 meter telescope in April of 1995 during very cloudy weather, but none were identified as quasars. Typical exposure times are 300 to 600 seconds, depending on the magnitude of the candidate. For the red side of the DBSP, we use a 316 l/mm grating with a dispersion of 3.06Å/pixel. This gives a resolution of 11Å with a 2″ slit. The camera covers the wavelength range 5000Å to 7500Å in order to catch the Lyα line in the redshift range $4.0 < z < 5.0$. Wavelength calibration, using a polynomial fit to He-Ne arc lines, has residuals of ~0.3Å. We use a 300 l/mm grating on the blue side of the DBSP (data not shown) with a dispersion of 2.17Å/pixel and a resolution of 11Å. It covers the wavelength range from 3350Å to 5100Å. With COSMIC II, we used a 300 l/mm grating with a dispersion of 3.2Å/pixel over the wavelength range 3640Å to 9850Å. Using a 1.5″ slit, this gave a resolution of 17Å. The COSMIC II spectra were wavelength calibrated using a fit to Hg-Ar arc lines, which has residuals of ~0.2Å. Notes on individual PSS quasars follow.

PSS 0059+0003: Two spectra totalling 600s were obtained on UT 1994 December 4 using the COSMIC II spectrograph and coadded. The resulting spectrum has been binned to further improve the signal-to-noise. A strong Lyα line as well as N V and C IV (not shown) are detected. We estimate a redshift of $z = 4.16$ for this object, based on these lines. The object shows strong absorption at $z_{abs} \sim z_{em}$.

PSS 0248+1802: Two spectra totalling 1200s were obtained on UT 1994 November 4 using the DBSP and coadded. A strong Lyα line blended with N V is seen as well as O I + Si II emission. We estimate a redshift of $z = 4.43$ for this object, based on the Lyα line.

PSS 1048+4407: Three spectra totalling 2100s were obtained on UT 1995 March 25 and 28 using the DBSP and coadded. A strong Lyα/N V blend is detected at 6625Å, giving this object a redshift of $z = 4.45$, the highest redshift so

far in our sample. This quasar was not detected on its J plate. Its colors (Figure 2.4, filled circle with arrow to the right, denoting a limiting $(g - r)$ color) are consistent with it being at a higher redshift than the other quasars. This quasar may also have characteristics of a BAL object (Turnshek 1988). Note the apparent broad absorption at ~7300Å. However, the spectrum does not cover enough range in wavelength to be certain. The continuum level is not well defined, making its D_A value and Lyα/N V EW uncertain.

PSS 1057+4555: Two spectra totalling 900s were obtained on UT 1995 March 25 using the DBSP. A strong Lyα/N V blend is detected at 6241Å. The Lyα/N V line is affected strongly by absorption, so the Si IV + O IV line at 7157Å has been used to assign it a redshift of $z = 4.10$. This object is the brightest so far in our sample with $r = 17.7^m$.

PSS 1317+3531: Three spectra totalling 2100s were obtained on UT 1995 March 25 and 28 using the DBSP. Lyα, N V, and O VI lines are detected. We estimate a redshift of $z = 4.36$ based on these lines. The quasar shows absorption at $z_{abs} \sim z_{em}$.

PSS 1430+2828: Two spectra totalling 1000s were obtained on UT 1995 January 28 using the DBSP. The coadded spectrum shows a strong Lyα line as well as O VI, N V, and O I + Si II. We estimate a redshift of $z = 4.31$ for this object, based on these lines. The object also shows strong absorption at $z_{abs} \sim z_{em}$.

PSS 1435+3057: Two spectra totalling 1000s were obtained on UT 1995 January 28 using the DBSP. The spectra were coadded and binned to improve the signal to noise. The spectrum shows weak Lyα/N V emission, and a pronounced continuum drop. The observed equivalent width of the Lyα/N V blend is only 52Å, which is right at the stated limit of the Schneider et al. (1994) grism survey. A redshift of $z = 4.35$ has been adopted with caution, based only on the apparent location of the Lyα line. This should be taken as an upper limit of the redshift of the object.

PSS 1438+2538: A 900s spectrum was obtained on UT 1995 March 27 using COSMIC II. The spectrum has been binned to improve the signal to noise. The object is a BAL quasar, with broad absorption at ~7150Å and ~7900Å. Lyα, N V, O I + Si II, Si IV + O IV, and C IV emission are seen. The redshift, estimated at $z = 4.24$, is made uncertain by the extreme absorption.

PSS 1443+2724: Two spectra totalling 1000s were obtained on UT 1995 January 29 using the DBSP. The spectra were coadded and binned to improve the signal to noise. The spectrum shows weak Lyα/N V emission as well as O I + Si II. A redshift of $z = 4.42$ has been adopted, based on the Lyα and O I + Si II lines. Absorption at $z_{abs} \sim z_{em}$ is seen. There is also a possible damped Lyα system at 6352Å, and strong unidentified absorption at 6804Å and 6967Å which may be C IV doublets at $z = 3.39$ and $z = 3.50$.

2.3 Completeness Estimates

2.3.1 Model Quasar Spectra

To estimate the completeness of our survey, we first need to calculate the probability of selecting quasars with different properties as candidates with our technique and adopted selection criteria. We have followed the basic Monte Carlo methodology of WHO by generating model quasar spectra of differing line strength, redshift, and magnitude, and testing if they meet our selection criteria. In generating these spectra, we assumed a power law continuum of the form $f_\nu \propto \nu^\alpha$, with $\alpha = -0.5$, and Gaussian profile emission lines of FWHM=5000 km s^{-1}. Rest frame equivalent widths were taken from Wilkes (1986) for Lyα, N V, Si IV, C IV, and C III, and from Warren et al. (1991a) for O VI. Following the methodology of WHO, we have considered three line strength cases by varying the strength of the Lyα line, but keeping the EW ratios fixed. Wilkes (1986) gives the rest frame EW of Lyα of a typical quasar as 65Å. In case A we take half this value, in case B we adopt the typical value, and in case C we use twice the typical value. We have not allowed for a variation in the continuum slope, mainly due to the difficulty in measuring the value of the slope of our quasar continua from their discovery spectra. However, we have investigated the effect of varying the slope on the model quasar colors and found that it has a noticable effect only on the $(r-i)$ color and is small compared to the effect of varying the line strength.

The most defining characteristic of a quasar at $z > 4$ is the continuum drop blueward of Lyα due to intervening absorption. We have modeled the absorption due to the Lyα forest ($1.0 \times 10^{12} < N_{HI} < 1.6 \times 10^{17}$) by assuming that the number density of absorbers varies as

$$\frac{dN}{dz} \propto (1+z)^\gamma \tag{2.1}$$

where $\gamma = 2.75$ (Lu et al. 1991) and a normalization chosen so that D_A=0.60 at $z = 4.5$. This normalization was chosen based on the D_A values of quasars at $z > 4$ quoted in the literature (Figure 2.7) For the Lyman-limit systems ($1.6 \times 10^{17} < N_{HI} < 1.0 \times 10^{20}$), the number of absorbers was again assumed to vary according to Eq. (2.1), but with $\gamma = 1.55$ and a normalization of $dN/dz = 0.27$ at $z = 0$ (Storrie-Lombardi et al. 1994). For each type of absorber, the column density distribution was taken to be a power law:

$$N(N_{HI}) \propto (N_{HI})^{-\beta} \tag{2.2}$$

where β=1.55 (Lu et al. 1995). The Doppler width (b) distribution is taken to be a Gaussian with mean $\bar{b} = 23$ km s^{-1} and $\sigma = 8$ km s^{-1}, but truncated at b = 15 km s^{-1} (Lu et al. 1991). For each absorber, the first 31 lines of the Lyman series were included. Lyman continuum absorption of the form

$$f = f_0 e^{-\tau} \tag{2.3}$$

was also included, where

$$\tau = \left(\frac{\lambda}{\lambda_{abs}}\right)^3 \frac{N_{HI}}{1.68 \times 10^{17}} \quad , \tag{2.4}$$

λ_{abs} is the wavelength of redshifted 912Å for the absorber, and $\lambda < \lambda_{abs}$. Given the uncertainty in the value of D_A due to the Lyα forest at these redshifts, we have chosen not to include damped systems as they are sufficiently rare and so have little effect on the broadband colors of the quasars (Moller & Warren 1991).

2.3.2 Selection Probabilities

For each line strength case and at each redshift $4 < z < 5$ with $\Delta z = 0.1$, 50 quasar spectra were constructed with different absorption-line properties based on the above distribution functions, for a total of 1650 model quasar spectra. In

order to compute the probability that a quasar of a given line strength, redshift, and magnitude would be selected as a candidate, we must add appropriate random errors to the theoretical colors. Because the plate data from different bands can be taken at times separated by as much as eight years, we have also chosen to include quasar variability. The variability was modeled using a simple Gaussian distribution with $\sigma_{var} = 0.1^m$, based on the work of Hook et al. (1994), who show a slight trend toward decreasing variability with higher redshifts and brighter absolute magnitudes.

For each model spectrum, and at each magnitude, $16.5^m < r < 20.0^m$, $\Delta r = 0.1^m$, g and i band magnitudes were computed in accordance with the colors of that spectrum. The broadband magnitudes were adjusted separately for variability by adding a value taken randomly from the Gaussian distribution described above. Random photometric errors were then added based on the error distributions of Figure 2.2. Broadband colors were computed for each spectrum by convolving the spectrum with the JFN filter curves and calibrating to gri with a Gunn-Thuan standard. The colors computed from case B model quasar spectra are shown in the right panel of Figure 2.4 for three different magnitudes ($r = 17.3^m, 18.3^m$, and 19.3^m) and over the range $4 < z < 5$. The model quasar colors show good agreement with our discovered PSS quasars, lending confidence that the model quasar spectra are a good representation of the quasar population at these redshifts.

The selection criteria described in Sec 2.2.4 were applied to the final colors and the percentage of objects that met the selection criteria counted as a function of redshift, magnitude, and line strength. These selection probabilities are plotted in Figure 2.8a. For case B, a quasar of average line strengths (middle diagram), the probability of being selected as a candidate rises rapidly from $z = 4.0$ to $z = 4.2$ and remains high out to $z = 5$. The probabilities vary little with r over the range of interest, although there is some decrease after $r > 19.0^m$ when the selection

criteria become more restrictive due to increased photometric scatter. Comparing the three line strength cases, it is apparent that objects with stronger lines are more likely to be selected, as would be expected due to the increased flux in the r band from the Lyα/NV line.

2.3.3 Spectroscopic Completeness

As mentioned briefly above, we have obtained spectra for half of the objects that meet our selection criteria. Candidates are ranked on the basis of their magnitudes and colors. This means that for large portions of the color-color space, we are complete or nearly complete spectroscopically, while in other areas, we are only 50% complete or even less than 10% complete. In order to take this into account, for each half-magnitude bin, we have divided the color-color space into different spectroscopic completeness areas. These areas are too cumbersome to show in detail here, but can be roughly described by Figure 2.9, where the selection area has been divided into four sub-areas, numbered 1-4. In area 1, we are greater than 90% complete spectroscopically for all magnitude ranges. For areas 3 and 4, we are less than 10% complete for all magnitude ranges. For area 2, our spectroscopic completeness goes from 100% at the brightest magnitudes to $\sim$10% at the faintest magnitudes, with an average of $\sim$50% completeness over the whole range.

We shall define the "spectroscopic probability" in a given area of the color-color space as the ratio of the actual number of candidate spectra that have been taken in that area to the number of candidates selected for spectroscopy in that area. A model quasar is assigned the spectroscopic probability corresponding to the area in which it falls. Model quasars with limiting $(g - r)$ colors (not detected on the J plate) are assigned a spectroscopic probability of 1 because we have obtained spectra for all three of the candidates with only F and N detections, confirming one as a quasar. These spectroscopic probabilities are multiplied

by the selection probabilities described above (Figure 2.8a), to arrive at a final detection probability for the model quasars. These final detection probabilities, p, are shown in Figure 2.8b as a function of line strength, magnitude, and redshift. Because most model quasars have colors that put them in area 1 of Figure 2.9 (see Figure 2.4 for model quasar colors) where we are spectroscopically complete, the detection probabilities (Figure 2.8b) do not differ significantly from the selection probabilities (Figure 2.8a). The detection completeness is most affected at fainter magnitudes, where our spectroscopic incompleteness becomes significant in area 2. This is more important at lower redshift, as these quasars are more likely to fall in area 2 due to their lower $(g - r)$ colors.

2.4 The z>4 Quasar Luminosity Function

2.4.1 Absolute Magnitudes

In order to compute the QLF at $z > 4$ and compare it to the QLF found from surveys at $z < 2.2$, as well as other surveys at very high redshift, we wish to transform the apparent r magnitudes of the quasars to their rest frame M_B magnitudes. Throughout this transformation, we will assume that the quasar continua have a power law spectrum of the form

$$f_\nu \sim \nu^\alpha. \tag{2.5}$$

We will first find a relation for M_B expressed in terms of the AB magnitude (Oke 1974) at the wavelength $\lambda_{obs} = 1450(1+z)$, where

$$AB(\lambda) = -2.5 \ \log \ f_\nu(\lambda) - 48.60. \tag{2.6}$$

We have adopted a cosmology of $H_0 = 50$km s^{-1} Mpc^{-1}, $q_0 = 0.5$ to aid in the comparison to other surveys. The bolometric luminosity distance is then $(c/H_0)A(z)$ where

$$A(z) = 2(1 + z - \sqrt{1+z}). \tag{2.7}$$

Following the methodology of SSG, we have

$$\begin{aligned} M_{AB}(\lambda_{obs}/(1+z)) = AB(\lambda_{obs}) - 5 \ \log[(c/H_0)A(z)/10pc] \\ + 2.5 \ \log(1+z), \end{aligned} \tag{2.8}$$

which is independent of α because the absolute magnitude refers to the same rest frame wavelength as the observed apparent magnitude. Using Eq. (2.5), we can express $M_{AB}(1450)$ in terms of $M_{AB}(4400)$ by

$$M_{AB}(4400) - M_{AB}(1450) = -2.5 \ \alpha \ \log\left(\frac{1450}{4400}\right). \tag{2.9}$$

Combining Eqs. (2.8) and (2.9) and denoting $AB(1450(1+z))$ as AB_{1450} gives

$$M_{AB}(4400) = AB_{1450} - 5\ \log[(c/H_0)A(z)/10pc] + 2.5\ \log(1+z) + 1.20\alpha. \quad (2.10)$$

SSG report that convolution of an $\alpha = -0.5$ power law spectrum with the B-filter response gives an offset of

$$M_B = M_{AB}(4400) + 0.12. \quad (2.11)$$

The final expression relating M_B to AB_{1450} is then

$$M_B = AB_{1450} - 5\ \log[(c/H_0)A(z)/10pc] + 2.5\ \log(1+z) + 1.20\alpha + 0.12. \quad (2.12)$$

For quasars at $4 < z < 5$, the relation between m_r and AB_{1450} cannot be found analytically by assuming a simple power law spectrum because Lyα/NV emission and the forest absorption blueward of the line lies in the r band at these redshifts. This relation will also be dependent on z, as the Lyα line moves through the r band with increasing redshift. In computing this relation, we have employed the model quasar spectra discussed in Sec. 2.3.1. For each model spectrum, the flux at 1450(1+z) was measured and its AB magnitude computed via Eq. (2.6). The model spectrum and the spectrum of a Gunn-Thuan standard were then convolved with the F-band filter and m_r for the spectrum was computed. This "k-correction," denoted by k_1, is then

$$k_1 = AB_{1450} - m_r. \quad (2.13)$$

We can then write the total k-correction, k_{eff}, as

$$k_{eff} = k_1 + 1.20\alpha + 0.12, \quad (2.14)$$

and then the final expression relating M_B and m_r is

$$M_B = m_r - 5\ \log[(c/H_0)A(z)/10pc] + 2.5\ \log(1+z) + k_{eff}. \qquad (2.15)$$

The relation is also dependent on the Lyα line strength, so the average k_1 for each line strength case as a function of z was found and is shown in Figure 2.10. The k_1 values remain small from $z = 4.0$ to $z = 4.5$, but then become increasingly negative as the Lyα line leaves the r band. This has the effect, that while the multicolor method employed in this survey is in principle sensitive to objects with $z > 4.6$, the objects would need to be intrinsically bright to have $m_r < 19.6^m$, and hence be included in the survey.

For each of the PSS quasars, the M_B was computed from m_r by first finding the value of k_1 from its spectrum and using this value in Eq. (2.15) assuming $\alpha = -0.5$. These values are given in Table 2.3. This procedure is equivalent to measuring the AB_{1450} flux of the quasar and using Eq. (2.10). Since the spectra were taken in nonphotometric weather, this has the effect of flux calibrating the spectra by their r magnitudes.

2.4.2 Space Densities

Now that we have computed detection probabilities and absolute B magnitudes for the quasars, we can calculate space densities using the $1/V_a$ estimator (e.g., Avni & Bahcall 1980), where V_a, the available volume, is the comoving volume over which the quasar could have been detected by this survey. We have done this using two methods as outlined by WHO. Method 1 involves assuming that the survey is comprised of a number of subsurveys, each of interval $\Delta z = 0.1$ and $\Delta m_r = 0.1$ (the resolution of the detection probabilities) and for each line strength case. The area of each subsurvey is then the actual area multiplied by the detection probability $p(z, m_r)$. The space density is computed as $\sum 1/\int p(z, m_r) dV_a$

and the error as $[\sum 1/\int(p(z,m_r)dV_a)^2]^{1/2}$. Using method 2, one first corrects for incompleteness by assuming that for each object found, the true number is $1/p$. The space density is then $\sum 1/pV_a$ and the error $[\sum 1/(pV_a)^2]^{1/2}$.

The detection probabilities, p, are dependent on the Lyα line strength. Therefore, in order to assign the quasars a detection probability, we must decide which line strength case they belong to. Quasars at these redshifts suffer from strong Lyα absorption, so the criterion we have used to assign the quasars a case is their k_1 value. The k_1 value of each quasar as calculated from its spectrum was compared to the k_1 values computed from the model quasar spectra (Figure 2.10). The case whose k_1 was closest to that of the quasar at the quasar redshift was adopted and is listed in Table 2.3. The adopted line strength case corresponds well with the Lyα/NV EW (also given in Table 2.3), with the possible exception of PSS 0059+0003.

Space densities computed using the two methods described above are given in Table 2.4 along with their errors for two M_B ranges. The two methods give similar results, although Method 2 has larger errors. Space densities from method 1 are plotted in Figure 2.11 (solid squares) versus the median M_B for the quasars in the bin. Also shown is a $z = 2$ luminosity function from Boyle (1991). We find that the density of bright ($M_B < -27^m$) quasars decreases by a factor of $\sim$7 from $z = 2$ to $z = 4.35$ (our median redshift). Hewett et al. (1993), in analyzing the Large Bright QSO Survey, have calculated space densities at $z = 2$ that are a factor of $2 - 3$ lower than that of Boyle (1991). Comparing our work with that of Hewett et al. gives a decline of a factor of $\sim$3 from $z = 2$ to $z = 4.35$.

In the above discussion, we have ignored the fact that one (and possibly two) of the quasars in our sample shows characteristics of a BAL. Because BAL's suffer from strong absorption, continuum absorption causes the flux blueward of $(1 + z_{quasar})912$Å to drop to essentially zero. This gives the BAL a more extreme $(g-r)$ color, making it easier to detect. The BAL object, PSS 1438+2538, does have

the lowest computed detection probability (p=0.23), suggesting that its detection probability could be underestimated. If we assume that $p(z) = 1$ for this object and recompute the space density using Method 1, we find $\Phi(-26.5^m < M_B < -27.5^m) = 4.7 \pm 1.7 \times 10^{-9}$ Mpc^{-3} mag^{-1}, which is well within the errors of the value reported in Table 2.4.

2.4.3 Comparisons with Other Surveys

SSG derive the QLF in the redshift range $2.75 < z < 4.75$ based on 90 quasars (9 at $z > 4$) detected through their Lyα emission in the Palomar Transit Grism Survey (Schneider et al. 1994). They conclude that the space density for $M_B < -26^m$ decreases by a factor of 2.7 per unit redshift beyond $z = 2.7$. In Figure 2.11, we plot the points from SSG (their Figure 5) scaled to our median redshift of $z = 4.35$ (open squares). Our survey (Figure 2.11, filled squares) agrees with the SSG survey remarkably well, especially considering the very different techniques employed. One can even imagine that the points follow a curve with the same shape as the $z = 2$ QLF, scaled to lower space densities. In Figure 2.12, we plot cumulative space densities for our survey (histogram and solid squares) as well as the SSG cumulative space density for $M_B < -26^m$ at $z = 4.35$ (see SSG, Eq. 36) (open star). Both surveys show a decrease in the density of objects from $z = 2$ to $z = 4.35$.

WHO have performed a six-band multicolor survey for quasars in the range $2.0 < z < 4.5$. This survey covers an effective area of 43.0 deg^2 down to $m_{or} = 20.0^m$ and contains 86 quasars in their complete sample, one with $z > 4$. They derive the QLF over the redshift range $2.0 < z < 4.5$ and find a decrease in the space density beyond $z = 3.3$. The QLF is modeled by a double power-law function and best fit parameters are given (Warren et al. 1994). The $z > 3.3$ QLF is parameterized by assuming that it has the same shape as that at $z = 3.3$, but scaled

down by a factor of $e^{-3.33(z-3.3)}$ ($q_0 = 0.5$). In Figure 2.12, we represent the WHO survey at $z = 4.35$ (open square) by calculating the $M_B < -26.5^m$ cumulative space density at $z = 3.3$ using the WHO model, scaling by the appropriate factor, and transforming to our adopted cosmology. The $M_{C(1216)}$ used by WHO was transformed to M_B using $M_B - M_{C(1216)} = -0.60$ as given by SSG. The WHO point shows a drop in the space density of quasars from $z = 2$ to $z = 4$, and agrees well with both our survey and the SSG survey. Taking a simpler approach, if we assume that our survey and the WHO survey have similar sensitivities at $z > 4$, then, given that we cover 16 times the effective area, we should find 16 ± 4 quasars. We found 10, which is consistent within the Poissonian errors. It should be stressed that while this consistency is heartening, given that the WHO complete sample contains only one $z > 4$ quasar, it is very uncertain.

IMH are conducting a multicolor survey for bright ($R < 19^m$) $z > 4$ quasars using APM scans of UK Schmidt plates. They have surveyed ~ 2500 deg^2, and discovered 27 quasars at $z > 4$, with a median redshift of $z = 4.25$ (M. Irwin, private communication). IMH report a cumulative space density of 6×10^{-9} Mpc^{-3} for $M_B < -27.8^m$. We plot this point in Figure 2.12 (open circle). As can be seen in Figure 2.12, IMH see no evidence for a decline in the space density of quasars from $z = 2$ to $z = 4.3$, in direct contrast to our findings. The survey techniques employed by IMH are almost identical to our own, covering similar redshift and magnitude ranges. IMH cover $\sim$3 times our survey area and have identified $\sim$3 times the number of quasars. This would lead one to presume that our surveys are in fact finding similar space densities, but are interpreting the results very differently. A full characterization of the IMH survey is needed before any firm conclusions can be made.

2.5 Discussion

We have successfully conducted a search for $4 < z < 5$ quasars using digitized scans of plates from the Second Palomar Sky Survey. This search was greatly facilitated by the use of SKICAT, a software package that enabled the reduction of the plate data into object catalogs, the accurate classification of the detected objects, and the easy manipulation of the final catalogs. So far we have surveyed 27 fields for an effective area of 681 deg^2. We have discovered ten quasars at $z > 4$, nine previously unknown, comprising $\sim$20% of the currently known $z > 4$ quasar population.

After defining objective selection criteria, we were able to estimate our survey completeness by computing the detectability of quasars as a function of apparent magnitude, redshift, and line strength using model quasar spectra. Photometric errors, quasar variability, and the effect of intervening absorption were included. Quasar space densities at $z = 4.35$, our median redshift, were calculated, showing a decrease by a factor of $\sim$7 from $z = 2$ for $M_B < -27^m$.

These results were compared to other surveys for high-redshift quasars. They agree remarkably well with the results of SSG, and are consistent with the results of WHO. However, our results seem to be in direct constrast to the results of IMH, who see no evidence for a decline in the space density of quasars from $z = 2$ to $z = 4$. Our survey and the IMH survey use a similar (almost identical) technique, and are sensitive to the same redshift and magnitude ranges. The two surveys are in fact recovering roughly the same number of quasars per effective area covered. This would suggest that the two surveys are finding similar space densities of quasars at $z \approx 4.3$, but are interpreting the results in a very different way. We believe the difference may be due to the way in which M_B magnitudes are computed, as many assumptions must be made in the transformation from apparent r band magnitudes to rest frame M_B magnitudes at these redshifts. We

await the characterization of the IMH survey in hopes that this discrepancy can be explained.

SSG and WHO conclude that there is a peak in the comoving space density of quasars at $z \sim 3$, with a decline at higher redshifts. Our results are consistent with these findings, and extend this apparent decline to brighter magnitudes. We see no evidence that the QLF at faint magnitudes ($M_B > -27^m$) evolves differently from the QLF at brighter magnitudes, eliminating the need to invoke luminosity dependent density evolution from $z = 2$ to $z = 4$. The decline in the density of quasars at $z > 3$ could indicate a peak in the quasar population at these redshifts and possibly mark the epoch of peak structure and galaxy formation in the universe. However, Fall & Pei (1993) argue that obscuration by dust could cause optical surveys for quasars at $z = 3$ to miss $10 - 70\%$ of bright quasars, and at $z > 4$, the number could be as high as 90%. For extreme obscuration, they find that the number of quasars missed could increase by a factor of seven from $z = 2$ to $z = 4$, which is the apparent decrease that we find. As this is their extreme case, dust obscuration could just account for the decrease that we are seeing. However, their results at $z = 4$ are extrapolations from $z = 3$, making this interpretation even more tentative.

Whether this apparent decline in the number of quasars at $z > 3$ is caused by a real decrease in the space density or by obscuration, it is clear that the study of quasars at these epochs will lead to a better understanding of these objects as well as the universe at its earliest stages. To this end, we are continuing this search by proceeding with candidate spectroscopy for these fields as well as from additional DPOSS fields. This will provide a larger sample of bright, high redshift quasars for use in absorption line studies, lensing studies, etc., while further constraining the density of quasars at $z > 4$.

Table 2.1: Survey Fields

Field	Central Coordinates α (B1950)	δ (B1950)
679	00 00	+10
751	00 00	+05
752	00 20	+05
539	00 21	+20
826	01 00	+00
615	02 40	+15
480	02 56	+25
834	03 40	+00
620	04 20	+15
314	09 06	+40
500	10 16	+25
436	10 21	+30
264	10 44	+45
268	11 40	+45
575	12 57	+20
382	13 12	+35
577	13 39	+20
384	14 00	+35
385	14 24	+35
447	14 34	+30
512	14 40	+25
386	14 48	+35
448	14 57	+30
889	22 00	+00
820	23 00	+05
893	23 20	+00
894	23 40	+00

TABLE 2.2: Coordinates, redshifts, r magnitudes, and D_A for the quasars

QSO	α (J2000)	δ (J2000)	z	r	D_A
PSS 0059+0003	00 59 22.8	+00 03 01	4.16±0.03	19.5±0.2	0.58
BRI 0103+0032	01 06 19.2	+00 48 22	4.43±0.01	19.1±0.2	0.62
PSS 0248+1802	02 48 54.3	+18 02 50	4.43±0.03	18.4±0.2	0.61
PSS 1048+4407	10 48 46.6	+44 07 13	4.45±0.03	19.3±0.2	0.71
PSS 1057+4555	10 57 56.4	+45 55 52	4.10±0.05	17.7±0.1	0.53
PSS 1317+3531	13 17 43.2	+35 31 31	4.36±0.03	19.1±0.2	0.62
PSS 1430+2828	14 30 31.7	+28 28 34	4.31±0.02	19.3±0.2	0.55
PSS 1435+3057	14 35 23.6	+30 57 22	4.35±0.05	19.3±0.2	0.59
PSS 1438+2538	14 38 35.6	+25 38 32	4.24±0.05	19.5±0.2	0.57
PSS 1443+2724	14 43 31.2	+27 24 37	4.42±0.05	19.3±0.2	0.65

TABLE 2.3: M_B, p, and adopted spectral type

QSO	z	M_B	p	type	Lyα/NV EW
PSS 0059+0003	4.16	−26.7	0.39	C	398 Å
BRI 0103+0032	4.43	−27.4	0.78	B	463 Å
PSS 0248+1802	4.43	−28.0	0.97	B	483 Å
PSS 1048+4407	4.45	−27.3	0.70	B	424 Å
PSS 1057+4555	4.10	−28.5	0.47	B	381 Å
PSS 1317+3531	4.36	−27.3	0.67	B	560 Å
PSS 1430+2828	4.31	−26.8	0.76	C	685 Å
PSS 1435+3057	4.35	−27.4	0.40	A	52 Å
PSS 1438+2538	4.24	−27.2	0.16	A	216 Å
PSS 1443+2724	4.42	−27.5	0.47	A	162 Å

Table 2.4: Quasar Space Densities at $4.0 \leq z \leq 4.5$ (Mpc^{-3} mag^{-1}), $\mathrm{H}_0 = 50$ km s^{-1} Mpc^{-1}, $\mathrm{q}_0 = 0.5$

M_B	Method 1	Method 2
-26.5 to -27.5	$(5.6 \pm 2.1) \times 10^{-9}$	$(5.4 \pm 3.2) \times 10^{-9}$
-27.5 to -28.5	$(5.5 \pm 3.9) \times 10^{-10}$	$(5.1 \pm 5.1) \times 10^{-10}$

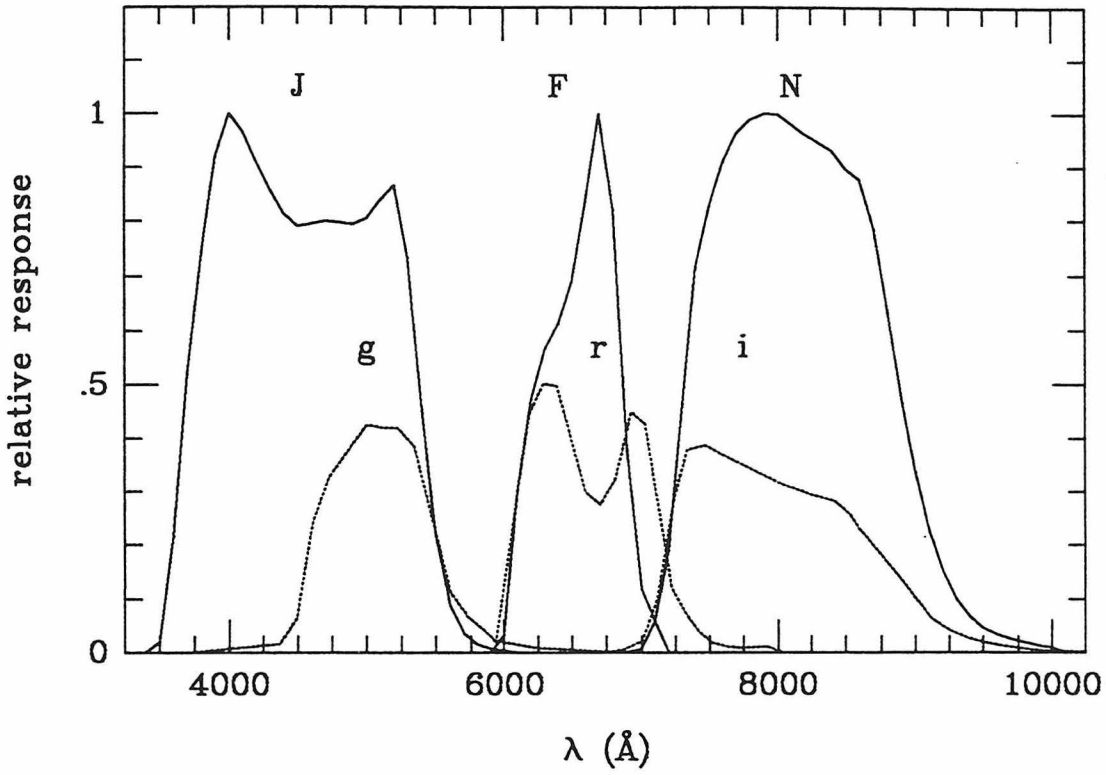

Figure 2.1: Plate and CCD Bandpasses

The relative transmission of the J, F, and N plate plus filter combinations and the Gunn-Thuan g, r, and i system.

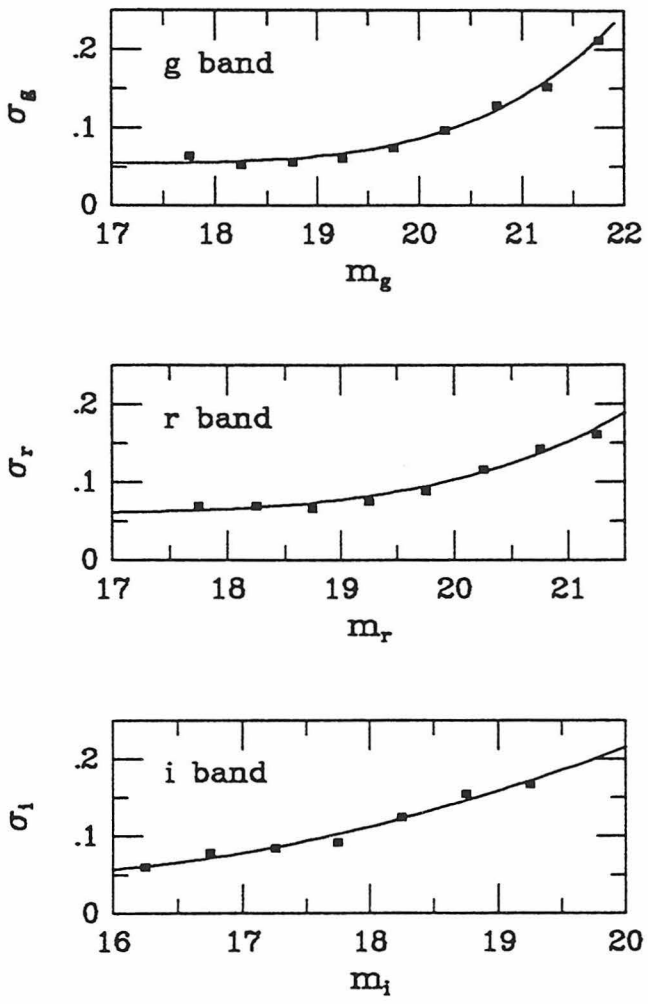

Figure 2.2: Random Plate Errors

The median σ in magnitudes of the random plate errors for each band as a function of magnitude.

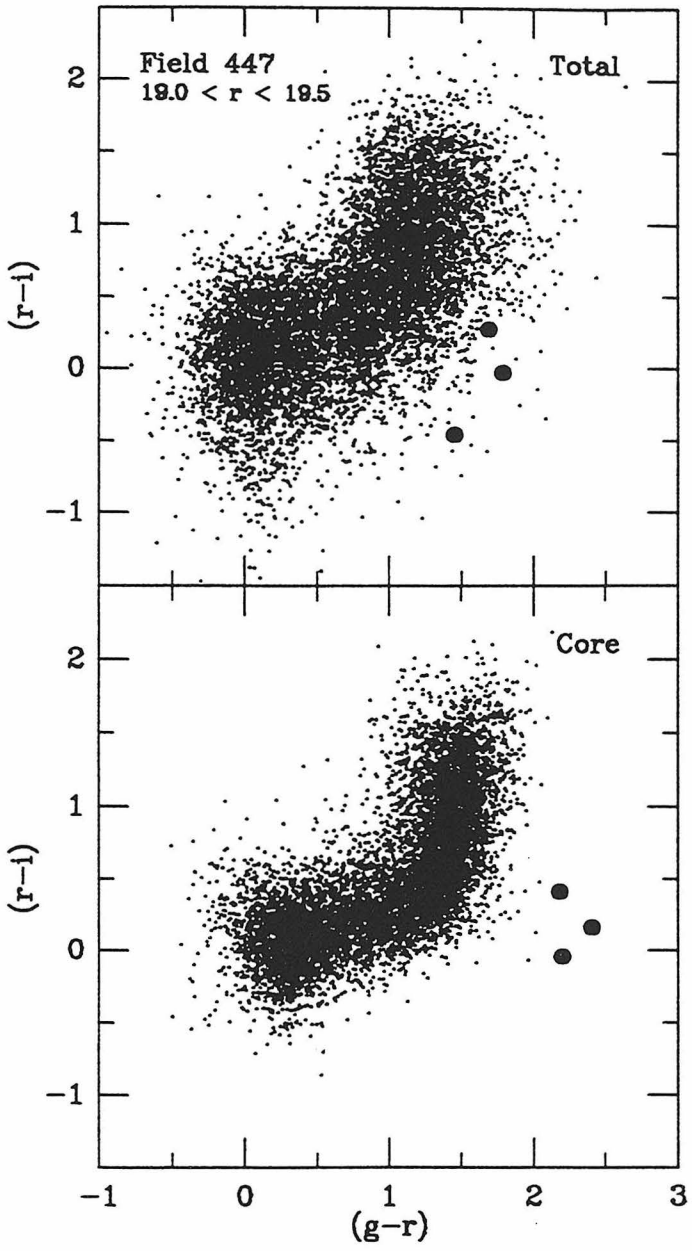

Figure 2.3: Comparison of Total and Core Colors

Color-color diagrams for the 447 field in the range $19.0^m < r < 19.5^m$ using total (top) and core (bottom) magnitudes as described in the text. The reduced scatter in the core diagrams makes quasars (large filled circles) much easier to identify.

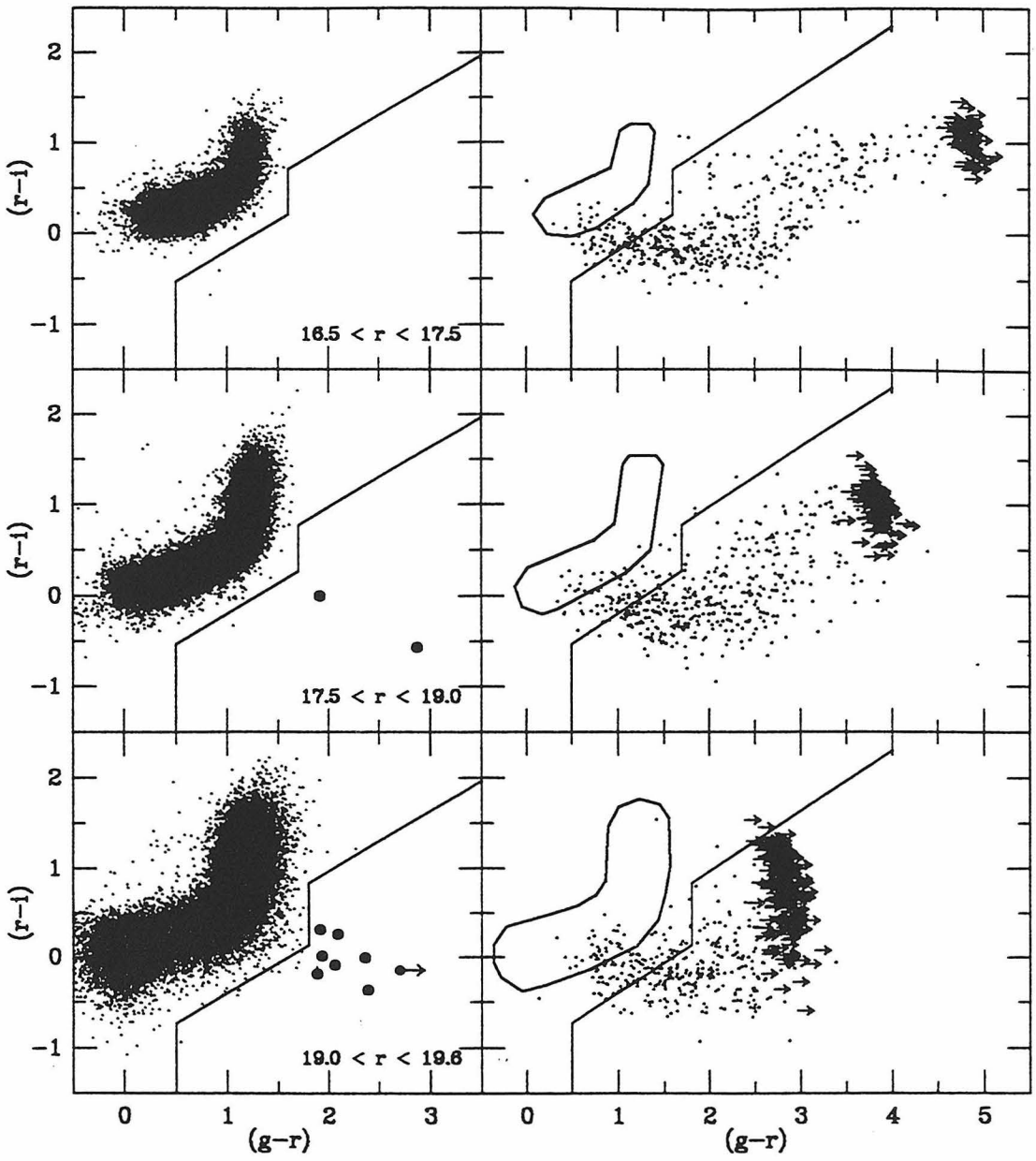

Figure 2.4: Color-Color Diagrams

Left: Color-color diagrams in three magnitude ranges containing stellar objects from four survey areas. The large filled circles are the PSS quasars. The arrow denotes a limiting $(g-r)$ color. The solid lines demark our survey selection area: objects are chosen as candidates if they lie to the right of these lines. Right: The colors computed from case B model quasar spectra over the range $4 < z < 5$ at $r = 17.3^m$ (top), $r = 18.3^m$ (middle), and $r = 19.3^m$ (bottom). The location of the stellar loci and the selection areas are indicated for reference.

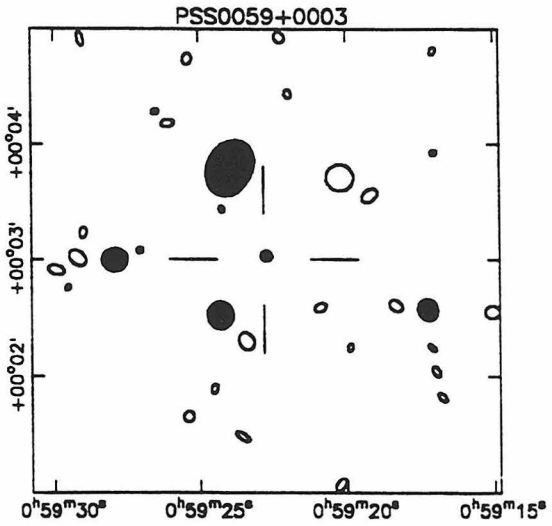
PSS0059+0003
+00°04'
+00°03'
+00°02'
0h59m30s
0h59m25s
0h59m20s
0h59m15s

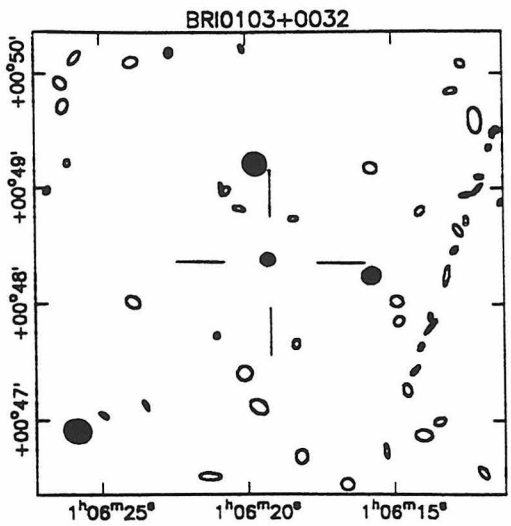
BRI0103+0032
+00°50'
+00°49'
+00°48'
+00°47'
1h06m25s
1h06m20s
1h06m15s

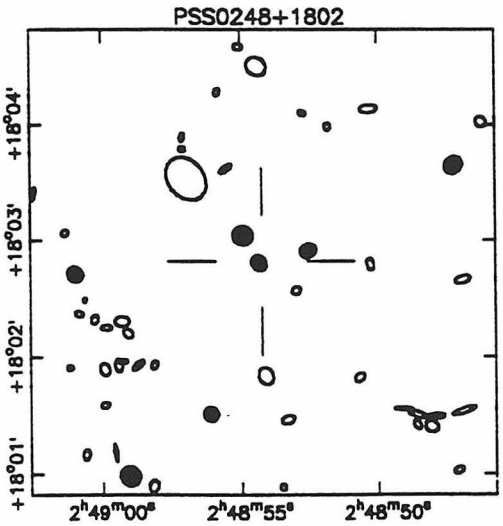
PSS0248+1802
+18°04'
+18°03'
+18°02'
+18°01'
2h49m00s
2h48m55s
2h48m50s

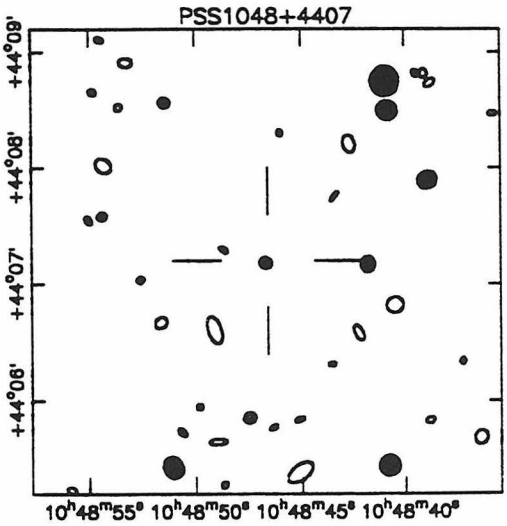
PSS1048+4407
+44°09'
+44°08'
+44°07'
+44°06'
10h48m55s
10h48m50s
10h48m45s
10h48m40s

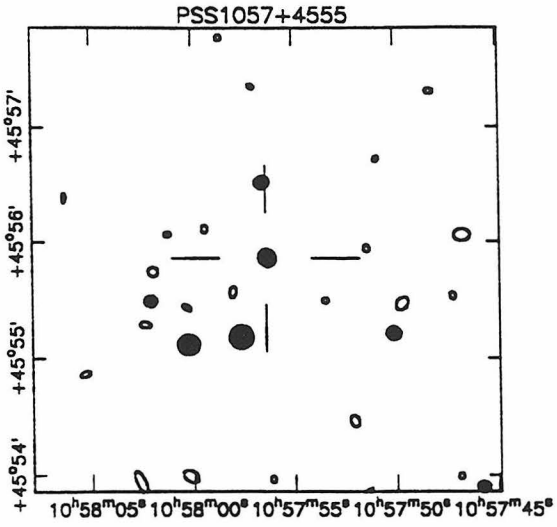
PSS1057+4555
+45°57'
+45°56'
+45°55'
+45°54'
10h58m05s 10h58m00s 10h57m55s 10h57m50s 10h57m45s

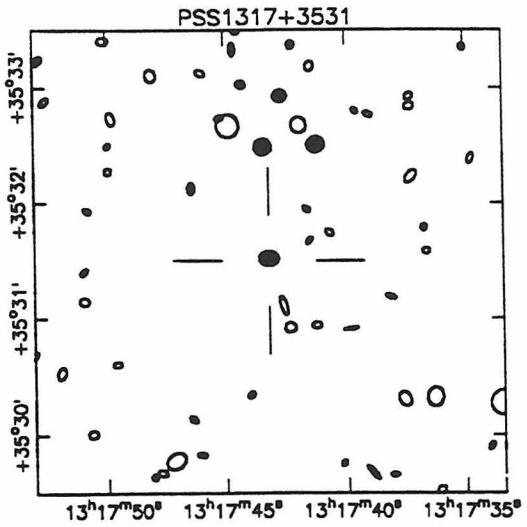
PSS1317+3531
+35°33'
+35°32'
+35°31'
+35°30'
13h17m50s 13h17m45s 13h17m40s 13h17m35s

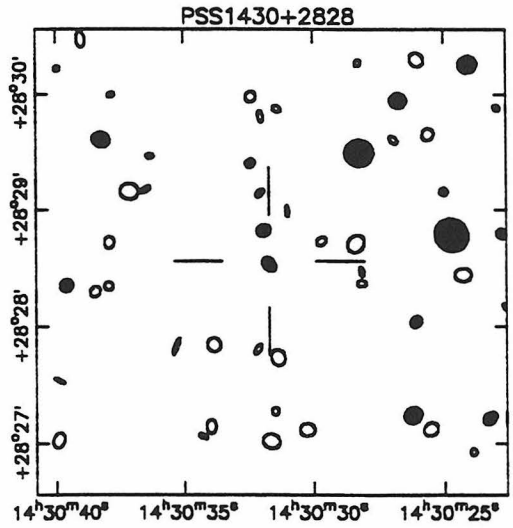
PSS1430+2828
+28°30'
+28°29'
+28°28'
+28°27'
14h30m40s 14h30m35s 14h30m30s 14h30m25s

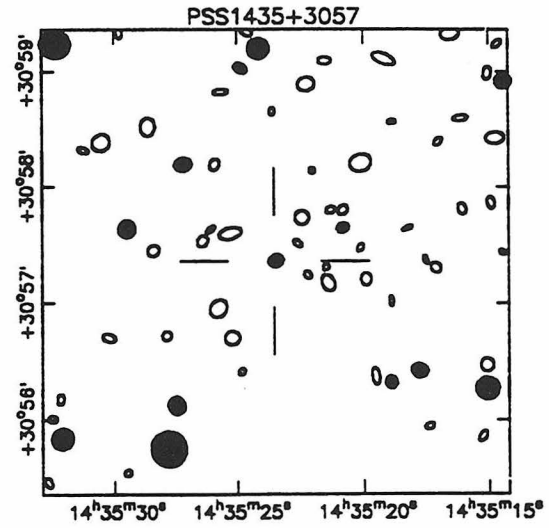
PSS1435+3057
+30°59'
+30°58'
+30°57'
+30°56'
14h35m30s 14h35m25s 14h35m20s 14h35m15s

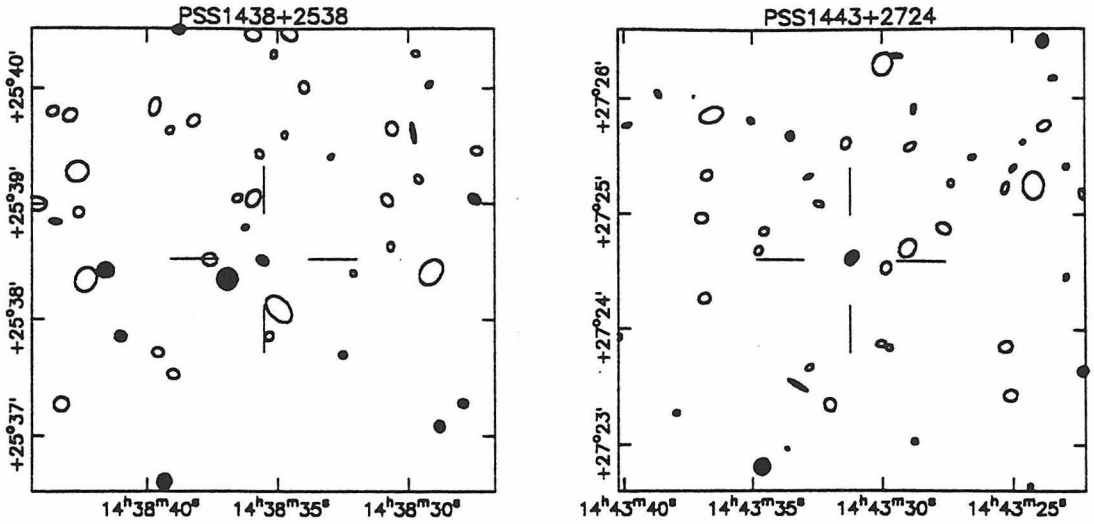

Figure 2.5: Finding Charts

Finding charts for the nine PSS quasars and BRI 0103+0032. The filled symbols represent stellar objects while the open symbols represent galaxies. The coordinate axes are in J2000 equinox. All diagrams are 4 arcmin square with N up and E to the left.

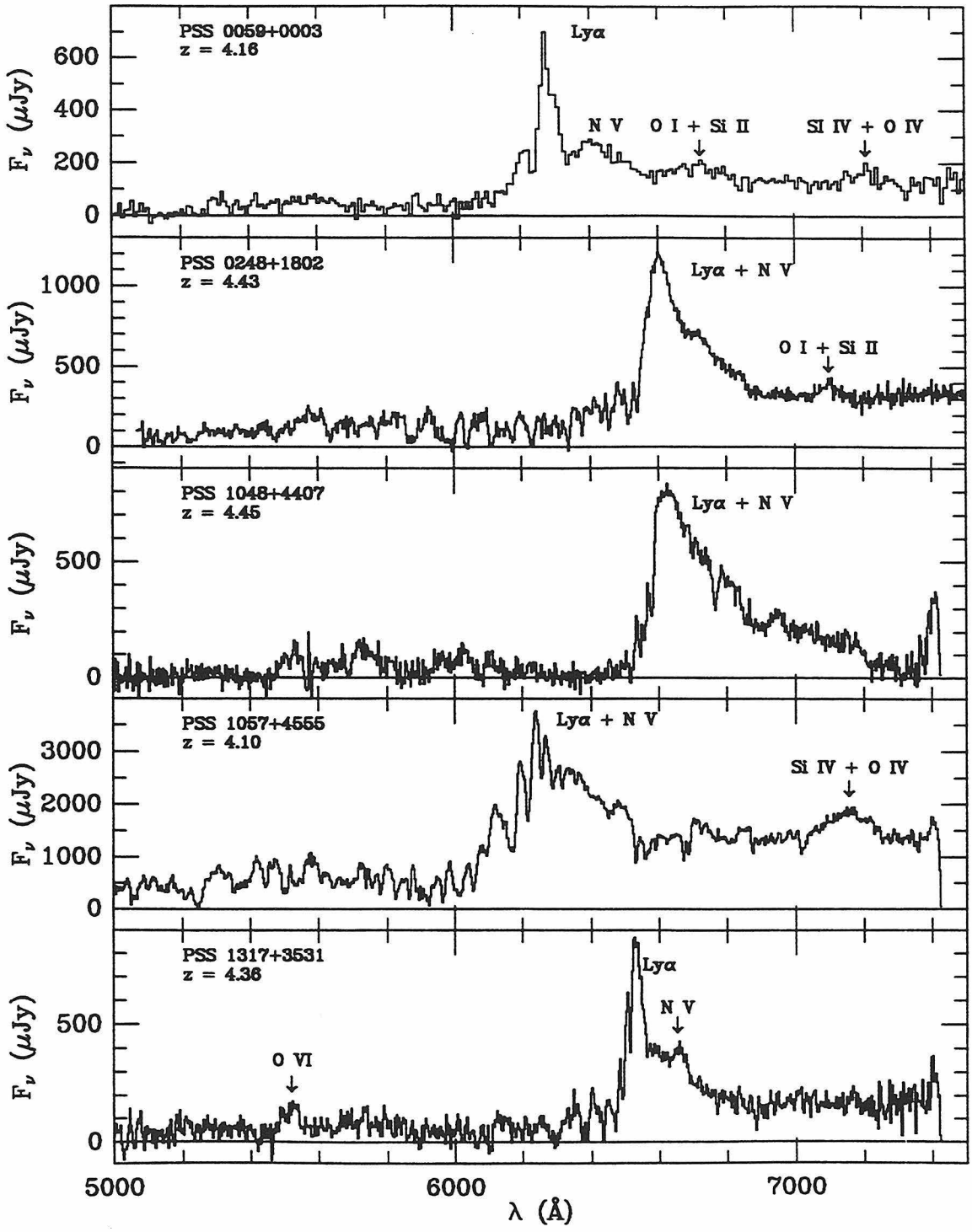
PSS 0059+0003
z = 4.16
Lyα
N V
O I + Si II
Si IV + O IV
PSS 0248+1802
z = 4.43
Lyα + N V
O I + Si II
PSS 1048+4407
z = 4.45
Lyα + N V
PSS 1057+4555
z = 4.10
Lyα + N V
Si IV + O IV
PSS 1317+3531
z = 4.36
Lyα
N V
O VI
F_ν (μJy)
λ (Å)
5000
6000
7000

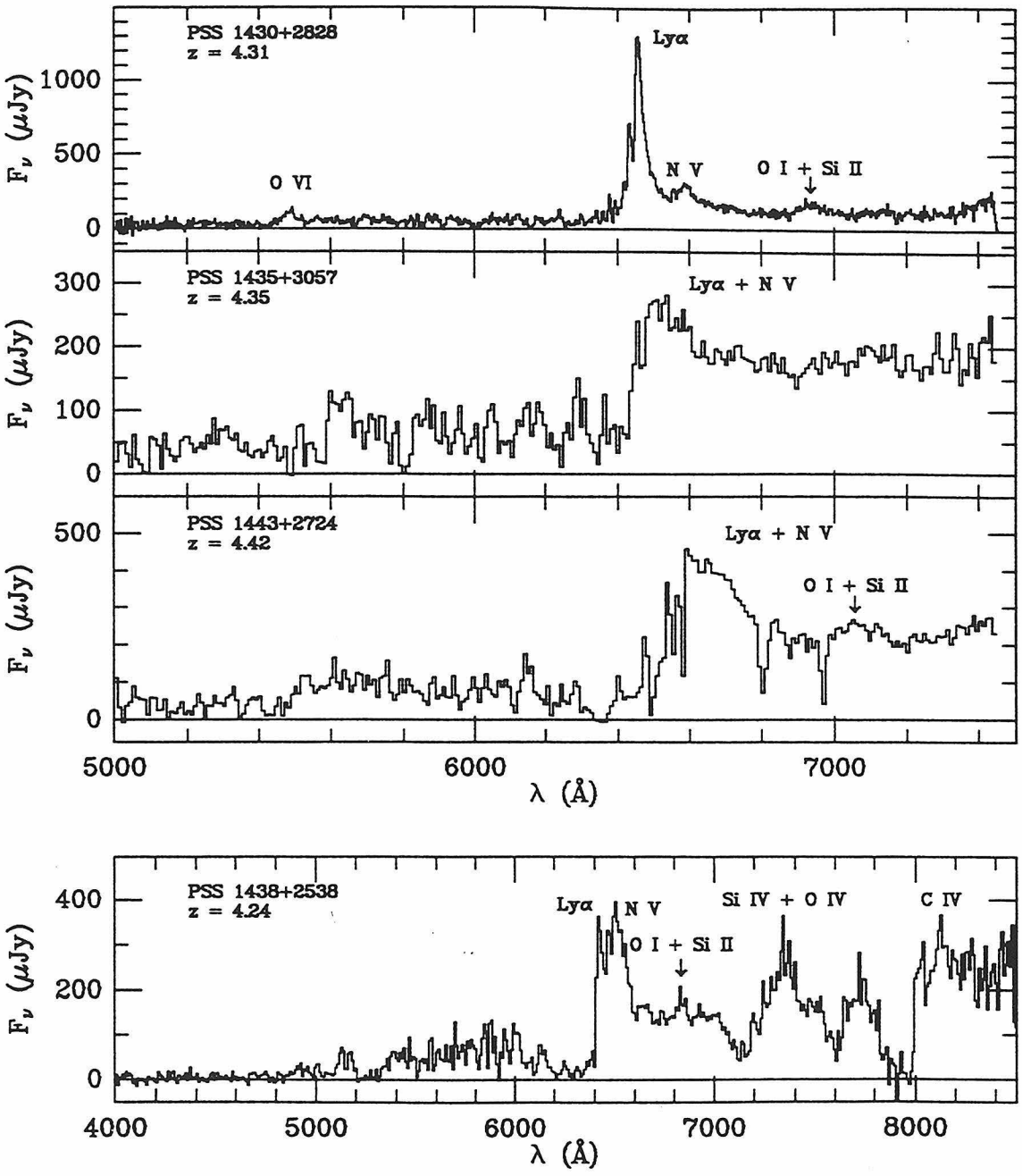

Figure 2.6: PSS Discovery Spectra

Spectra of the nine new PSS quasars discovered so far. Obvious emission lines are labeled. For a spectrum of BRI 0103+0032, see Figure 4.2a.

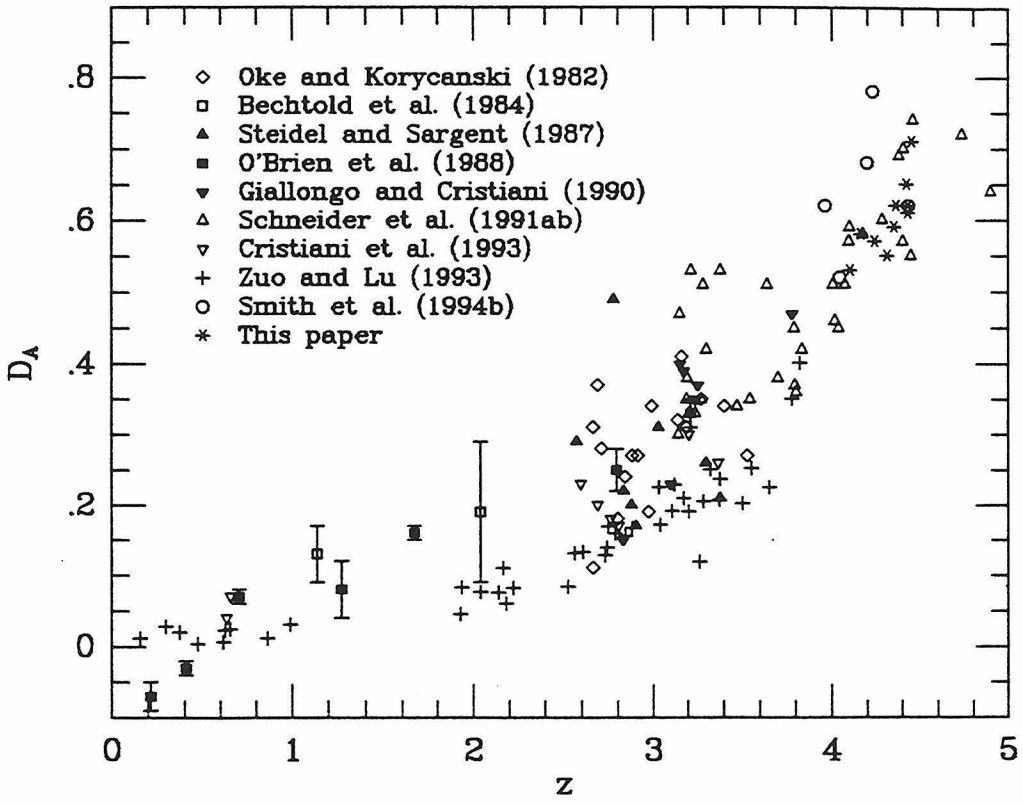

Figure 2.7: Continuum Depression Values

Values of the continuum depression blueward of Lyα (D_A) as a function of redshift as reported in various surveys.

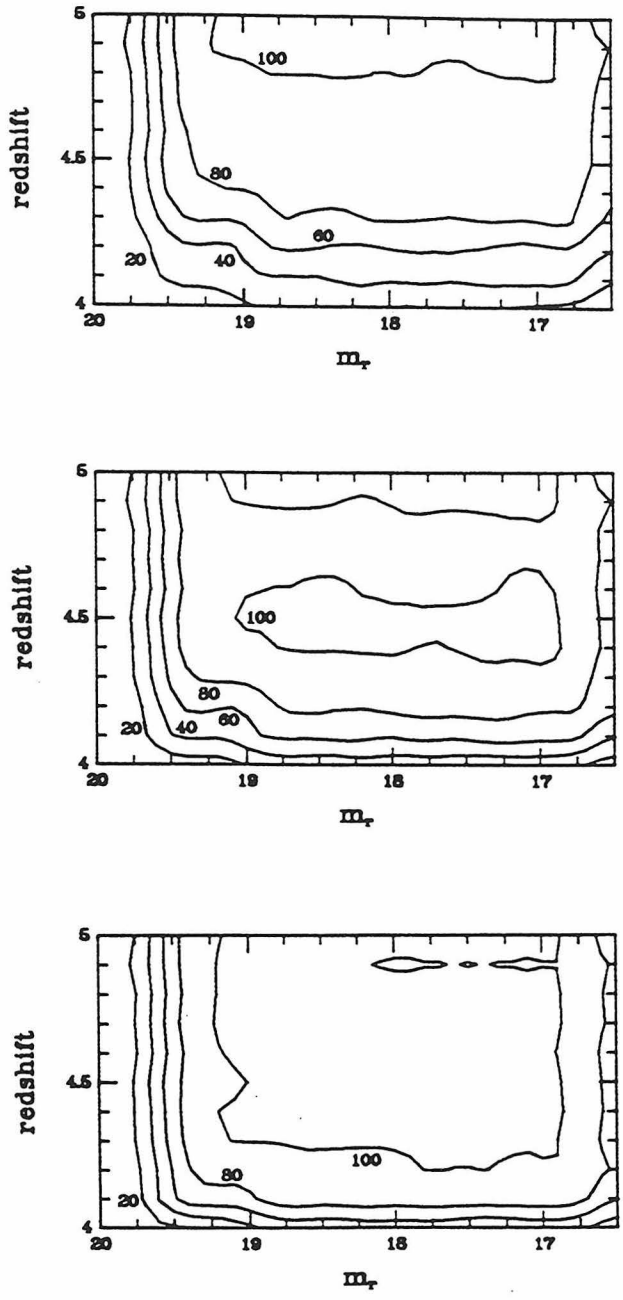

Figure 2.8a: Selection Probabilities

Contour plots showing the selection probabilities for quasars of different line strengths, redshifts, and r magnitudes. Contours are drawn at 20% intervals. Top: Lyα = 32.5Å (case A); Middle: Lyα = 65Å (case B); Bottom: Lyα = 130Å (case C).

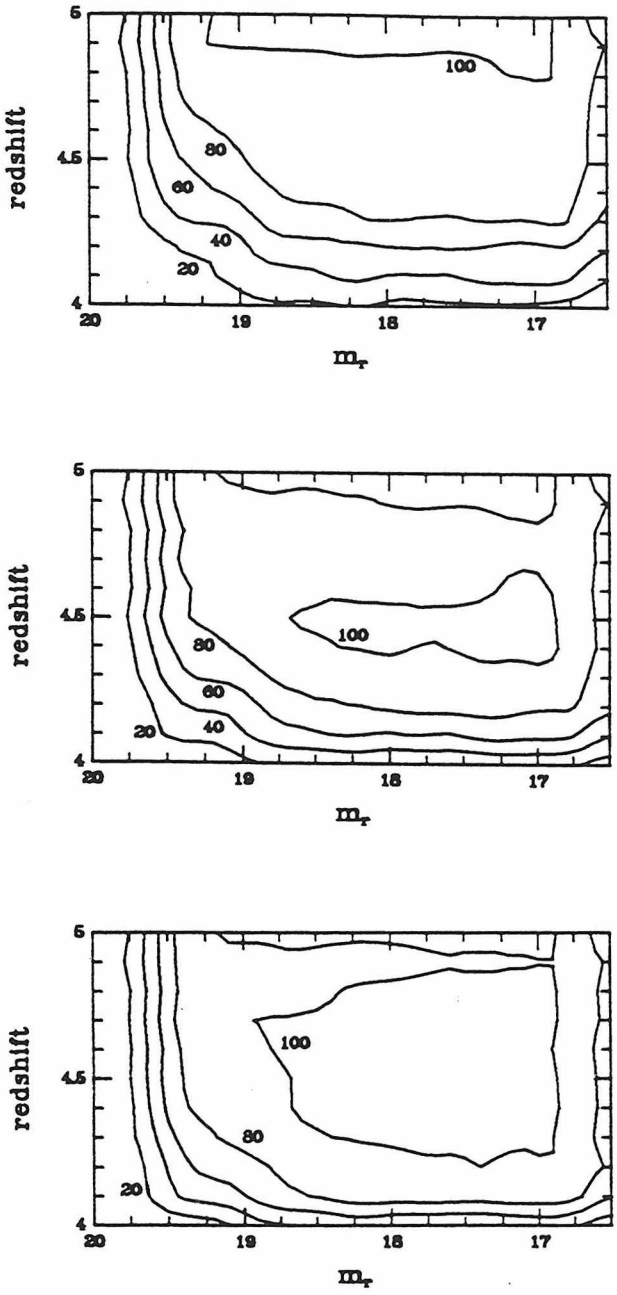

Figure 2.8b: Detection Probabilities

Same as Figure 2.8a, but multiplied by the spectroscopic probability as described in the text, giving the detection probabilities, p, for quasars with different line strengths, redshifts, and r magnitudes.

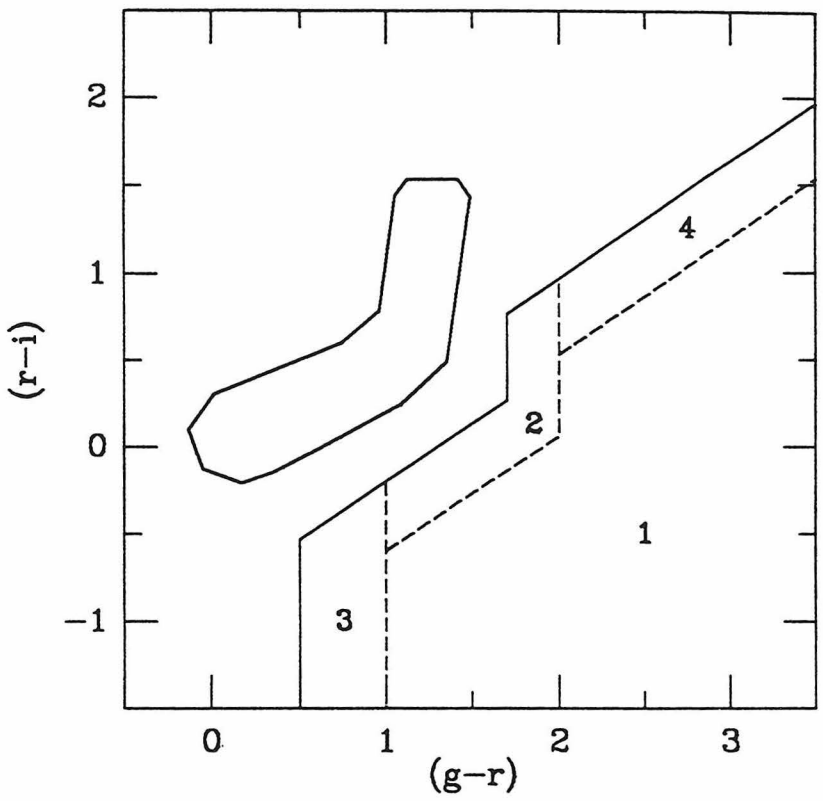

Figure 2.9: Spectroscopic Completeness Areas

Schematic representation of the spectroscopic completeness areas. See text (Section 2.3.3).

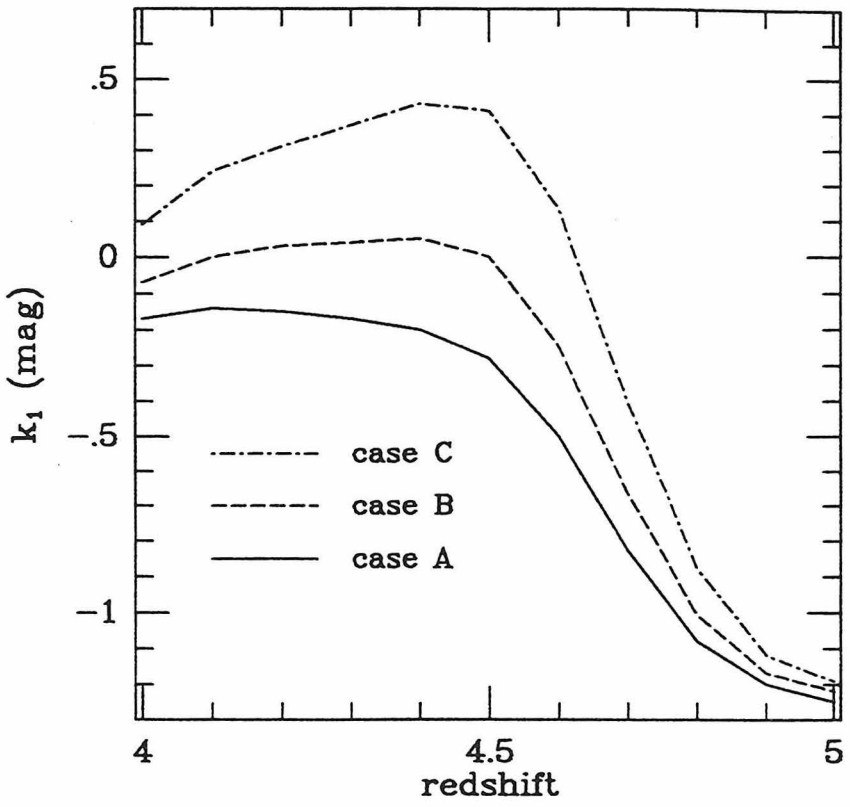

Figure 2.10: The k-Correction

The k-correction from $M_{AB(1450)}$ to r magnitude as a function of redshift for the three line strength cases described in the text.

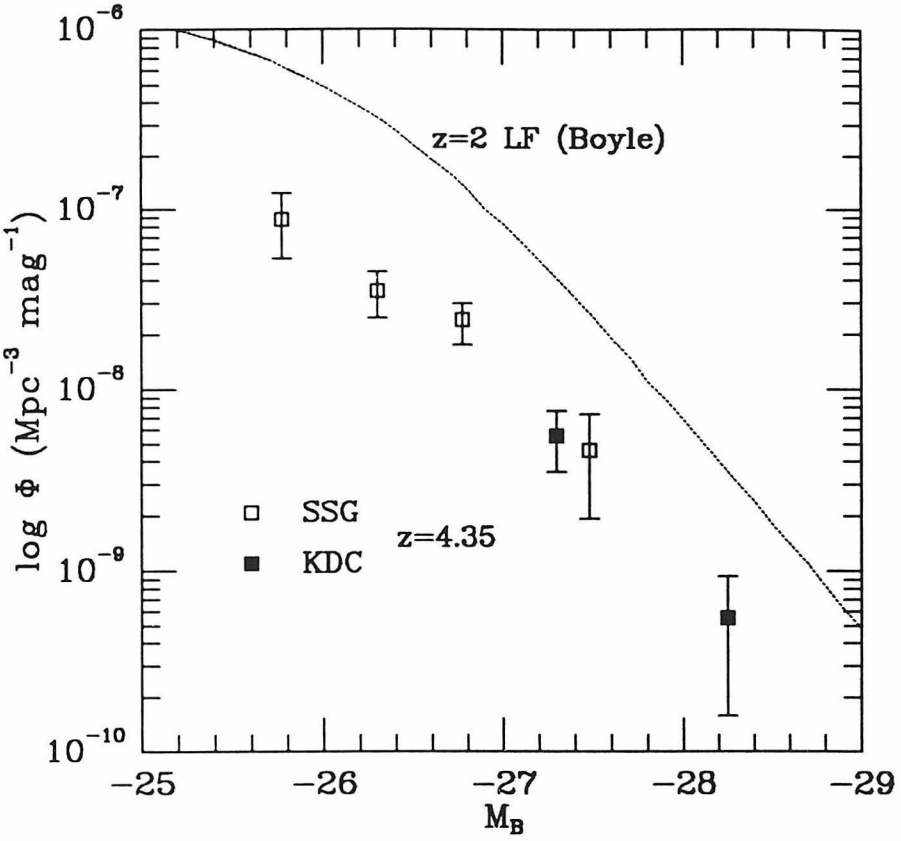

Figure 2.11: Differential Quasar Space Densities

Quasar space densities per magnitude at $4 < z < 4.5$ as a function of M_B from this survey (KDC) as well as SSG. The $z = 2$ QLF from Boyle (1991) is shown for comparison (dotted line).

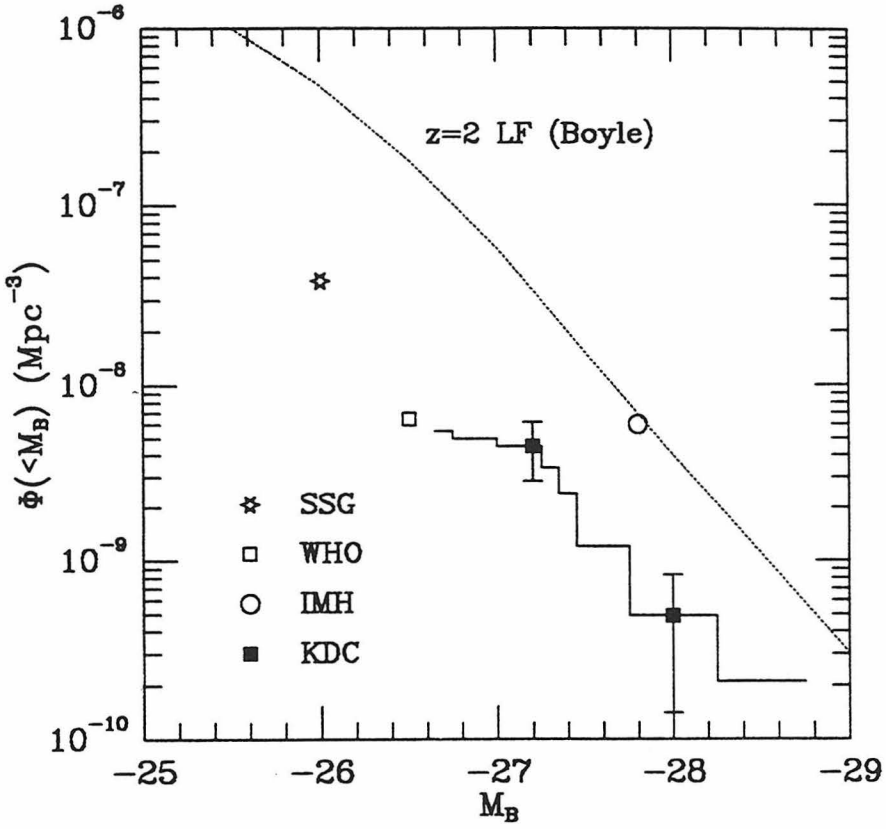

Figure 2.12: Cumulative Quasar Space Densities

Cumulative space densities at $4 < z < 4.5$ from the four surveys for high-redshift quasars described in the text. The $z = 2$ QLF from Boyle (1991) is shown for comparison (dotted line).

Chapter 3

A Multicolor CCD Survey for Faint $z > 4$ Quasars†

ABSTRACT

We describe survey techniques and initial results for a 0.69 deg^2 CCD multicolor survey for quasars at $z > 4$. The original motivation for the survey was to detect quasar clustering at high-redshift in order to constrain theories of structure formation at early stages in the history of the universe. Therefore, the majority of data reported here are centered on fields containing known $z > 4$ quasars and a few are centered on blank control fields. We have selected a complete rigorously defined sample of 39 quasar candidates and have examined seven of these spectroscopically, confirming none as high-redshift quasars. However, we have surveyed enough area to constrain the $z > 4$ quasar luminosity function at $M_B < -24.0^m$ and find limits consistent with the double power law formulation of Boyle (1991) and Hewett et al. (1993) scaled down in density. On an initial examination of the data, we discovered a faint quasar with a peculiar spectrum at $z = 3.60$. We were also able to recover three quasars at $z > 4$ discovered by Irwin, McMahon, & Hazard (1991) but not fully documented in the literature. These objects are reported here as well. Finally, we place weak contraints on quasar clustering for high values of Ω_0 and discuss the future prospects for detecting quasar clustering at high-redshift using these survey techniques.

---

† Adapted from a paper entitled "A Multicolor CCD Survey for Faint $z > 4$ Quasars" by J.D. Kennefick, S.G. Djorgovski, and G. Meylan, submitted to the Astronomical Journal.

3.1 Introduction

The discovery of quasars at $z > 4$ provides an opportunity to investigate the formation of galaxies and large scale structure at very early epochs when the universe was only $\sim 5-10\%$ of its present age (Small & Blandford 1992, Haehnelt & Rees 1993). Given the homogeneity of the universe at $z \sim 1000$, the very existence of quasars at redshifts greater than four presents severe timing problems, as these massive objects ($10^{7-10} M_{\odot}$) would need some time to form and turn on (Turner 1991, but see Katz et al. 1994). This suggests that $z > 4$ quasars reside in the most massive objects which have collapsed by that epoch and are associated with rare high peaks in the primordial density field. Such high peaks should be strongly clustered (Kaiser 1984).

A generic prediction for any reasonable primordial density fluctuation spectrum is a strong *ab initio* clustering of quasars at large redshifts. In particular, Efstathiou & Rees (1988) predict that, for the CDM model, quasars at high redshift should be clustered with an amplitude comparable to that of bright galaxies today. Cole & Kaiser (1989) find that for CDM the clustering strength would be intermediate between bright galaxies and rich clusters. It therefore makes sense to look for high redshift quasars near other high redshift quasars. Schneider et al. (1994) found three cases of probable physical pairs of quasars in their sample of 90 quasars from the Palomar Transit Grism Survey, all with $z > 3$. These could be just the kind of structures we are looking for.

We have conducted such a survey for quasar-marked protoclusters at $z > 4$ (Djorgovski et al. 1991, Djorgovski et al. 1992b, Smith et al. 1993). An effective way to search for quasars at $4 < z < 5$ is through multicolor imaging in the Gunn-Thuan *gri* or similar passbands. This technique exploits the fact that at these redshifts, the Lyα line is emitted in the r passband, and the continuum drop due to the Lyα forest blueward of the line (which is $\sim$60% at these redshifts) results in a strong color-color signature (see Figure 1.1). The majority of currently known

$z > 4$ quasars were discovered employing such techniques (Warren et al. 1991b, Irwin et al. 1991, Smith et al. 1994ab, Kennefick et al. 1995ab, Darling et al. 1996).

We have covered enough area to provide intial constraints on quasar clustering and set some new limits on quasar space densities at faint magnitudes ($-26^m < M_B < -24^m$). The $z < 2.2$ quasar luminosity function (QLF) has been well established (Boyle 1991, Hewett et al. 1993), but the evolution of the QLF at high redshift has for many years been the subject of much debate, with some groups seeing evidence for a decline in the number of quasars from $z = 2$ to $z = 4$ (Schmidt et al. 1995, Warren et al. 1994, Kennefick et al. 1995b), while others have claimed that the density of objects remains constant (Irwin et al. 1991). Here we present evidence that space densities decrease from $z = 2$ to $z = 4$ at faint magnitudes. When combined with the results from Schmidt et al. (1995, SSG) and Kennefick et al. (1995b, KDC), our results are consistent with pure density evolution from $z = 2$ to $z = 4$.

At the time we began this survey (~1990), ~40 $z > 4$ quasars were known, but only 17 had published coordinates. As we desired a larger sample, we conducted a survey to "rediscover" the BRI quasars of Irwin et al. (1991) (Smith et al. 1994ab). We recovered seven of them, five of which we have obtained deep imaging around for use in this survey. We have subsequently recovered three more BRI quasars, around which deep imaging was obtained, and information for these objects is presented here.

We have obtained deep CCD images of 39 fields (0.69 square degrees) in the *gri* or *BRI* bands, 33 of which contain or are near $z \gtrsim 4$ quasars. Spectroscopy for several candidates chosen from initial reductions were obtained, most of them identified as galaxies at $z < 1$. However, we discovered one faint quasar with a peculiar spectrum at $z = 3.60$. The data were subsequently re-reduced and rigid candidate selection procedures adopted. A total of 39 final candidates have

been selected and follow-up spectroscopy has been obtained for seven of them, confirming none of them as $z > 4$ quasars. Data reduction and candidate selection procedures are described, and selection functions presented. Finally, we discuss the future prospects for detecting quasar clustering at high redshift. We assume an $H_0 = 50$ km s^{-1} Mpc^{-1}, $q_0 = 0.5$ cosmology throughout.

3.2 Observations and Data Reduction

3.2.1 CCD Imaging

A total of 39 fields were imaged in the *gri* or *BRI* bands between September, 1988 and August, 1994, primarily under slightly variable conditions. Of these, 33 were fields containing or near a $z \gtrsim 4$ quasar and six were centered on blank fields. The *gri* data sets are listed in Table 3.1. Targeted fields are listed first, with the field name indicating the quasar around which the data was taken. The blank fields are listed last. They were obtained in conjunction with a Fabry-Perot search for primeval galaxies (Thompson 1995, Thompson et al. 1995) and are denoted "FP." The *BRI* data sets are listed in Table 3.2. All of the *BRI* data sets were targeted around known $z \gtrsim 4$ quasars.

The majority of the *gri* data were taken at the Palomar 200 inch telescope with both the 4Shooter and COSMIC instruments. The 4Shooter employs a mosaic of four 800×800 Texas Instruments CCDs with a scale of 0.334″/pixel. COSMIC uses a 2048 × 2048 Tektronix CCD with 0.284″/pixel. Additional *gri* data were obtained at the CTIO 4-meter telescope using a Tektronix 1024 × 1024 CCD with 0.473″/pixel. Most of the *BRI* data were obtained at the ESO NTT using the EMMI instrument on UT 1994 April 12 - 14. EMMI employs a 2048 × 2048 Tektronix CCD with 0.268″/pixel. One set of *BRI* data was obtained at the CTIO 4-meter telescope with the CCD described above.

The nightly observations consisted of several bias frames and dome flatfield frames in each band. Twilight and dawn sky flatfield frames were taken as time allowed, especially in the g and B bands. For a given field, at least two exposures were typically taken in each band offset by several arcseconds to aid in flatfielding and cosmic ray and chip defect removal as well as to increase the total exposure

time. If the night was deemed photometric, at least one standard star was observed in each band (Thuan & Gunn 1976, Kent 1985, Landolt 1992).

3.2.2 CCD Processing

The CCD images were bias corrected, overscan subtracted, flatfielded, and trimmed using the CCDRED facility in IRAF. When twilight and/or dawn sky flats were available, they were combined with the dome flats in the initial flatfielding. There usually remained a significant gradient across the frames after initial flatfielding, probably due to differences in the sensitivity of the chips between the dome flats and the night sky. When sufficient object frames were available from a given night or observing run, the object frames were combined to make an illumination flat using the COMBINE and MKSKYCOR tasks in IRAF. Once this correction was applied, the variations in the sky level were less than 2% and for most frames was on the order of 1%. For data sets where there were not enough object frames to create an illumination flat, and where the gradient across the frames was significant, the frames were corrected individually. This was done by binning the images, interpolating over objects visible in the frames, smoothing the frames heavily, and fitting a high order (typically six) 2-dimensional polynomial surface to the frame. The resulting gradient images were magnified back to the original image size and used to correct the original frames. Frames corrected in this way also had resulting sky variations on the order of 1%.

Once the frames were flatfielded, images from the three bands in a given field were shifted into coincidence at the pixel level and trimmed to include only the overlap region of all the images in the data set using the IMALIGN task in IRAF. Frames from each band were then coadded, weighted by their exposure times. No effort was made to remove cosmic rays or chip defects at this point.

3.2.3 CCD Photometric Calibration

Only eight of the 30 *gri* data sets were obtained under fully photometric conditions. These sets were calibrated with *gri* exposures of 1-3 Gunn-Thuan (Thuan & Gunn 1976, Kent 1985) standard stars. Photometric zero point errors range from 0.02^m to 0.05^m in each band. Six fields were calibrated using regions that overlapped with photometric data. Because only a small area of the fields overlapped, the photometric zero point errors are on the order of 0.1^m. Ten fields were calibrated using images obtained at the Palomar 60 inch telescope under photometric conditions. Photometric zero point errors for these fields are on the order of 0.1^m. Three targeted fields had no calibrating data available, so reported magnitudes of the quasar in the field were used to roughly calibrate the data. Since quasars are known to vary on the scale of years (Hook et al. 1994), these zero points are very uncertain ($\sim 0.2^m$ errors). Three of the FP fields had no calibrating data available. They were roughly calibrated by using an average zero point for the 4Shooter data, with errors estimated to be on the order of 0.3^m.

Five of the eight *BRI* data sets taken with EMMI at the ESO NTT were obtained under photometric conditions. They were calibrated with *BRI* exposures of two standard stars from Landolt (1992) and have zero point errors of 0.05^m. The R band images of the remaining three EMMI fields were calibrated with R band images taken under slightly variable conditions on a subsequent date, and have zero point errors estimated at 0.2^m. The *BRI* set from the CTIO 4m had no calibrating data. A zero point for the R image was estimated using the reported R band magnitude of the target quasar and therefore is quite uncertain.

For data sets taken on non-photometric nights, only r or R band zero points were estimated from overlapping data or QSO magnitudes. g or B and i or I band zero points were found by visually shifting the stellar locus of the data in their color-color diagrams into coincidence with the stellar loci of the well calibrated data. This procedure can be repeated consistently to within 0.1^m.

3.3 Data Analysis

The data were initially reduced using DAOPHOT (Stetson 1987). Frames were shifted into coincidence and object detection and measurement performed on the r or R band frames. Object measurement was then performed on the g or B and i or I band frames at the r band positions of the detected objects. No initial attempt was made to separate stars from galaxies. Candidates were selected from appropriate areas of the color-color space, and object morphology judged by eye. Follow-up spectroscopy was performed on several of these objects. Most were identified as galaxies at $z < 1$ or were too faint to make firm identifications. One of these candidates was confirmed as a quasar at $z = 3.60$ (Section 3.3.4.3).

In order to estimate quasar space densities, the survey completeness had to be estimated. This required a more stringent application of object classification and candidate selection procedures. Subsequent data reduction was performed and objects classified using FOCAS (Jarvis & Tyson 1979; Valdes 1982). These reductions are described in detail below.

3.3.1 Object Detection

Object detection and measurement was performed using FOCAS within the SKICAT environment (Weir 1994, Weir et al. 1995c). The FOCAS detection algorithm works by smoothing the data (we used the built-in FOCAS filter) and searching for contiguous pixels with values greater than the locally estimated sky by the specified detection threshold. The minimum detection area was set to three times a seeing disk (where seeing is defined as the FWHM of an unresolved object). The detection thresholds were set to 2.5σ in r, R, i, and I and 2.0σ in g and B. Objects near bright saturated stars often went undetected, so these areas were ignored and are not included in our area estimations given in Tables 3.1 and 3.2.

One of the CCDs in the 4Shooter mosaic is partly covered by the spectrographic slit. The affected area is trivial, but was also excluded from the estimated area.

Once objects are detected, their attributes are measured and a classification is assigned. The FOCAS classification of an object is based on its similarity to a set of classification templates generated from a stellar point spread function (PSF) formed from stellar objects in the frame. Typically 3-20 stars were used in constructing the empirical PSF, the number depending mainly on the field size. A PSF was formed for each coadded image individually including a different PSF for each of the four images that comprise a 4Shooter mosaic.

Aperture magnitudes were measured at a radius of two times the HWHM in order to optimize the signal to noise (Thompson 1995). FOCAS also measures a total magnitude by "growing" the detection isophote out until the total area is twice the detection area for that object. Magnitudes quoted below are total magnitudes unless stated otherwise whereas colors are computed from aperture magnitudes. However, median corrections from aperture to total magnitudes are small ($< 0.05^m$).

3.3.2 Completeness Estimates

In order to establish detection limits of stellar objects in the data sets, Monte Carlo simulations were performed. An image of a stellar object was formed from the constructed PSF. This image was then scaled to random magnitudes (within a certain range) and added to a random position in the frame that was known to be free of other objects. Typically ten objects were added to a frame at one time to avoid overcrowding. A total of 100 simulated frames were made resulting in 1000 simulated objects. FOCAS object detection and measurement was performed on these frames and the object catalogs examined to see what percentage of simulated objects were sucessfully detected. Figure 3.1 shows the results of these simulations

for one of the fields. The detection limit is taken as that magnitude where the detection probability falls below 90% (dotted line). The detection limits for each field are listed in Tables 3.1 and 3.2.

A critical element in eliminating contaminating galaxies from the candidate lists is star/galaxy classification. Because quasars at $z > 4$ have large $(g-r)$ colors, and our data go deeper in r than in i, we rely on r band classifications. In order to assess the classification accuracy of FOCAS, the same Monte Carlo simulations were performed, counting the percentage of objects detected and classified as stellar (FOCAS "star" or "fuzzy star" classifications, see Valdes 1982 for a description). The classification limit was taken to be the magnitude where the percentage of simulated objects detected as stellar dropped below 90%. This was typically one magnitude above the detection limit (Figure 3.1).

Random aperture magnitude errors in each band were established from these simulations as well. The difference between the target magnitude and the recovered aperture magnitude was computed for each detected simulated object. These magnitude differences were plotted *vs.* the target magnitude, aperture corrected, and normalized to the field's limiting detection magnitude. A Gaussian profile was then fit to the errors in half magnitude bins for each field. The median σ of the errors from all the fields in each half magnitude bin was then computed. These errors are shown in Figure 3.2 plotted *vs.* magnitude above the detection limit.

3.3.3 Candidate Selection

Once catalogs of the images in the three bands where formed and detection limits established, the catalogs were matched together using SKICAT matching algorithms (Weir 1994). The catalogs were filtered for those objects with a detection in both the r and i bands and classified as stellar ("star" or "fuzzy star") in the r band. No g band detection was required. Aperture colors for all the stellar

objects were then computed and plotted in $(g-r)$ *vs.* $(r-i)$ color-color diagrams (Figures 3.3 and 3.4). For objects with no g detection, the limiting g magnitude was adopted. A magnitude equal to the g band limit was also assigned to those objects detected in g but whose magnitudes were found to be below the g detection limit. Limiting $(g-r)$ colors were computed for these objects.

The candidate selection was also limited in r magnitude. Because classification limits were on average one magnitude above the r band detection limits, we adopted $r = (r_{lim} - 1^m)$ as the r band selection limit of a data set. Therefore, from each field, candidates were limited to those objects brighter by at least one magnitude in r than the r band detection limits given in Tables 3.1 and 3.2.

Objects were selected as candidates if they populate specific areas of the color-color space. This area was chosen on the basis of model quasar colors (discussed below), the colors of the known quasars in the fields, and the location of the locus of stars. These selection lines are shown in Figures 3.3 and 3.4. Objects lying to the right of these lines were chosen as candidates and are shown as squares. Filled squares indicate that a spectrum of that object has been obtained. Candidates with limiting $(g-r)$ colors have arrows pointing to the right. Known quasars are shown as open stars. Notice that all of the known quasars in the BRI diagrams of Figure 3.4 lay within the selection area, even those at $z \sim 4$ such as BRI 1500+08. Two known quasars, Q 0000−26 and PC 2331+0216, both at $z = 4.10$, do not lie within the gri selection areas. The B band is in general a better descriminant than the g band because the B band samples that part of $z \gtrsim 4$ quasar spectra where Lyman continuum absorption is stronger (Figure 1.1).

An image of each candidate was examined in each band to make sure their extreme colors were real. If a cosmic ray was found near a candidate object in one of the frames, it was removed by hand (replacing it with the local median) and object detection and measurement reperformed on the frame. If a candidate had a better detection in i than in r, was classified as a galaxy in i, and appeared

extended, it was discarded as a candidate. Candidates were also discarded if they were affected by chip defects, although this was rare.

A total of 39 candidates satisfying all of these criteria have been selected ranging in magnitude from $r = 21.0^m$ to $r = 23.5^m$. It should be noted that the detection and classification limits are independent of the adopted zero points and so are not affected by the lack of calibration. If new zero points are adopted in the future as we acquire further calibration, the detection limits will move along with the magnitudes of the objects and the candidate list will not change.

3.3.4 Some Initial Results

3.3.4.1 The Recovery of Three z > 4 Quasars

Irwin, McMahon, & Hazard (1991, IMH) have conducted a ~2500 deg^2 multicolor photographic survey for $z > 4$ quasars using APM scans of UK Schmidt plates. They have been very successful at recovering $z > 4$ quasars, but have yet to make details of the survey available to the general community, including coordinates for their objects. They have released names for many of the quasars in the form BRI hhmm+dd (Irwin & McMahon 1990). With the hope of using these quasars in our protocluster search, we designed a CCD survey aimed at recovering several of these BRI quasars and have published coordinates, finding charts, and spectra for seven of them (Smith et al. 1994ab, Chapter 4). The CCD data acquired in this survey did not go much deeper than the expected magnitudes of the target quasars, but several of them were later observed to a deeper level and are included in the protocluster survey.

By April, 1994, we had acquired the names of three more BRI quasars in the form BR(I) hhmm+ddmm (Storrie-Lombardi et al. 1994, Storrie-Lombardi 1994). This allowed all possible coordinates to be covered in two pointings with the EMMI on the ESO NTT (field size $\sim 9' \times 9'$). Deep imaging was obtained on the two

pointings around BRI 1328−0433 and one pointing each around BR 0951−0450 and BR 0945-0411 at the ESO NTT on UT 1994 April 12-14. Exposure times were 1200 seconds in B and 840 seconds in R and I. These data are included in our multicolor protocluster search (Table 3.2). The data were reduced as described in section 3.2.2 and color-color diagrams produced. The quasars were immediately obvious (Figure 3.4, open stars) due to their separation from the stellar locus and their bright magnitudes. We were very fortunate in that both BR 0951−0450 and BR 0945-0411 were recovered even though only one of the necessary pointings had been obtained.

Confirming spectra were taken on UT 1995 March 29-30 at the ESO NTT using EMMI. Two 1800 second exposures were obtained for the three quasars in each of two moderate resolution gratings over the wavelength ranges 4000Å to 6600Å (G5) and 6000Å to 8350Å (G6). The spectra were flux calibrated using three standard stars from Baldwin & Stone (1984). Wavelength calibration, using a polynomial fit to helium and argon arcs, has residuals of ∼0.2Å (G5) and ∼0.7Å (G6). The spectra from the two gratings were scaled to a common flux and coadded, and have been binned to increase the signal to noise (Figure 3.5). Adopted redshifts for the objects are listed in Table 3.3. BR 0945−0411 shows characteristics of a BAL quasar with broad absorption at $\sim$ 7000Å and $\sim$ 7800Å, and the Lyα line seems to have been almost completely absorbed.

Coordinates and R magnitudes are listed in Table 3.3. Finding charts are given in Figure 3.6.

3.3.4.2 Galaxies at z < 1

In the initial stages of the survey, our candidate selection procedures were not applied consistently, and classification limits were not established. Objects were initially chosen for spectroscopy that did not make our current final candidate list. Most of these objects were identified as galaxies at $z < 1$. Figure 3.7 shows

two such objects selected from the Q2203+29 field. Object 403 has a redshift of $z = 0.810$. The [O II] line and the 4000Å continuum break give it a red color similar to quasars at $z \sim 4$. Object 92, with a redshift of $z = 0.258$, has three emission lines in the r band, also giving it a red color. These two objects are too faint ($r \sim 23.5^m$) to be included in the final candidate list, but demonstrate how galaxies at moderate redshifts can mimic the colors of high redshift quasars.

3.3.4.3 A Quasar with a Peculiar Spectrum at z=3.60

4Shooter images in *gri* of the field around known quasar PC 1247+3406 at $z = 4.897$ (Schneider et al. 1991b) were obtained on UT 1992 March 30 at the Palomar 200 inch telescope (Table 3.1, Set A) under hazy conditions. These frames were initially reduced using DAOPHOT (Stetson 1987) and candidates chosen based on their colors and image morphology. One of these candidates, with $m_r = 23.3$, was designated high priority. A 3600 spectrum for this candidate was obtained on UT 1993 March 19 using the Double Spectrograph on the Palomar 200 inch telescope. Conditions were variable, with 1 to 2 magnitudes of extinction and $2''$ seeing. This spectrum showed the presence of broad emission lines, although their nature could not be established. Further spectra totalling 18,000 seconds were obtained over the next two nights under similar conditions and using the same instrument. These spectra were coadded, confirming the presence of broad lines. Still, the signal to noise and the wavelength range covered did not allow a redshift to be established unambiguously.

In order to determine the nature of this object, LRIS spectra totalling 5400 seconds were obtained at the Keck 10 meter telescope on UT 1994 April 09 under good conditions. The coadded spectrum is shown in Figure 3.8. A very weak Lyα line is seen along with C IV and C III, confirming the object as a high redshift quasar. The redshift of this object, denoted QSO 1247+3407, is $z = 3.60$ based on the C IV line. Our survey is not in principle sensitive to objects at this redshift.

However, the weakness of the Lyα line combined with the presence of C IV emission in the r band pushed this object into the selection area of the color-color space. It is near the r band detection limit of our data and is therefore not included in our final candidate list. Subsequent LRIS R band imaging at the Keck 10-meter telescope on UT 1994 April 10 shows the object to have a stellar morphology (Figure 3.9). Coordinates of this quasar are $\alpha = 12^h47^m48.3^s$, $\delta = +34°07'41''$ (B1950).

Infrared imaging was obtained on UT 1994 April 5 and 6 at the Keck 10 meter telescope using NIRC, again showing the object to be stellar in appearance. Infrared magnitudes of the quasar were found to be $K = 19.7 \pm 0.1$ and $J = 21.2 \pm 0.1$. This gives the quasar an $(r - K)$ color of ~ 3.6, which is fairly typical of quasars at these redshifts (e.g., Smith et al. 1994b). Therefore, its peculiar colors are probably not due to reddening by dust.

3.3.4.4 Final Candidates

Follow-up spectroscopy has been performed on seven of the 39 candidates. The candidates examined so far have been difficult to identify spectroscopically. For all objects, a continuum was detected, but no obvious emission was seen, allowing us to conclude that they are not quasars at $z > 4$. The candidates chosen for spectroscopy in our initial pass through the data were mainly identified as galaxies at $z < 1$. This would lead one to believe that the final candidates examined so far but not identified are also early type galaxies at moderate redshifts.

The candidate in the PC 0307+0222 Set A field is the same object as the candidate in the PC 0307+0222 Set C field at $(g - r) = 0.8$ and $(r - i) = -0.1$. That is was chosen as a candidate in both sets is reassuring, but its very different positions in color-color space demonstrates the possible loss of candidates due to photometric scatter. It also demonstrates the ease with which contaminant objects can be scattered into the selection area.

3.4 The Luminosity Function

3.4.1 Survey Selection Probabilities

In a multicolor survey of this type, the selection probabilities play an important role in determining the completeness of the survey and hence the quasar space densities, as these probabilities can vary largely with redshift, magnitude, line strength, etc. In order to assess our survey completeness, we follow the basic Monte Carlo methodology of Warren et al. (1994, WHO) by testing if quasars with different spectral properties in the form of constructed model quasar spectra meet our selection criteria. For this purpose, we use some of the same spectra that we used in assessing the DPOSS survey (Section 2.3.1). These spectra were generated assuming a power law continuum of the form $f_\nu \propto \nu^\alpha$, with $\alpha = -0.5$, and Gaussian profile emission lines of FWHM=5000 km s^{-1}. In Chapter 2, we considered three line strength cases. For simplicity, here we will only consider the case of a typical quasar as described by Wilkes (1986) (Chapter 2, case B). Lyα forest and Lyman-limit system absorption has also been included (see Section 2.3.1 for details). Because the frames of our CCD data sets were usually obtained on the same night, we have not included the effects of quasar variability.

We have generated 50 quasar spectra, each with a different realization of the Lyα forest and Lyman limit system absorption, for each redshift $4 < z < 5$ ($\Delta z = 0.1$), for a total of 550 model quasar spectra. One such spectrum at $z = 4.3$ is shown along with the BRI filter curves in Figure 1.1. Broadband colors were computed for each spectrum by convolving it with the gri and BRI filter curves and calibrating with an appropriate standard. Because each of our data sets reach to different limiting magnitudes, the selection probabilities had to be assessed separately for each set. For each model spectrum and at each magnitude $(r_{lim} - 4) < r < (r_{lim})$, $\Delta r = 0.1^m$, g or B and i or I band magnitudes were

computed in accordance with the colors of that spectrum. Random photometric errors were then added based on the error distributions of Figure 2.2. Model colors for a typical *gri* data set are shown in Figure 3.10 and for a *BRI* set in Figure 3.11 for three different r or R magnitudes. Objects that would have gone undetected in g or B are shown as arrows, denoting a limiting color. All model quasars have colors that put them above the detection limit in i or I.

The selection criteria described in Section 3.3.3 were applied to the final colors. Selection probabilities for typical *gri* and *BRI* data sets are shown in Figure 3.12 as a function of magnitude and redshift. The *gri* selection probabilities rise rapidly from $z = 4.0$ to $z = 4.1$, decline sharply at $z = 4.4$, and then rise again until a decline at faint levels and high redshifts. The decline at $z \sim 4.4$ is due to the dip in the r filter at ~ 6600Å (Figure 2.1). The *BRI* selection probabilities start high at $z = 4.0$ and decline towards higher redshifts as the limiting $(B - R)$ color becomes progressively lower with R and moves objects with limiting colors behind the selection lines.

3.4.2 Absolute B Magnitudes

Quasar space densities are usually given in terms of the rest frame M_B magnitudes. This allows for the comparison of surveys at different redshifts. In making the transformation from observed r magnitudes to rest frame B, we have adopted a procedure identical to that of section 2.4.1, assuming $H_0 = 50$ km s^{-1} Mpc^{-1} and $q_0 = 0.5$ to aid in the comparison with other surveys. The final transformation is given in Eq. 2.12 and is repeated here:

$$M_B = AB_{1450} - 5\ \log[(c/H_0)A(z)/10pc] + 2.5\ \log(1+z) + 1.20\alpha + 0.12,$$

where AB_{1450} is the AB magnitude (Oke 1974) of the quasar at redshifted 1450Å and α is the slope of the power law continuum of the quasar. At our redshifts

of interest, the relation between m_r (or m_R) and AB_{1450} was computed using the model quasar spectra described above. For each spectrum, its flux at $(1+z)1450$Å was measured and the AB magnitude computed via Eq. 2.6. The model spectrum and an appropriate standard star were convolved with the r (or R) band filter curve and m_r (or m_R) computed. These "k-corrections" are then

$$k_r = AB_{1450} - m_r, \tag{3.1}$$

$$k_R = AB_{1450} - m_R. \tag{3.2}$$

The final expression is then

$$\begin{aligned} M_B = m_r - 5\ \log[(c/H_0)A(z)/10pc] + 2.5\ \log(1+z) \\ + 1.20\alpha + 0.12 + k_r, \end{aligned} \tag{3.3}$$

or the equivalent expression for m_R. The average values of k_r and k_R are given *vs.* redshift in Figure 3.13. For our adopted cosmology and a redshift of $z = 4.5$, this translates to an $M_B = -23.8^m$ for $r = 23.0^m$ (a typical r band selection limit) and to $M_B = -24.0^m$ for $R = 22.5^m$ (a typical R band selection limit).

3.4.3 Faint Quasars at z > 4

As mentioned above, we have not yet obtained spectra for most of our candidates (only seven out of 39 have been observed spectroscopically). The candidates that were examined lie in those areas of the color-color space where quasars are more likely to be found. Many of the remaining candidates lie just inside of the selection area, indicating that their red colors are more likely to be due to photometric scatter than are those farther away from the stellar locus. Given that we have yet to confirm any $z > 4$ quasars, even among the more promising candidates, it is reasonable to assume that we are not liable to find large numbers of quasars among our remaining candidates.

If we assume for the moment that none of our remaining candidates are $z > 4$ quasars, we have covered enough area to set limits on the QLF at $z > 4$ and $-26^m < M_B < -24^m$. We have computed selection probabilities for each data set and have developed a procedure for translating observed magnitudes to restframe B magnitudes. Now we need to calculate the effective volume of our survey given these selection probabilities (p) and over a given M_B range. As in Section 2.4.2, we use the $1/V_A$ estimator (e.g., Avni & Bahcall 1980) where V_A is the comoving volume over which a quasar could have been detected by our survey. We imagine that the survey is made up of a number of subsurveys of individual data sets divided into further subsurveys of interval $\Delta z = 0.1$ and $\Delta m = 0.1$. The area of each subsurvey is then the actual area multiplied by the detection probability $p(z, m_r)$ for that data set. The space density is computed as $\sum 1/\int p(z, m_r) dV_a$. In practice, we have asked, for each M_B and z, what is the probability of selecting a quasar with the properties assumed ($\alpha = -0.5$ and average line strengths)? We then integrate over $4 < z < 5$ with $\Delta z = 0.1$ to arrive at an effective volume for a particular M_B. We also compute an average z for that M_B by averaging over z weighted by the $p(z, m_r)$. We have computed these effective volumes for $-26^m < M_B < -24^m$. Beyond $M_B = -24^m$, the effective volume decreases dramatically due to the m_r limits of the survey. The effective volume then gives us a limiting space density for the survey, assuming that the number of $z > 4$ quasars contained in the survey is equal to or fewer than one.

These limiting space densities are plotted for two M_B ranges in Figure 3.14 along with the results from the KDC and SSG surveys. The Boyle (1991), Hewett et al. (1993), and Hawkins & Véron (1995) $z = 2$ QLF's are shown for comparison. We have also scaled the Boyle and Hewett et al. functions down in density to coincide with the SSG and KDC points (pure density evolution). If we assume that the shape of the Boyle and Hewett et al. functions are preserved as we go from $z = 2$ to $z = 4$, we have surveyed enough effective area to have discovered

$\sim$one $z > 4$ quasar. While we are not sensitive to a turnover in the QLF at $z = 4$ as compared to $z = 2$ (luminosity dependent density evolution), once spectroscopy is complete, we should be able to limit the shape of the QLF, i.e., test if the QLF is described by a double power law as suggested by Boyle and Hewett et al., or the single power law of Hawkins & Veron.

3.4.4 Effects of Clustering

Quasar clustering has been fairly well established at $z < 2$ (Hartwick & Schade 1990, Bahcall & Chokshi 1991) and its strength probably decreases with redshift (Iovino et al. 1991). This clustering most likely reflects the growth of large-scale structure. What we are looking for is a different phenomenon: the clustering of quasars due to initial fluctuations in the primordial density field. It has been suggested by Efstathiou and Rees (1988) that $z > 4$ quasars should be clustered as strongly as bright galaxies today. Cole and Kaiser (1989) suggest this clustering could be intermediate between bright galaxies and rich clusters. This CCD survey was originally designed to look for such protoclusters in the fields around known quasars (Djorgovski et al. 1991, Djorgovski et al. 1992b, Smith et al. 1993).

A commonly used tool for studying galaxy and quasar clustering has been the two-point spatial correlation function. This two-point correlation function $\xi(r)$ is the excess number of objects one would expect to find within a distance r of a given object over the number one would expect if the objects were distributed randomly:

$$\xi(r) = \frac{N_{observed} - N_{expected}}{N_{expected}}. \tag{3.4}$$

Taking the suggestion of Efstathiou and Rees, we will assume that quasar clustering at high redshift is similar to that of galaxies today. The two point

correlation function for galaxies at $z \sim 0$ is usually described by a power law of the form

$$\xi = (r/r_0)^{-\gamma}, \tag{3.5}$$

where $\gamma = 1.8$ and r_0 is the correlation scale length (Peebles 1980, 1993). The probability of finding that a quasar has a neighbor at distance r in δV is

$$\delta P = \rho \delta V[1 + \xi(r)], \tag{3.6}$$

where ρ is the average density. The mean number of neighbors within a volume V containing a randomly chosen object is then

$$\langle N \rangle = \rho V + \rho \int \xi(r) dV. \tag{3.7}$$

The density with clustering within this volume V, ρ_{clus}, is given as

$$\frac{\langle N \rangle}{V} = \rho_{clus} = \rho + \rho \frac{\int \xi(r) dV}{V}, \tag{3.8}$$

and the ratio of the clustered density to the average background density within V is

$$\frac{\rho_{clus}}{\rho} = 1 + \frac{\int \xi(r) dV}{V}. \tag{3.9}$$

Substituting Eq. 3.5 into Eq. 3.9 and integrating over a survey field area from $z = 4$ to $z = 5$ (placing the known quasar at the center of the volume and assuming comoving coordinates), we arrive at an expression for ρ_{clus}/ρ in terms of r_0. This relation is plotted in Figure 3.15 for three different values of q_0 (assuming $H_0 = 50$ km sec^{-1} Mpc $^{-1}$).

Assuming that quasars at high redshift have correlation lengths similar to galaxies today, expected values of r_0 range from 10 to 50 Mpc (Bahcall & Soneira 1983, Dalton et al. 1994, Martinez & Coles 1994). If quasar space densities do scale with redshift as described in the preceding section, our results exclude large values of r_0 for an $\Omega_0 = 1$ universe, as large overdensities are expected in this

case. In a $q_0 = 0.1$ universe with, for example, $r_0 = 30$ Mpc, $\rho_{clus}/\rho = 1.22$, which means that if we are just surveying enough area to see one quasar not associated with clustering, we would need to cover 4.5 times our current number of fields, all containing high redshift quasars, to detect one associated quasar, or around 150 fields. While this number is not outrageous, considering that there are only on the order of $\sim$60 $z > 4$ quasars currently known, the prospects of detecting such clustering in the very near future are not high. However, at least one large survey for bright quasars at $z > 4$ is currently under way (Kennefick et al. 1995ab, Darling et al. 1996) which should provide more objects for such investigations.

3.5 Discussion

We have conducted a multicolor CCD survey for quasars at $4 < z < 5$ covering 0.69 square degrees. Assuming that none of our remaining candidates are high redshift quasars, the area covered has allowed us to constrain the QLF at faint ($-26^m < M_B < -24^m$) magnitudes. Combining our data with that of surveys at brighter magnitudes, our results are consistent with a pure density evolution decrease in the number of objects from $z = 2$ to $z = 4$.

Hall et al. (1996) and Osmer et al. (1996) report initial results from an 0.83 square degree multicolor CCD survey for quasars in six bands, UVB and three filters centered at 6615, 7425, and 8586 Å. Their selection criteria for $z > 4$ candidates are similar to ours as are their limiting magnitudes. They are still performing follow-up spectroscopy, and have identified one $z > 4$ quasar ($z = 4.33$), a relatively bright object at $R = 20.09^m$ ($M_B \sim -26^m$). They have yet to identify any faint quasars at $z > 4$, and so their initial results are consistent with our own.

Our current coverage is not enough to significantly constrain quasar clustering at $z \gtrsim 4$. Expected space densities for even faint quasars at these redshifts requires that at least a few square degrees must be surveyed to guarantee the recovery of even one quasar. If there is clustering at a strength comparable to that of galaxies today, this would result in overdensities of perhaps 20% in the volume covered by one of our survey fields. Therefore, in order to be sensitive to clustering at these redshifts, one must survey many fields around known high redshift quasars. Fortunately, the number of known quasars at $z > 4$ continues to increase (Kennefick et al. 1995ab), and soon it may be possible to carry out such a targeted search capable of detecting these structures.

Such structures may have already been found. Schneider et al. (1994) report the discovery of three pairs of quasars at $z > 3$, separated by only a few Mpc in projection, in the course of their CCD transit grism survey. The survey covered

61.5 square degrees and detected 90 quasars through their Lyα emission. The probability of finding these pairs in their survey if no clustering is present is only 2×10^{-4}. They found one pair per 30 quasars detected, which means a survey for clustering must contain on the order of ~ 100 known $z > 4$ quasars to be sensitive to such clustering.

Most bright ($M_B < -27$) quasars at $z > 4$ were discovered using photographic plates, as large areas (tens of square degrees) are needed to find such objects. Unfortunately, photographic plates are not effective at fainter magnitudes and CCD surveys are needed due to their greater quantum efficiencies, especially at red wavelengths where most of the flux from quasars at $z > 4$ is detected. Fortunately, large format CCDs are becoming more common. The Hall et al. (1996) and Osmer et al. (1996) survey discussed above employed a Tektronix 2048×2048 CCD with a scale of $0.529''$/pixel, allowing them to cover their 0.83 deg^2 with only 12 pointings. Given the low surface density of faint $z > 4$ quasars expected, a larger survey area is clearly needed, and the current large format CCD's make such a survey possible.

Future surveys aimed at covering large areas of sky will certainly be able to determine faint $z > 4$ quasar space densities to a high level of confidence. In the meantime, we have shown that even with current technology, CCD programs designed to cover only a few square degrees are feasible and should start to give us a good handle on the evolution of the faint quasar population.

TABLE 3.1: *gri* CCD Observations

Field	z	Field Center		UT Date	Instrument	Seeing	Detection Limits			Area	Ref.
		α (1950)	δ (1950)			($''$)	g	r	i	(deg^2)	
Q 0000−26	4.10	00 00 49.5	−26 20 01	1992 Sep 01	CTIO 4m	2.2	23.8	23.2	23.6	0.018	1
Q 0051−279 Set B	4.40	00 51 35.9	−27 55 21	1992 Oct 01	4Shooter	1.3	24.0	23.7	22.8	0.015	2
Q 0051−279 Set C	4.40	00 51 39.8	−28 01 58	1992 Oct 02	4Shooter	1.5	24.0	23.6	22.8	0.012	2
Q 0101−304	4.07	01 01 14.1	−30 25 04	1992 Sep 01	CTIO 4m	2.1	23.5	23.2	22.8	0.017	2
BRI 0103+00	4.43	01 03 45.3	+00 32 21	1994 Sep 01	COSMIC	1.0	24.9	24.6	24.0	0.022	3
PC 0104+0215	4.17	01 04 12.3	+02 16 53	1992 Oct 01	4Shooter	1.1	24.2	24.0	23.1	0.018	4
PC 0307+0222 Set A	4.38	03 07 24.2	+02 19 50	1990 Oct 17	4Shooter	1.0	24.1	23.8	23.2	0.015	4
PC 0307+0222 Set B	4.38	03 06 52.7	+02 18 46	1993 Sep 25	4Shooter	1.1	24.2	24.0	23.4	0.020	4
PC 0307+0222 Set C	4.38	03 07 06.5	+02 24 22	1994 Feb 10	4Shooter	0.9	24.1	23.8	23.4	0.016	4
PC 0751+5623	4.28	07 51 44.8	+56 22 31	1994 Feb 10	4Shooter	1.0	24.4	24.4	24.1	0.018	4
PC 0910+5625	4.04	09 11 22.1	+56 23 34	1991 Jan 10	4Shooter	1.3	24.1	24.1	23.2	0.019	4
PC 0953+4749	4.46	09 53 21.7	+47 47 36	1994 Feb 10	4Shooter	1.1	24.1	23.5	23.6	0.014	4
BRI 1013+00	4.38	10 13 17.2	+00 34 40	1994 Feb 10	4Shooter	1.2	24.2	23.7	23.6	0.019	5
BRI 1050−00 Set A	4.29	10 50 50.0	−00 00 51	1993 Jun 12	4Shooter	1.2	24.1	23.6	23.0	0.005	5
PC 1158+4635	4.73	11 58 07.8	+46 34 30	1993 May 26	4Shooter	1.2	24.3	23.5	23.5	0.018	4
PC 1233+4752	4.45	12 33 08.3	+47 52 37	1992 May 01	COSMIC	1.1	23.6	23.3	22.7	0.025	4
PC 1247+3406 Set A	4.90	12 47 28.6	+34 04 16	1992 Mar 30	4Shooter	1.2	23.7	23.5	22.6	0.019	6
PC 1247+3406 Set B	4.90	12 47 09.5	+34 07 39	1992 Apr 30	4Shooter	1.4	23.5	23.0	22.9	0.014	6

TABLE 3.1: *gri* CCD Observations (Cont.'d)

Field	z	Field Center		UT Date	Instrument	Seeing	Detection Limits			Area	Ref.
		α (1950)	δ (1950)			(″)	g	r	i	(deg^2)	
RXJ 1759+6638	4.32	17 59 28.8	+66 38 56	1994 Aug 09	COSMIC	1.4	24.1	24.0	23.5	0.021	7
Q 2203+292 Set B	4.40	22 03 58.4	+29 13 42	1988 Sep 11	4Shooter	1.1	24.1	23.5	23.1	0.007	8
Q 2203+292 Set C	4.40	22 04 17.3	+29 11 07	1992 Oct 01	4Shooter	1.0	24.2	24.0	23.4	0.019	8
Q 2203+292 Set D	4.40	22 04 08.1	+29 18 55	1993 Sep 24	4Shooter	1.0	23.6	23.3	23.1	0.013	8
BRI 2235−03	4.23	22 35 47.5	−03 01 30	1994 Aug 09	COSMIC	1.2	24.6	24.6	23.5	0.024	3
PC 2331+0216	4.10	23 31 58.5	+02 16 47	1992 Sep 02	CTIO 4m	1.8	24.0	23.6	23.5	0.018	4
FP 0031+23	–	00 31 20.3	+23 35 00	1992 Oct 02	4Shooter	1.5	24.2	23.7	23.1	0.019	9
FP 0241+31	–	02 41 30.0	+31 40 00	1992 Nov 19	4Shooter	1.7	23.6	23.3	23.0	0.018	9
FP 0738+34	–	07 38 25.0	+34 41 00	1992 Nov 19	4Shooter	1.4	23.7	23.6	23.1	0.018	9
FP 1333+30	–	13 32 49.0	+30 01 28	1992 May 01	4Shooter	1.1	24.2	24.0	23.4	0.019	9
FP 1454+34	–	14 54 44.0	+34 12 09	1992 Mar 30	4Shooter	1.0	24.6	24.1	23.8	0.018	9
FP 1606+34	–	16 06 33.0	+34 52 30	1992 May 01	4Shooter	1.2	24.8	24.3	23.6	0.019	9

(1) Webb *et al.* 1988 (2) Warren *et al.* 1987b (3) Smith *et al.* 1994b (4) Schneider *et al.* 1994 (5) Smith *et al.* 1994a (6) Schndeider *et al.* 1991b (7) Henry *et al.* 1994 (8) McCarthy *et al.* 1988 (9) Thompson 1995

TABLE 3.2: *BRI* CCD Observations

Field	z	Field Center		UT Date	Instrument	Seeing	Detection Limits			Area	Ref.
		α (1950)	δ (1950)			($''$)	B	R	I	(deg^2)	
Q 0051−279 Set A	4.40	00 51 49.8	−27 58 24	1991 Oct 03	CTIO 4m	1.3	25.0	24.2	22.7	0.012	1
BR 0945−0411	4.14	09 45 15.0	−04 11 30	1994 Apr 13	EMMI	0.8	23.7	23.2	22.2	0.020	2
BR 0951−0450	4.37	09 51 15.0	−04 50 30	1994 Apr 13	EMMI	0.8	24.2	23.6	22.6	0.020	2
BR 1033−0327	4.50	10 33 51.5	−03 27 46	1994 Apr 14	EMMI	0.9	24.1	23.6	22.8	0.020	3
BRI 1050−00 Set B	4.29	10 50 46.7	−00 00 02	1994 Apr 14	EMMI	0.9	24.2	23.7	22.7	0.020	4
BR 1202−0725	4.70	12 02 49.2	−07 25 50	1994 Apr 13	EMMI	0.9	24.0	23.4	22.5	0.020	5
BRI 1328−0433 Set A	4.20	13 28 15.0	−04 33 30	1994 Apr 12	EMMI	0.7	24.1	23.6	22.7	0.017	2
BRI 1328−0433 Set B	4.20	13 28 45.0	−04 33 30	1994 Apr 14	EMMI	0.9	24.1	23.6	22.6	0.020	2
BRI 1500+08	3.96	15 00 18.2	+08 24 49	1994 Apr 12	EMMI	0.9	24.1	23.5	22.5	0.020	6

1) Warren *et al.* 1987b (2) this work (3) Williger *et al.* 1994 (4) Smith *et al.* 1994a (5) McMahon *et al.* 1994 (6) Smith *et al.* 1994b

TABLE 3.3: Coordinates, redshifts, and R magnitudes for the BRI Quasars

QSO	α (1950)	δ (1950)	z	R
BR 0945−0411	09 45 18.6	−04 11 18	4.14±0.01	19.1±0.2
BR 0951−0450	09 51 25.0	−04 50 07	4.37±0.02	19.1±0.2
BRI 1328−0433	13 28 55.0	−04 33 26	4.20±0.01	19.3±0.1

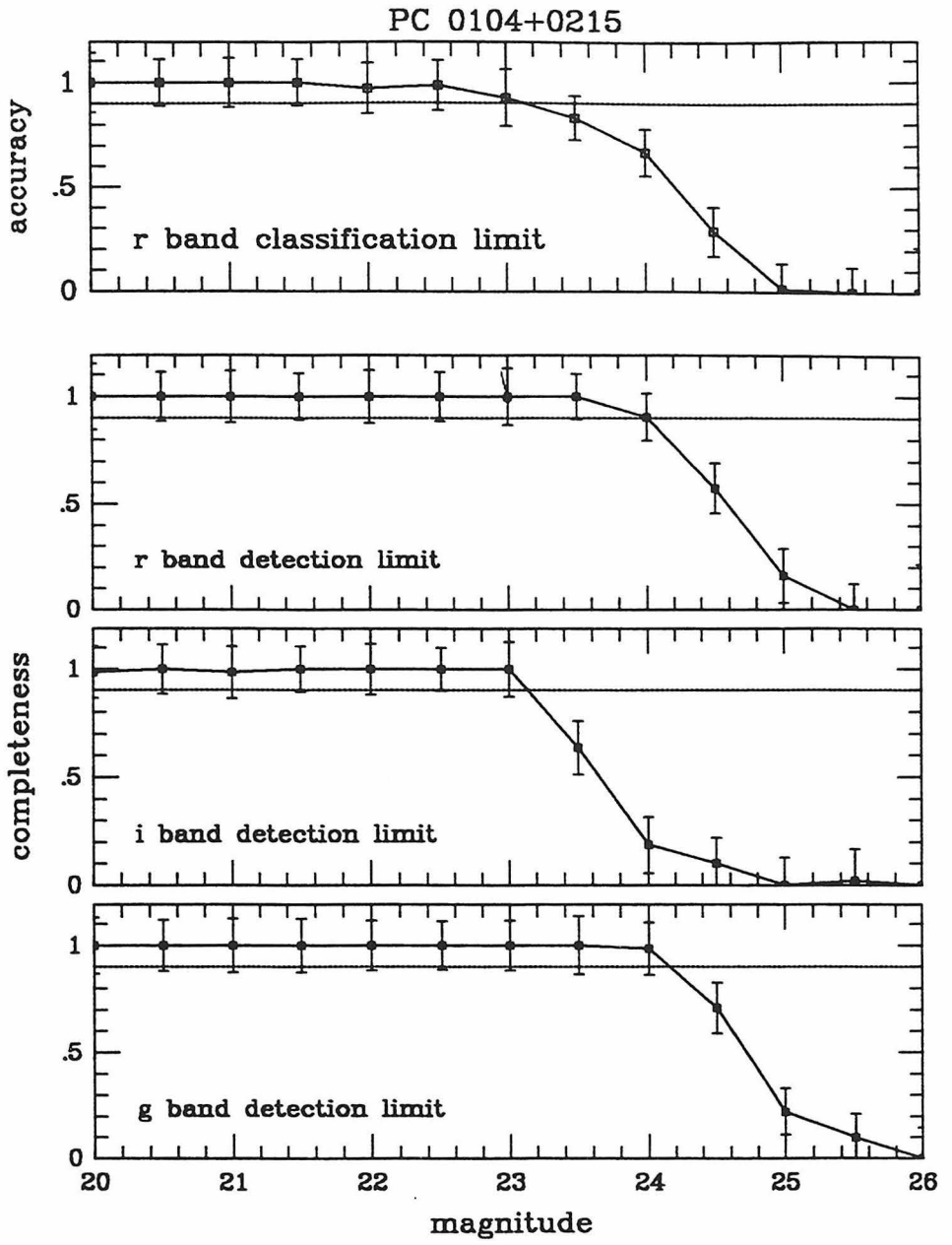

Figure 3.1: Detection and Classification Limits

Detection and classification limits of stellar objects for a typical data set as found from Monte Carlo simulations. The detection limit is taken to be the magnitude where the completeness falls below 90% (dotted line). The classification limit is on average one magnitude above the detection limit in r. To assure accurate classification, objects are selected as candidates only if their r magnitudes are at least one magnitude above the detection limit. Error bars are $1/\sqrt{N}$, where N is the number of simulated sources in that magnitude bin.

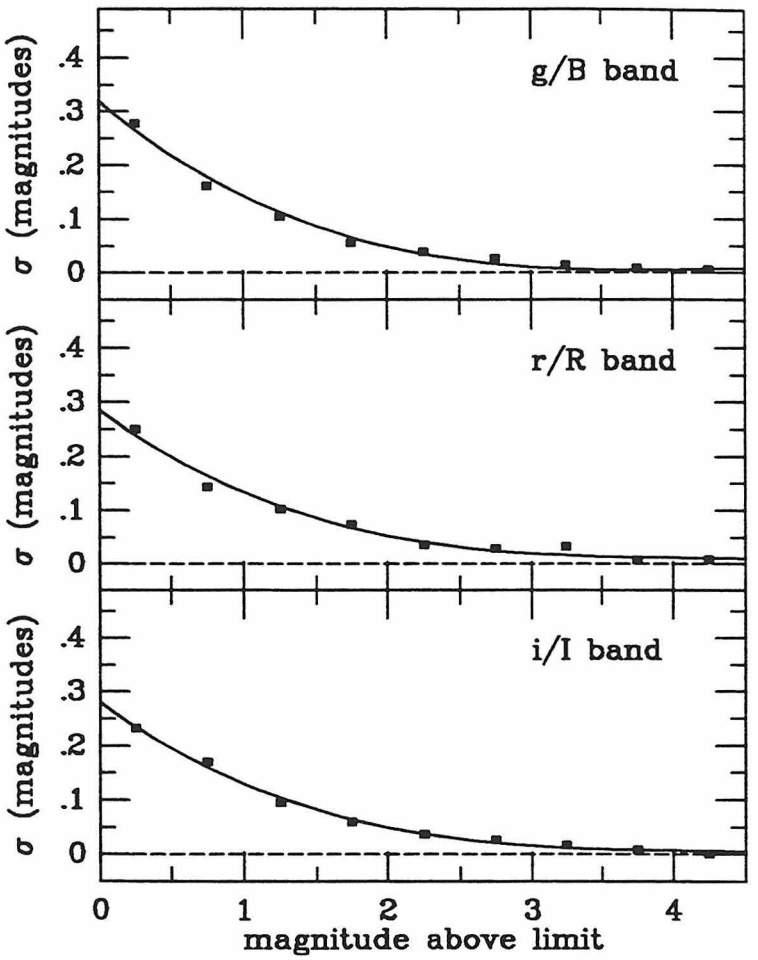

Figure 3.2: Random Errors

The random photometric errors for each band as calculated from the Monte Carlo simulations plotted *vs.* the magnitude above the detection limit of the data.

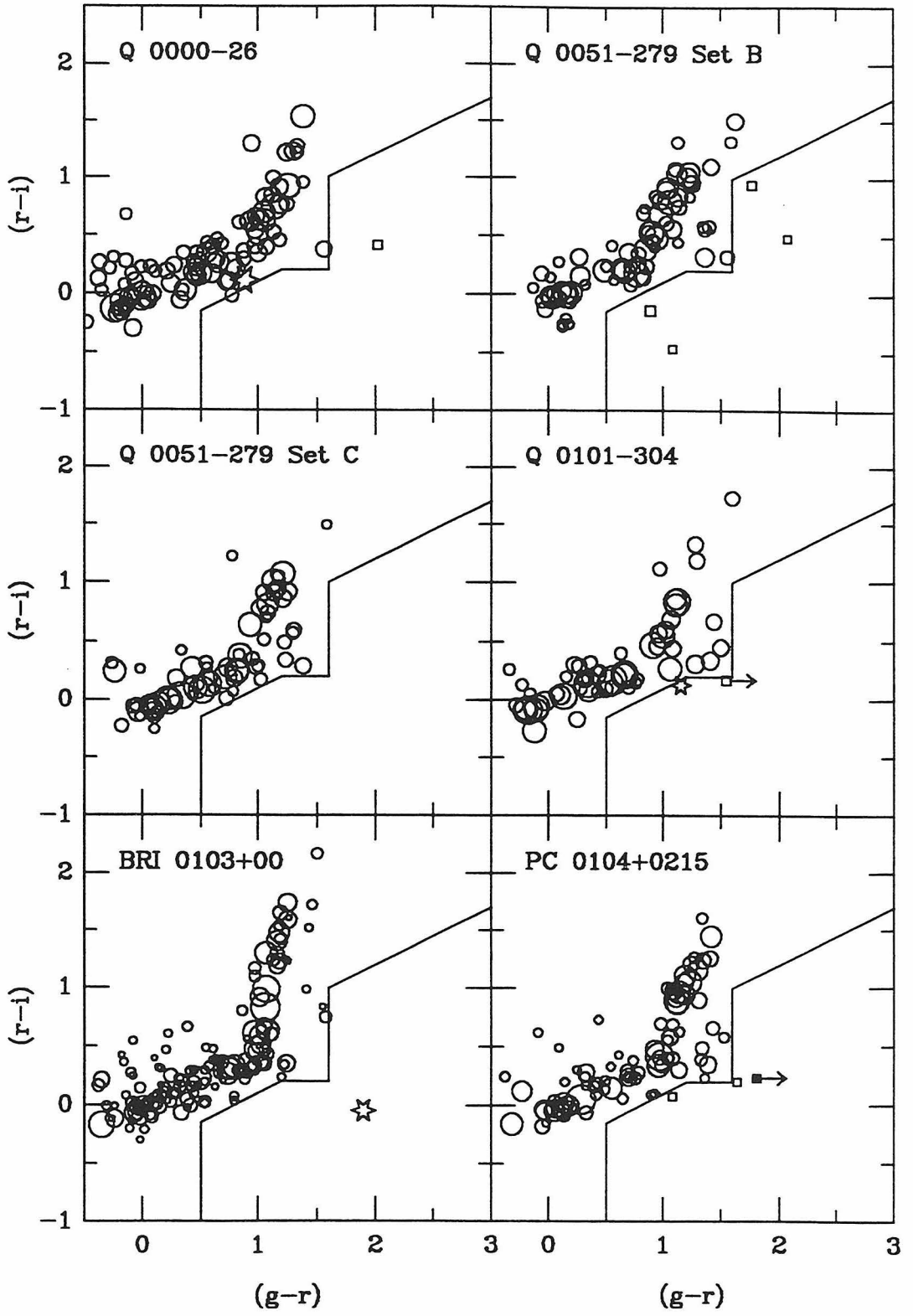
Q 0000−26
Q 0051−279 Set B
Q 0051−279 Set C
Q 0101−304
BRI 0103+00
PC 0104+0215
(r−i)
(g−r)
2
1
0
−1
3

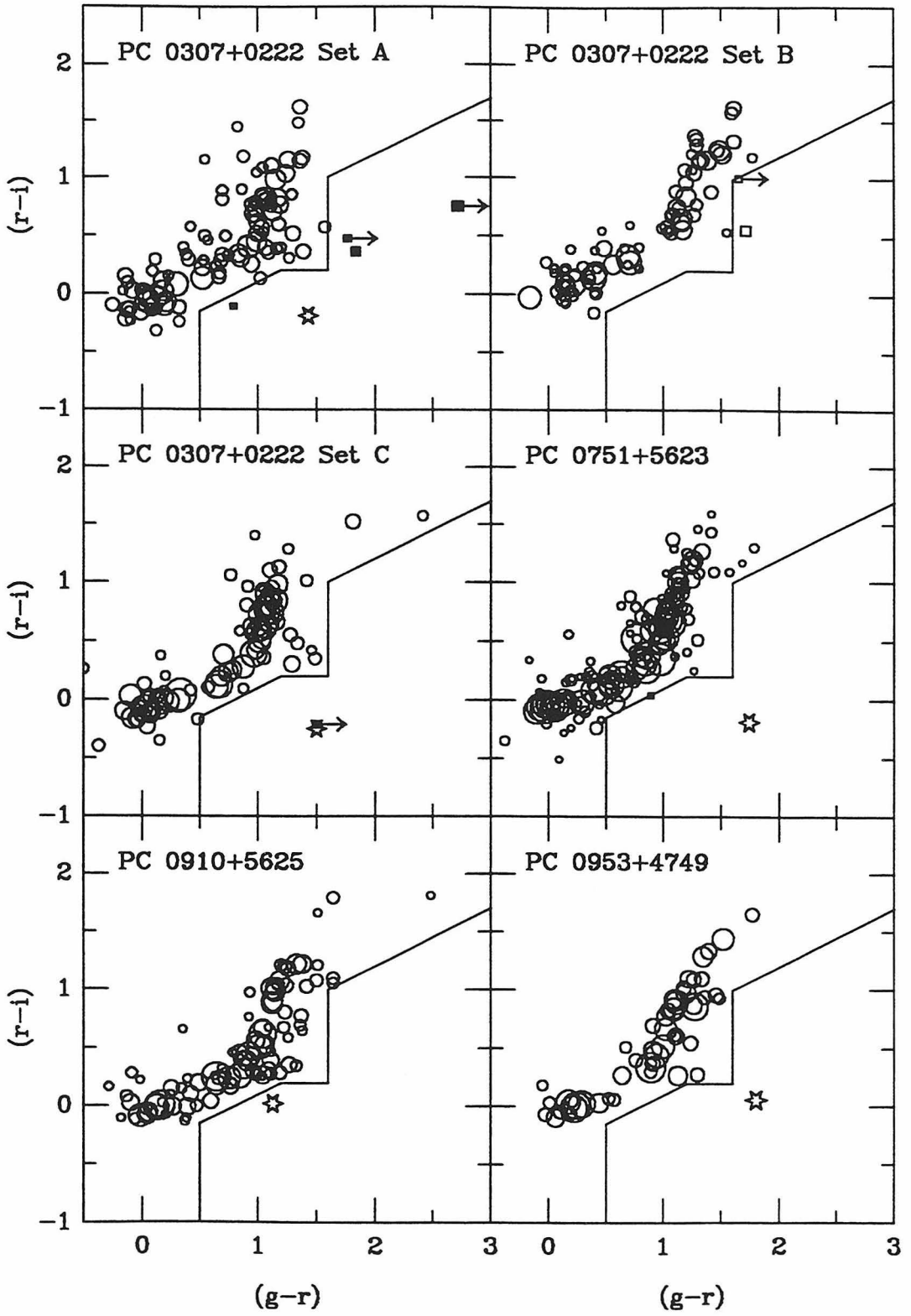
PC 0307+0222 Set A
PC 0307+0222 Set B
PC 0307+0222 Set C
PC 0751+5623
PC 0910+5625
PC 0953+4749
(r−i)
(g−r)
2
1
0
−1
0
1
2
3

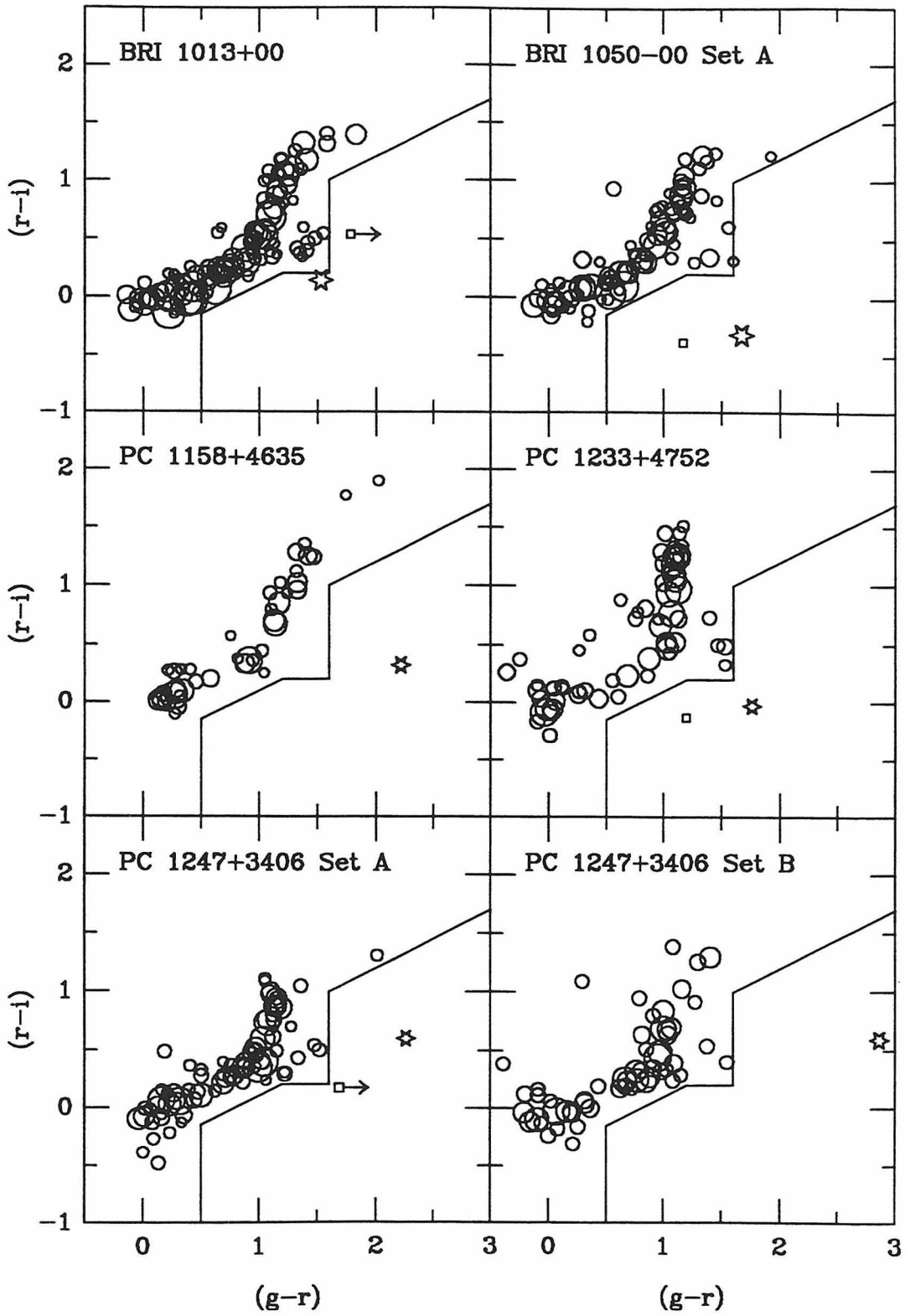
BRI 1013+00
BRI 1050−00 Set A
PC 1158+4635
PC 1233+4752
PC 1247+3406 Set A
PC 1247+3406 Set B
(r−i)
(g−r)
2
1
0
−1
3

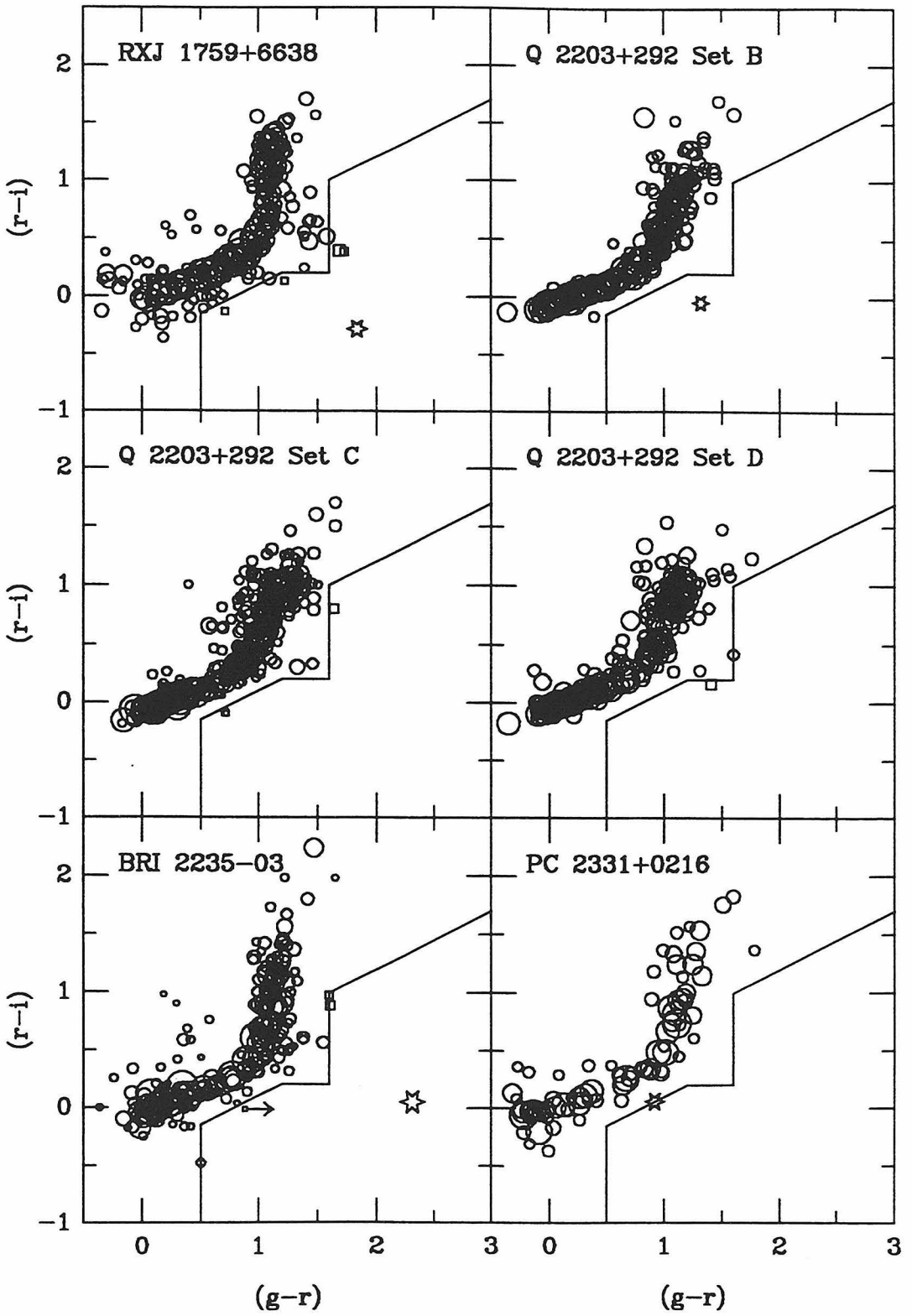
RXJ 1759+6638
Q 2203+292 Set B
Q 2203+292 Set C
Q 2203+292 Set D
BRI 2235−03
PC 2331+0216
(r−i)
(g−r)
2
1
0
−1
3

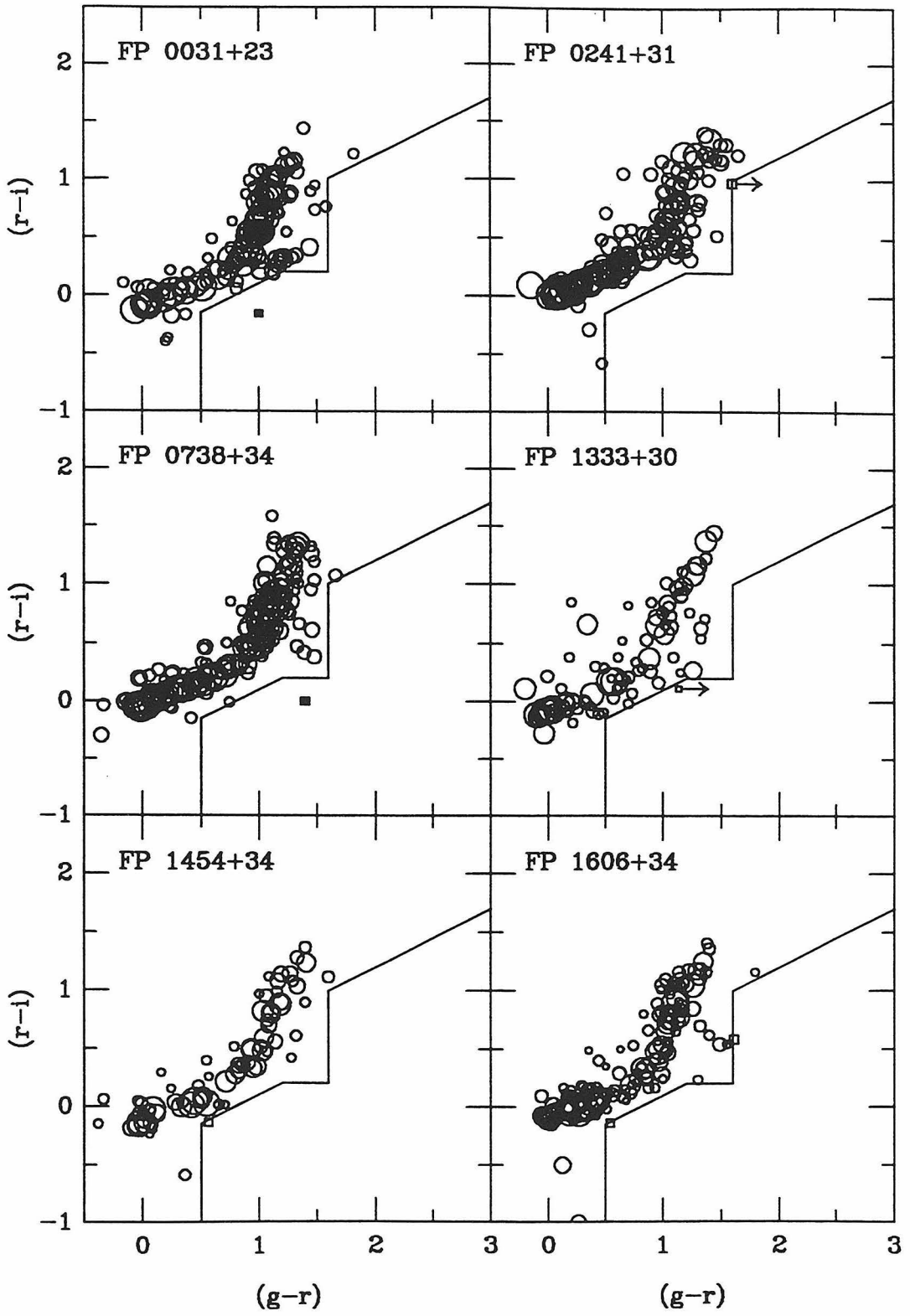
FP 0031+23
FP 0241+31
FP 0738+34
FP 1333+30
FP 1454+34
FP 1606+34
(r−i)
(g−r)
2
1
0
−1
0
1
2
3

Figure 3.3: *gri* **Color-Color Diagrams**

The color-color diagrams of the stellar objects in each data set with r magnitudes above the selection limit of the data. Known quasars are shown as open stars. Final selection limits for this survey are shown as the solid lines. Objects are chosen as candidates if they fall to the right of or below these lines. Candidates are shown as squares, with filled squares indicating that follow-up spectroscopy has been obtained. Candidates with limiting $(g - r)$ colors are indicated with an arrow pointing off to the right. The symbol size scales with the r magnitude.

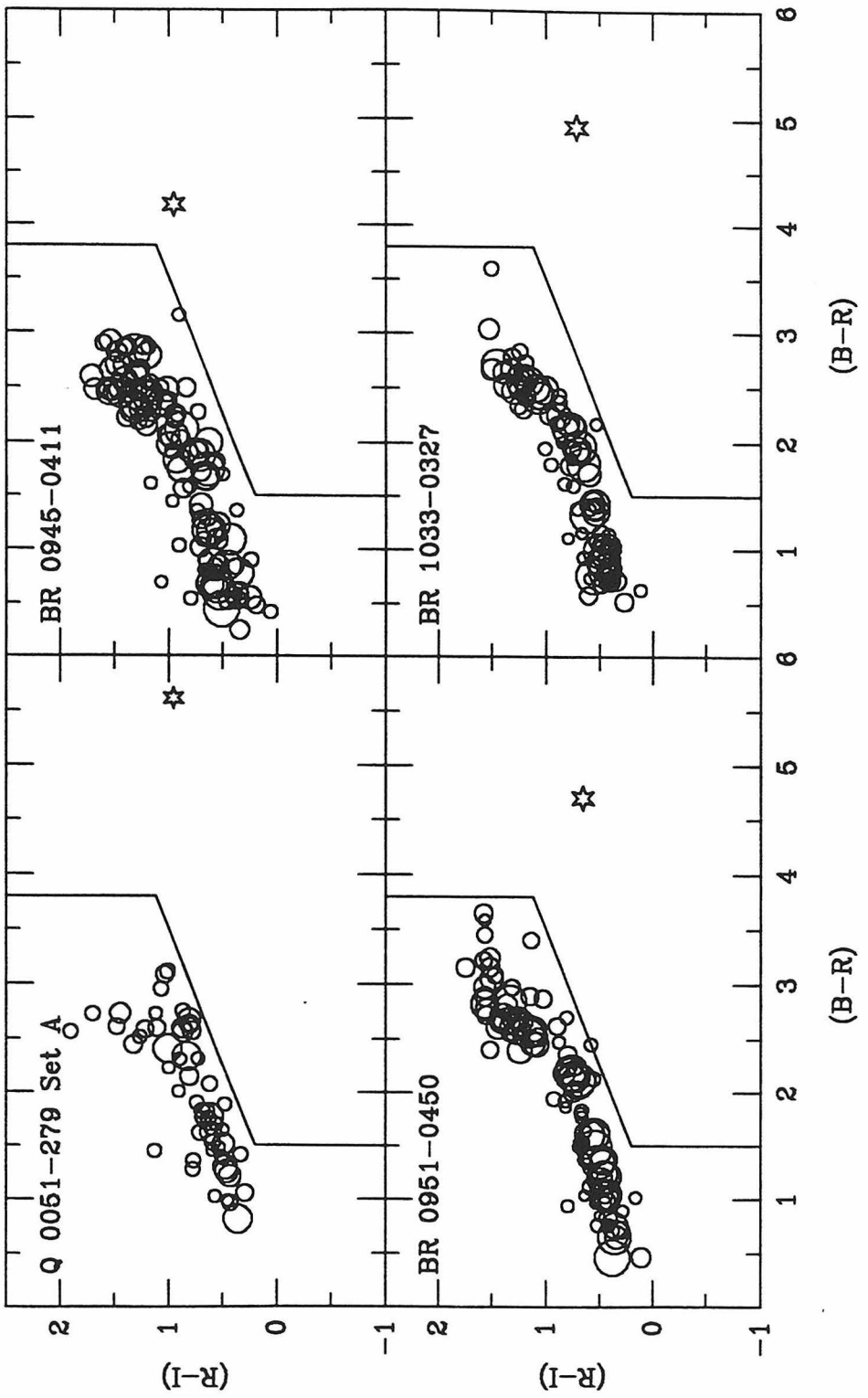
Q 0051−279 Set A
BR 0945−0411
BR 0951−0450
BR 1033−0327
(R−I)
(B−R)

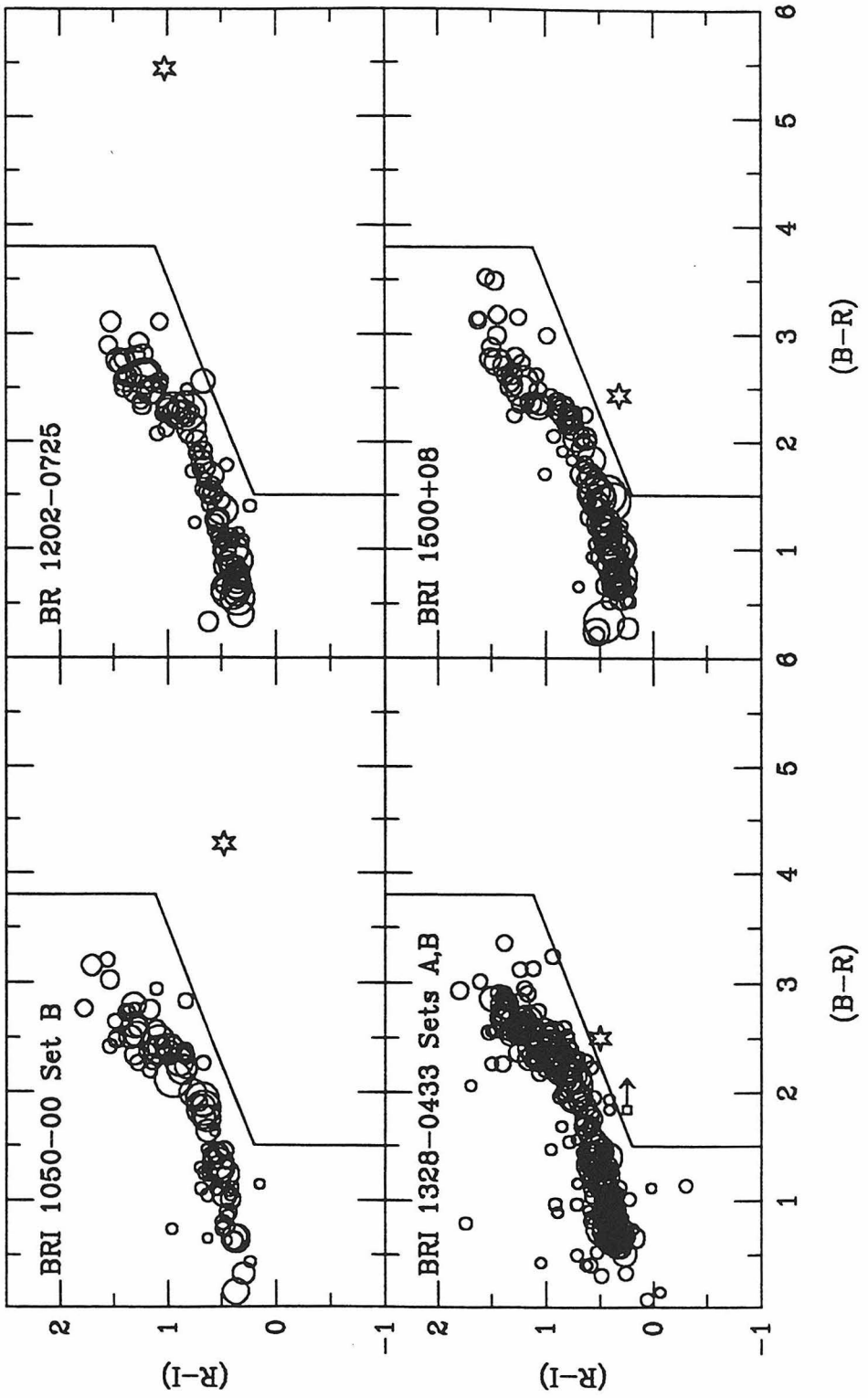
BR 1202−0725
BRI 1500+08
BRI 1050−00 Set B
BRI 1328−0433 Sets A,B
(R−I)
(B−R)

Figure 3.4: *BRI* Color-Color Diagrams

Same as Figure 3.3, but for the *BRI* data sets. Only one candidate was chosen from these fields.

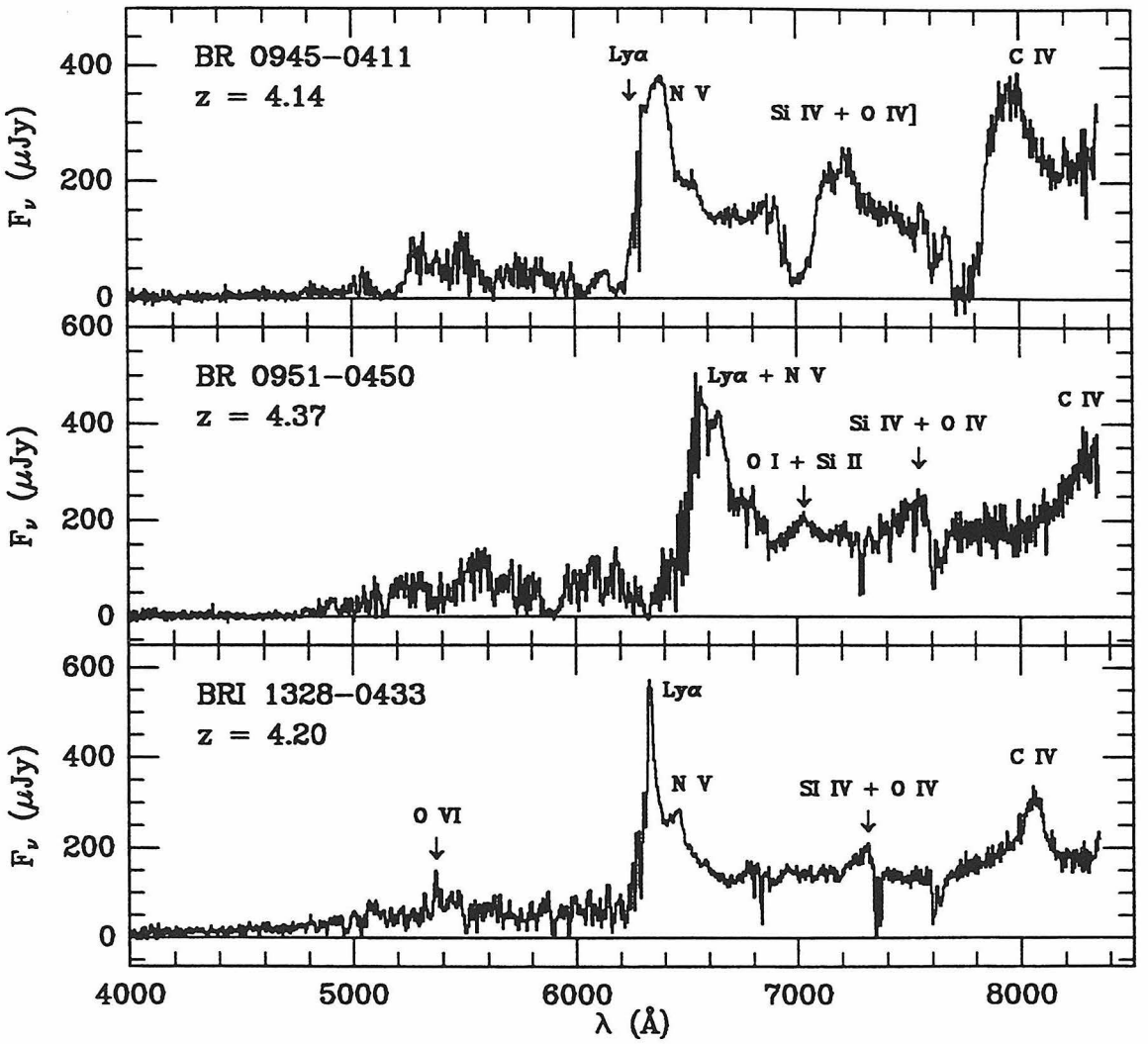

Figure 3.5: Spectra of BRI Quasars

EMMI spectra of the three BRI quasars recovered during the course of this survey. Obvious emission lines are labeled. BR 0945−0411 exhibits characteristics of a BAL quasar.

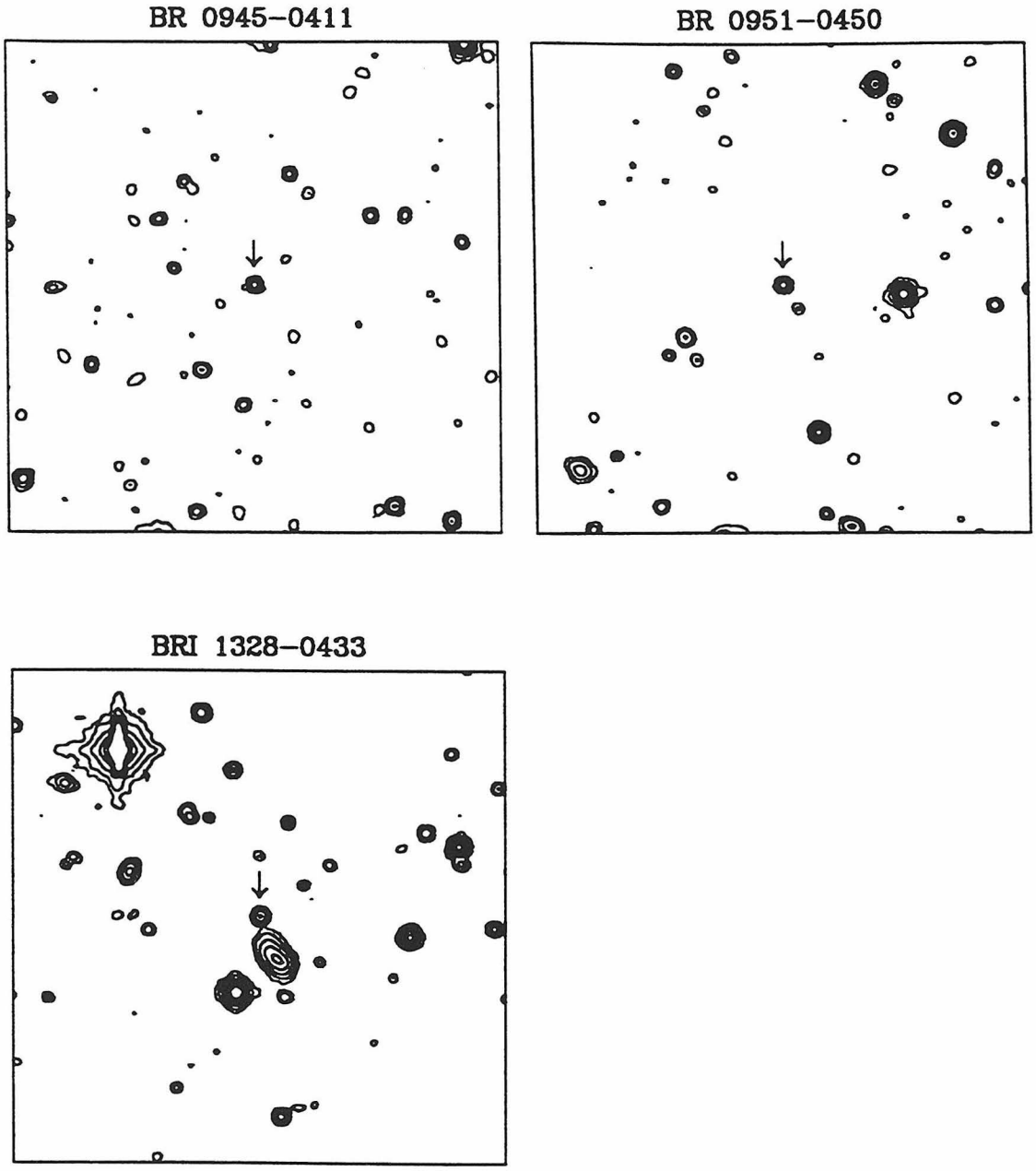

Figure 3.6: Finding Charts of BRI Quasars

Contour plots of R band images of the three BRI quasars obtained with EMMI on the ESO NTT during UT 1994 April 12-14. All images are 2 armin square with N up and E to the left.

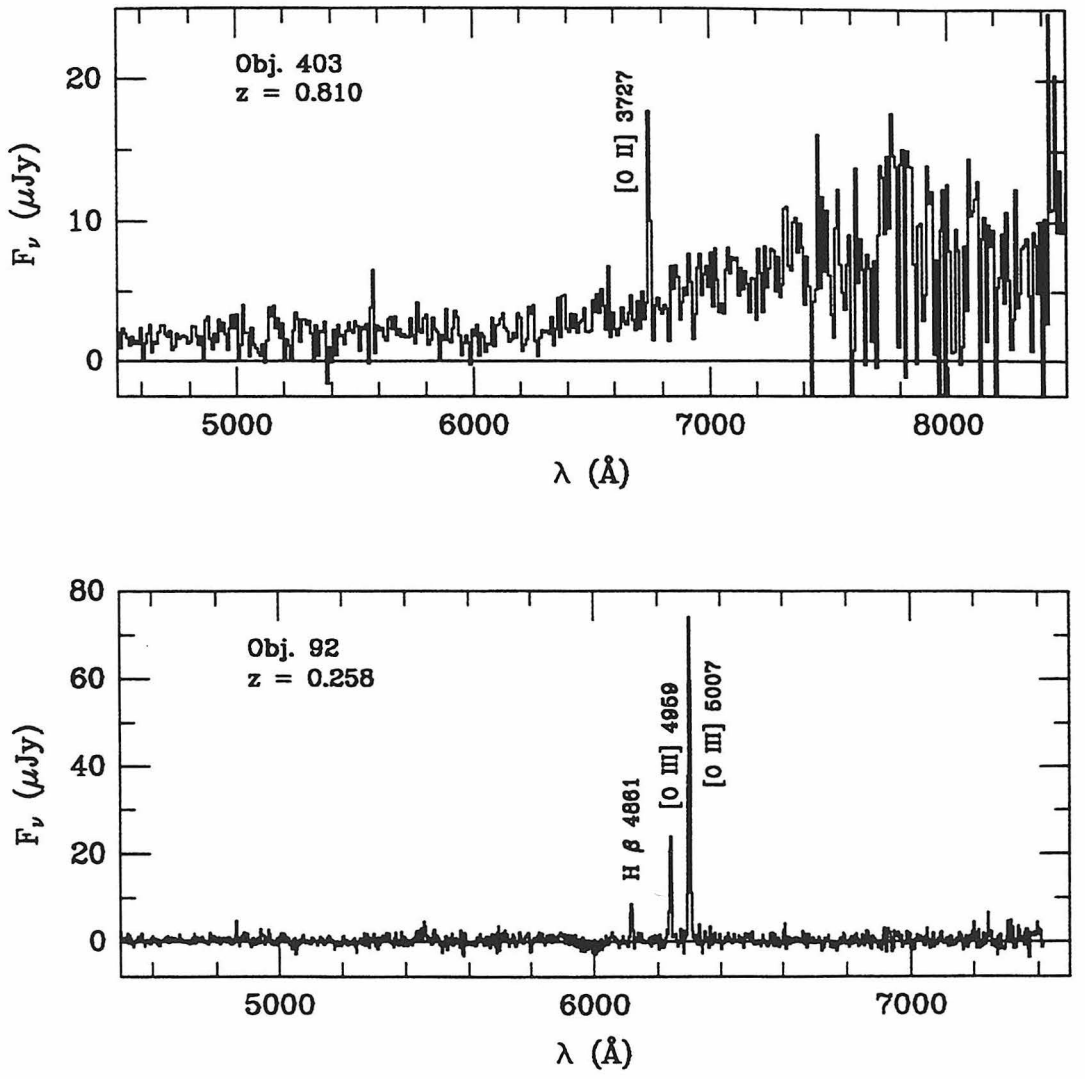

Figure 3.7: Galaxies at $z < 1$

Spectra of two candidates from the Q2203+29 field selected after an initial reduction of the data. Both candidates are too faint ($r \sim 23.5^m$) to be included in the final candidate list. These objects demonstrate how galaxies at $z < 1$ can mimic the colors of high redshift quasars.

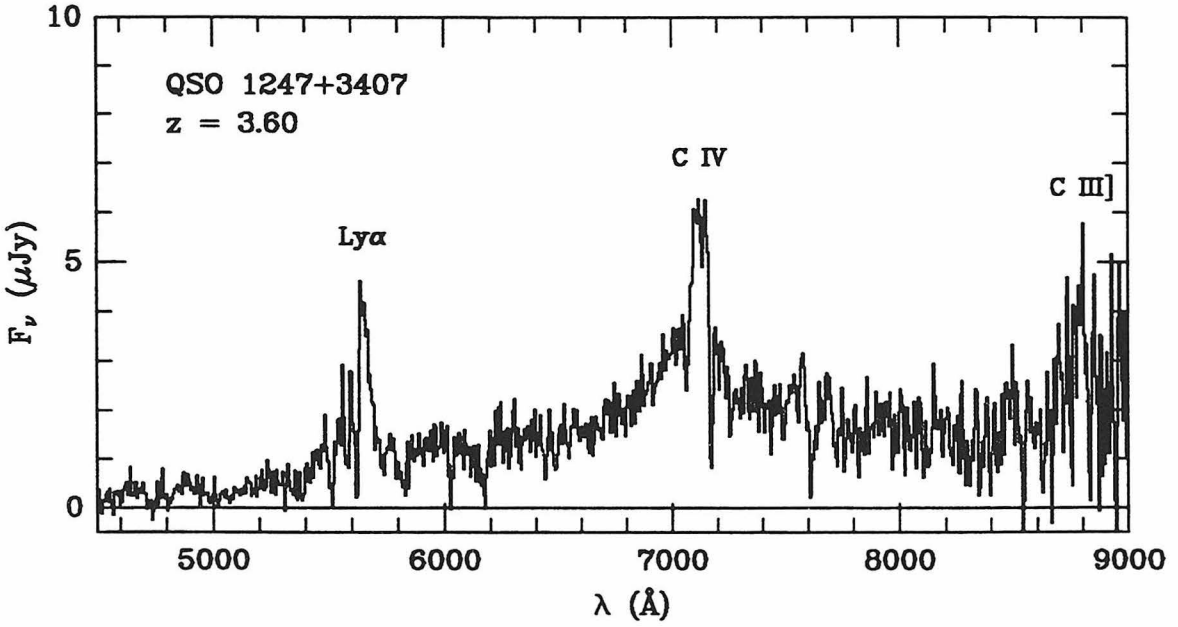

Figure 3.8: QSO 1247+3407 Spectrum

A Keck LRIS spectrum of a $z = 3.60$ quasar discovered in the course of this survey. The peculiar spectrum shows a weak Lyα line and a continuum weaker between the Lyα and C IV lines than is typical of quasars at these redshifts. These features resulted in its having a relatively red color and caused it to be initially selected for follow-up spectroscopy.

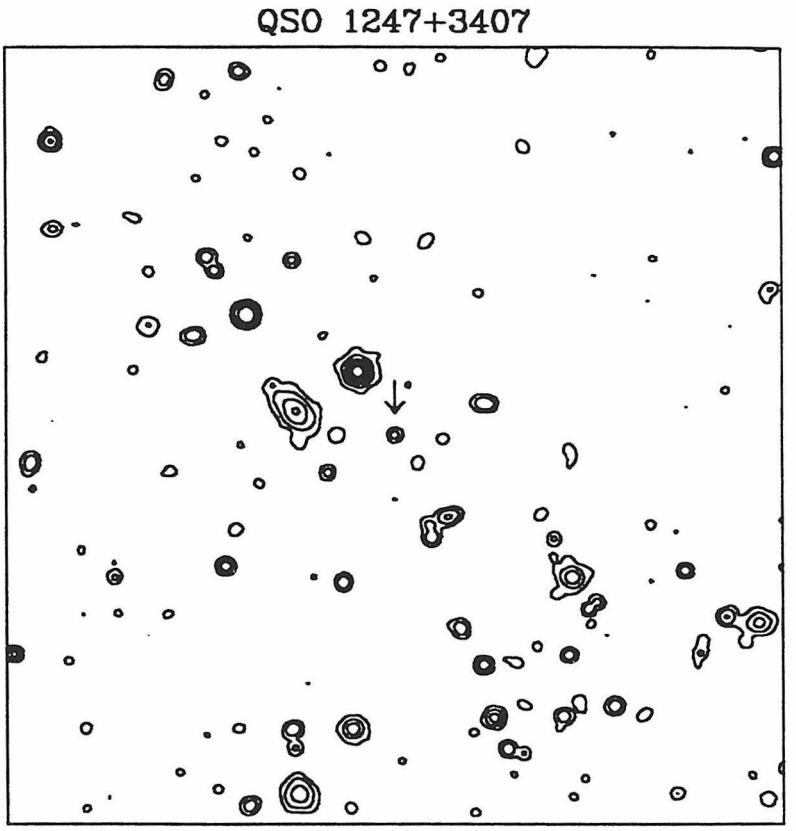

Figure 3.9: QSO 1247+3407 Finding Chart

Contour plot of an R band image of QSO 1247+3407 obtained at the Keck 10-meter telescope on UT 1994 April 10. The image is 2 arcmin square with N up and E to the left.

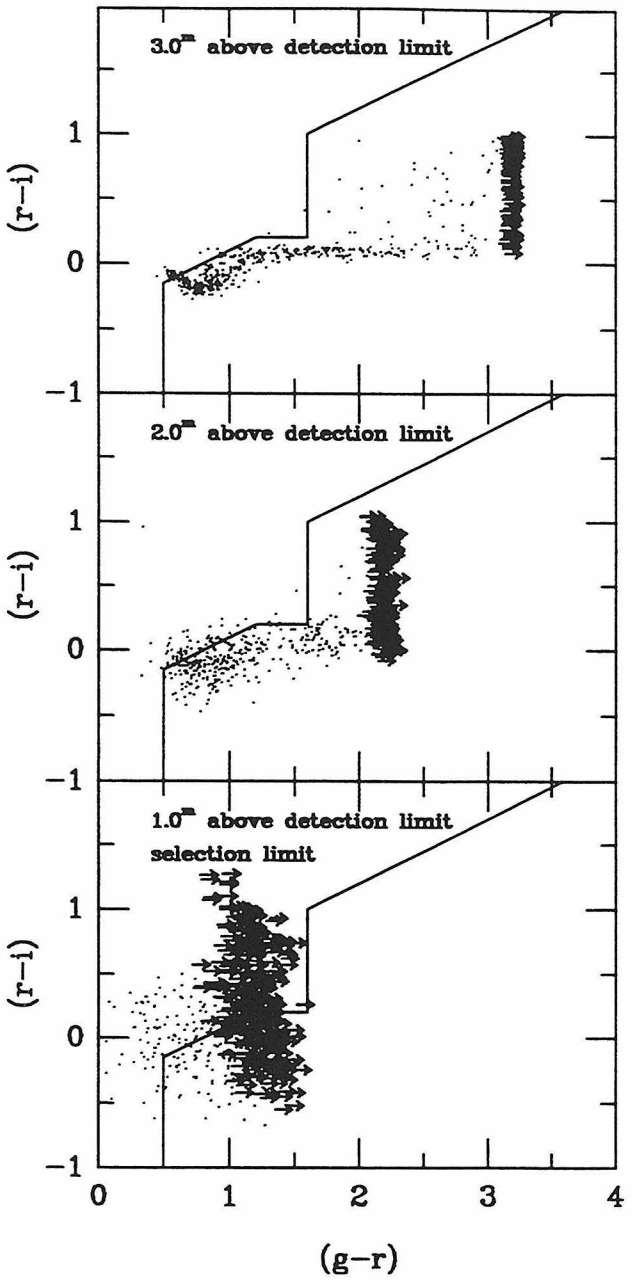

Figure 3.10: Model Quasar *gri* Colors

Quasar colors for a typical *gri* data set computed from model quasar spectra. Errors have been added for three different r magnitudes: (top) 3 magnitudes above the detection limit, (middle) 2 magnitudes above, and (bottom) 1 magnitude above or at the selection limit. Arrows denote the cases where the quasar would have a limiting $(g - r)$ color. The selection lines are shown.

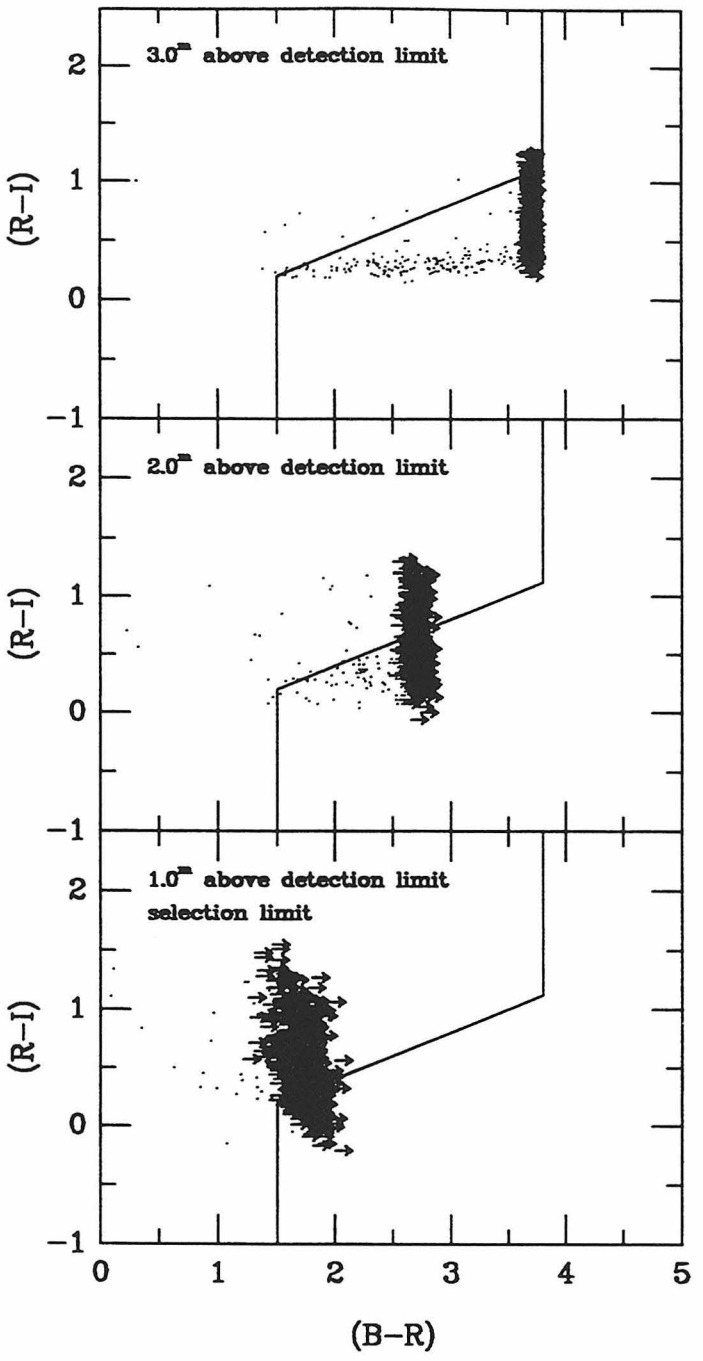

Figure 3.11: Model Quasar *BRI* Colors

Same as Figure 3.9, but for a typical *BRI* data set.

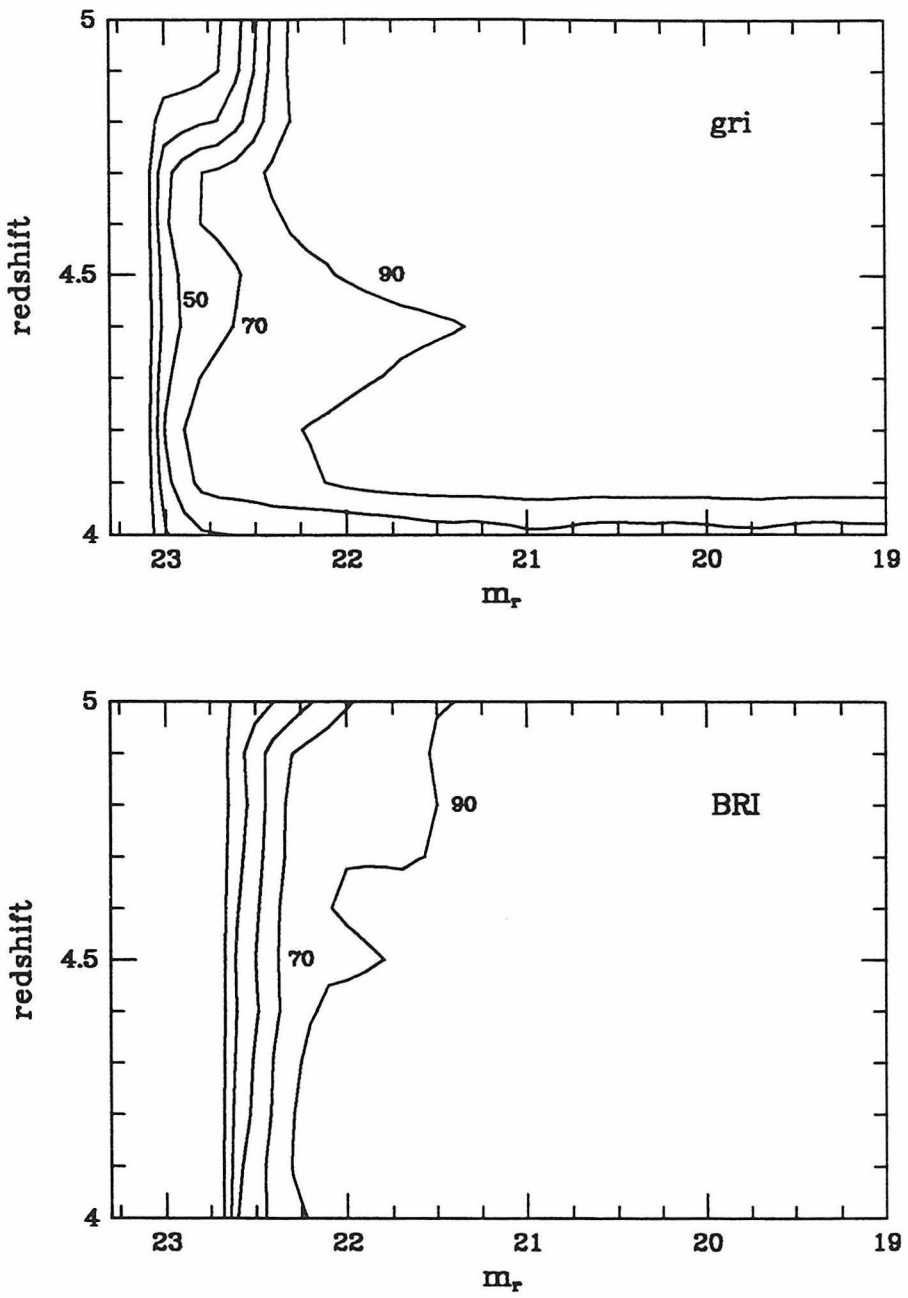

Figure 3.12: Selection Functions

Selection functions for typical *gri* and *BRI* data sets given as a function of redshift and magnitude. Contours are drawn at 10, 30, 50, 70, and 90% intervals. Notice the feature at $z = 4.4$ in the *gri* diagram. This is caused by the dip in the r band filter (Figure 2.1).

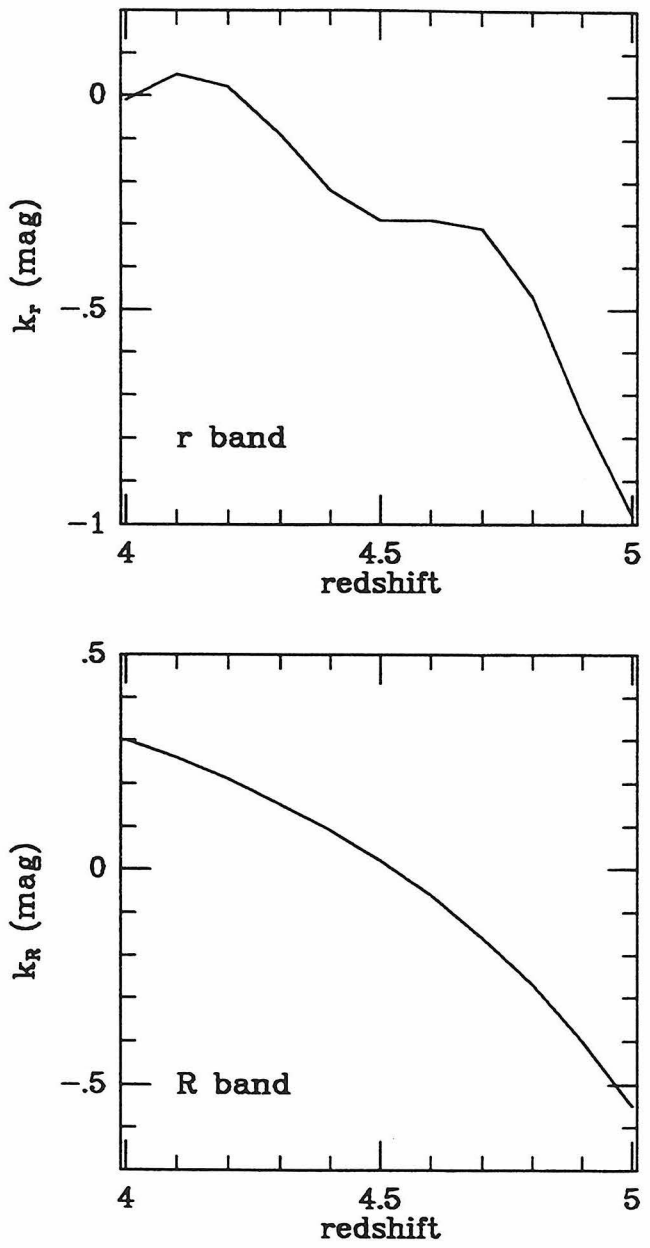

Figure 3.13: k-corrections

The correction from $M_{AB(1450)}$ to r and R magnitudes as a function of redshift as computed from the model quasar spectra.

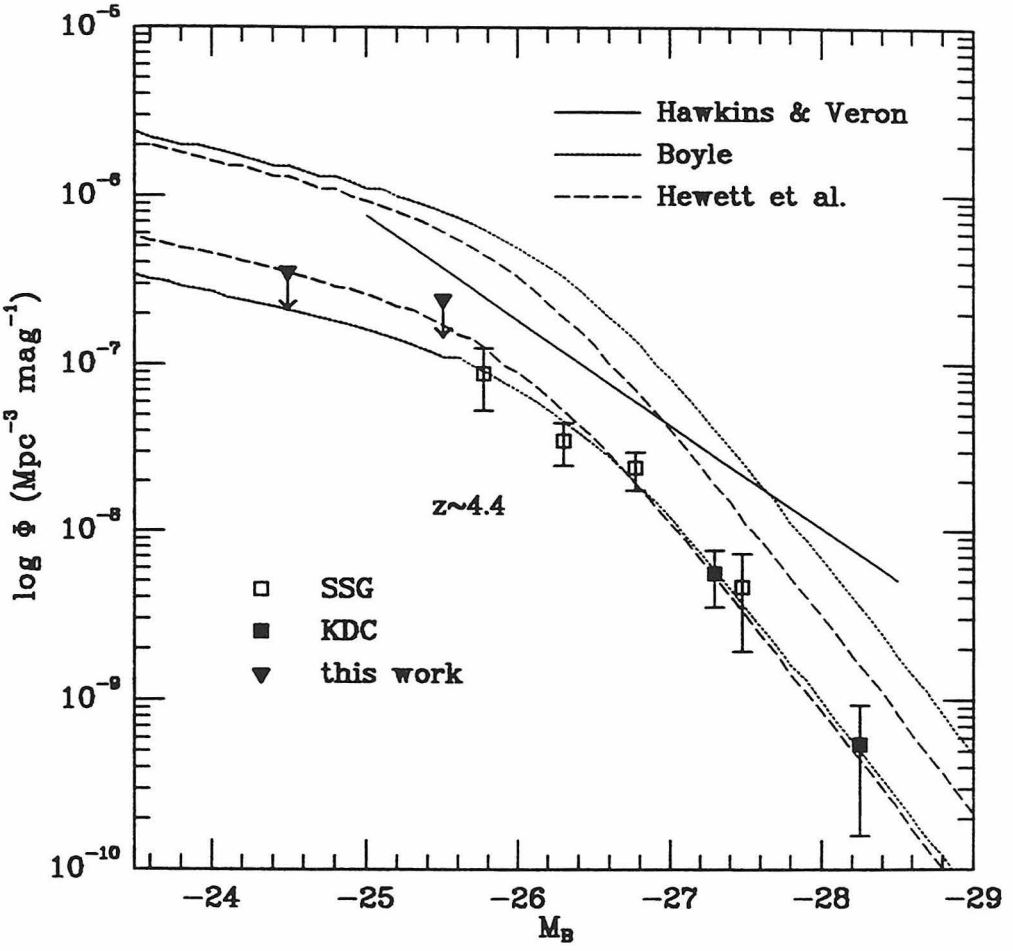

Figure 3.14: Limits on the QLF

Limiting differential space densities from this work and space densities from SSG and KDC at $z \sim 4.4$. Also shown for comparison are the $z \approx 2$ QLF's from Boyle (1988), Hewett et al. (1993), and Hawkins & Veron (1995). The top curve in each case represents the $z = 2$ function, while the bottom curve has been scaled in density to the median redshift of the SSG and KDC points. No attempt was made to scale the Hawkins & Veron function to a higher redshift.

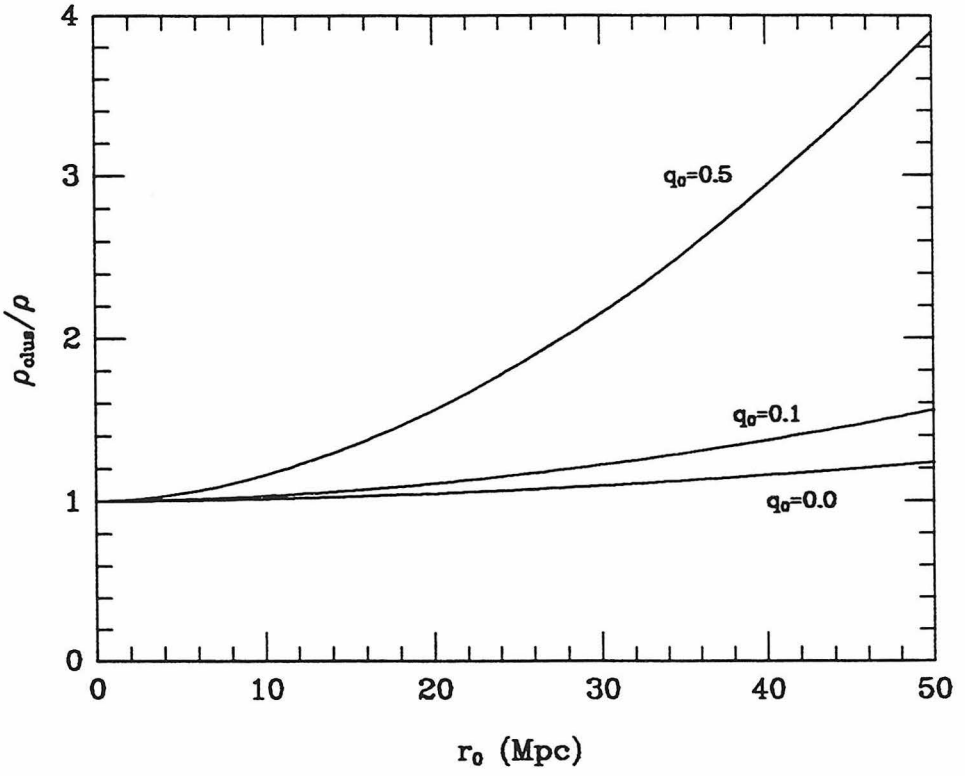

Figure 3.15: Clustering Strengths

Possible quasar overdensities expected in a targeted survey for our typical area and volume coverage as a function of the correlation scale length, r_0, for three different cosmologies ($H_0 = 50$ km s^{-1} Mpc^{-1}). See the text for details.

Chapter 4

The Search for BRI Quasars‡

ABSTRACT

We report the results of a multicolor wide-field CCD survey designed to rediscover several BRI quasars previously found in a photographic survey by Irwin et al. (1991), but not fully documented in the literature. Here we provide spectra, redshifts, finding charts, magnitudes and coordinates for seven such BRI quasars. Follow-up observations were obtained for BRI 2235−03, a borderline BAL object. A moderate resolution absorption line spectrum for the object shows a very dense Lyα forest and two C IV doublets at $z > 3$. Its visible spectrum is redder than those of the other quasars presented, although it is similar in the infrared. J, H, and K magnitudes are presented for this quasar, showing it to be one of the most luminous objects known. New J, H, and K photometry is presented for PC 1247+3406, the most distant quasar known.

‡ Adapted from two papers entitled "Multicolor Detection of High-Redshift Quasars. I. Two Objects at $z > 4$," by J.D. Smith, D. Thompson, and S. Djorgovski, 1994, AJ, 107, 24, and "Multicolor Detection of High-Redshift Quasars. II. Five Objects with $z \gtrsim 4$," by J.D. Smith et al., 1994, AJ, 108, 1147.

4.1 Introduction

In the last few years, several groups have been successful in the search for high-redshift ($z > 4$) quasars, with ~50 such objects having been found to date (Schneider et al. 1994, Warren et al. 1991b, Irwin et al. 1991, Kennefick et al. 1995ab). These surveys have helped to give a better understanding of the quasar luminosity function as well as the origins of quasars themselves. Studies of the absorption line spectra of these objects also give valuable information on the nature and evolution of the intergalactic medium at high redshifts. The existence of $z > 4$ quasars is evidence of the formation of structure in the universe at early epochs (5-10 percent of its present age). Since these objects would have had only ~1 billion years to form and turn on, they must have collapsed from the highest peaks of the primordial density field. This places strong constraints on galaxy formation in the early universe (Rees 1992, Turner 1991).

When we began this project, about 40 $z > 4$ quasars were known, with only 17 having published coordinates. Irwin et al. (1991) have discovered over 20 such objects in a photographic multicolor survey using APM measurements of UK Schmidt Telescope plates, but have reported the coordinates for only two of these objects (McMahon et al. 1994; Williger et al. 1994). Rough coordinates for some of the BRI quasars are given by Irwin & McMahon (1990). We are conducting a multicolor survey for quasars and star forming galaxies near known $z \gtrsim 4$ quasars, looking for protoclusters near these early quasars (Smith et al. 1993, Djorgovski et al. 1991). We are interested in using the BRI quasars in our protocluster search, and so began a survey to "rediscover" these objects. Here we describe our detection methods and present data on seven quasars: BRI 0103+00, BRI 0151−00, BRI 0241−01, BRI 1013+00, BRI 1050−00, BRI 1500+08, and BRI 2235−03. One of these objects, BRI 2235−03, has a very red continuum, and we present infrared magnitudes and a moderate resolution absorption line spectrum of it as well.

4.2 Observations

4.2.1 The Technique

The BRI quasars have coordinates published truncated to the nearest degree in declination and to the nearest minute in right ascension (Irwin & McMahon 1990). The quasars are mainly equitorial, and so their possible coordinates form a box 60 arcmin in declination and at most 15 arcmin in right ascension. Our initial imaging data were taken at the CTIO Schmidt telescope using a 1024^2 Tektronix CCD giving a 31.2 arcmin field of view with 1.83 arcsec/pixel and at the Palomar 60 inch telescope using reimaging optics and a 1024^2 Tektronix CCD giving an 18.4 arcmin field of view with 1.08 arcsec/pixel. Three pointings in a strip of constant right ascension were necessary in order to cover the desired range with some overlap using the CTIO Schmidt while four pointings were necessary with the Palomar 60 inch.

A simple method to discover high-redshift quasars is to use the Johnson *BRI* or Gunn-Thuan *gri* bands, and look for objects where the Lyα line is in the red band. The line, and the continuum drop across it would leave a distinct color-color signature (see Figure 1.1). The initial imaging was obtained in the *BRI* or *BRi* bands. Photometry was performed on all objects in the fields using *DAOPHOT* (Stetson 1987) and calibrated using standard stars (Landolt 1992; Kent 1985). All objects with appropriate colors were visually examined and a candidate list was formed by ranking candidates according to their positions in color-color space and image morphology (stellar vs. extended). Follow-up spectroscopy of our highest ranked candidates was then performed.

4.2.2 CCD Imaging

We obtained at least 1000s, 600s, and 600s in Johnson B and R and Gunn i respectively at each pointing around the quasars BRI 1013+00 and BRI 1050−00 on UT 1993 March 23 to 25 at the Palomar 60 inch telescope. Longer exposure times were used in bad weather. Two pointings of the BRI 1050−00 data were photometric and allowed us to calibrate this data set using standard stars and extrapolating the calibrations to the other pointings using overlapping regions. All of the BRI 1013+00 data were nonphotometric and were only roughly calibrated. CCD imaging totaling 3600s in B, 900s in R, and 900s in i was obtained under photometric conditions on the four fields around BRI 1500+08 at the Palomar 60 inch telescope on the nights UT 1993 May 18-20. Our initial imaging from the CTIO Schmidt telescope consisted of two 300s exposures in each of the BRI bands at the three pointings around BRI 0111−28 under photometric conditions and around BRI 2235−03 under nonphotometric conditions on UT 1993 June 26 and 29. A total of 1800s in B, 400s in R, and 400s in i was obtained under photometric conditions on the four fields around BRI 0103+00, BRI 0151−00, and BRI 0241−01 at the Palomar 60 inch telescope on the nights UT 1993 October 19 and 20. All of the data are complete to at least 20^m in R with the exception of the BRI 2235−03 data which are complete to 19^m.

The color-color diagram of the objects in the fields around several of the rediscovered BRI quasars as well as data around BRI 0111−28 is shown in Figure 4.1. The $(B-R)$ vs. $(R-i)$ data taken at the Palomar 60 inch telescope were shifted along the $(R-I)$ axes of the BRI 0111−28 data so that the stellar sequences coincide. The nonphotometric data of BRI 2235−03 were shifted so that its stellar sequence coincides with the BRI 0111−28 data as well.

4.2.3 Spectroscopy

Objects were chosen as candidates from appropriate areas of the color-color space. Images of the candidates were inspected and ranked according to image morphology and color. Two 600 second spectra of BRI 1050−00 were obtained in hazy weather and at high airmass on UT 1993 May 26 at the Hale 200-inch telescope, using the 4Shooter spectrograph. A total of 5400 seconds on BRI 1013+00 was obtained on the nights of UT 1993 May 27 and June 10 with the same instrument through some clouds. Spectra were reduced using standard techniques. Wavelength calibration, using helium and neon arcs, is good to an RMS of ∼0.5Å. Flux calibration, using standard stars from Oke & Gunn (1983) and Stone (1974), is estimated to be accurate to $\pm 0^m.3$ due to the hazy weather conditions.

Follow-up spectroscopy was also performed at the ESO NTT using the EMMI spectrograph. Low resolution spectra of BRI 1500+08 (2700 seconds) and BRI 2235−03 (two 3600 second exposures) obtained on the nights of UT 1993 August 19 and 20 were flux calibrated using a standard star from Hamuy et al. (1992), Baldwin & Stone (1984) and Stone & Baldwin (1983). Wavelength calibration, using a polynomial fit to helium and argon arcs, has residuals of ∼0.3Å. We also obtained spectra on two candidates from the BRI 0111−28 field at this time which were identified as red stars. Low resolution spectroscopy was obtained on UT 1993 December 8-10 at the ESO NTT on the objects BRI 0103+00 (1500 seconds), BRI 0151−00 (1200 seconds), and BRI 0241−01 (1500 seconds). The spectra were flux calibrated using a standard star from Baldwin & Stone (1984). Wavelength calibration, using a polynomial fit to helium and argon arcs, has residuals of ∼0.3Å.

4.3 Results

4.3.1 The BRI Quasars

Low resolution spectra of the seven BRI quasars are shown in Figure 4.2 with emission line redshifts given in Table 4.1. Because all of the spectra were obtained in marginally nonphotometric weather, the flux zero points have been adjusted to be consistent with the aperture photometry.

As a measurement of the discontinuity across the Lyα line, we have computed the continuum depression, D_A, parameterized by Oke & Korycanski (1982, see Eq. 2.1) for each spectrum as outlined by Schneider et al. (1989). D_A is measured between rest wavelengths of 1050 and 1170Å. Where the spectrum didn't extend far enough to the blue, D_A was computed between our blue limit and 1170Å. A power law was assumed to estimate the continuum flux. The value of D_A for each spectrum is listed in Table 4.2.

BRI 0103+00: We derive an emission-line redshift of 4.433±0.005 based on the Lyα, O I + Si II, and C IV lines. The Si IV + O IV lines are obscured by atmospheric absorption. We detect the presence of a C IV absorption doublet at z=3.32 (6690 and 6702Å).

BRI 0151−00: We derive an emission-line redshift of 4.196±0.005 based on the C IV and Si IV + O IV lines. We detect the presence of Lyα absorption at 6282Å, N V at and 6426Å, and C IV at 7999 and 8013Å (denoted by vertical bars in Figure 3b) which we identify as an absorption system at z=4.17.

BRI 0241−01: We derive an emission-line redshift of 4.042± 0.005 based on the C IV and Si IV + O IV lines. We detect Lyα absorption at 6036Å, Si IV + O IV at 6962Å, and C IV at 7687Å, as denoted by the vertical lines in Figure 8, which we identify as an absorption system at z=3.97. We also detect the presence of a C IV absorption doublet at z=3.12 (6384 and 6394Å).

BRI 1013+00: We derive an emission-line redshift of 4.381±0.010 for this quasar, with more weight given to the weak, broad N V and C IV lines in determining the redshift because of the severe blue-side absorption in the Lyα line typical of high-redshift QSOs. We see some evidence for a damped Lyα absorption system roughly centered at λ5909 (z =3.86), and possibly a second at λ5748 (z =3.73), though our low-resolution data, and the proximity of the atmospheric sodium emission line to the higher redshift system, make these identifications uncertain. The absorption line at λ6300 is strongly affected by the λ6300 [O I] atmospheric emission line and does not appear to be a damped system.

BRI 1050−00: We derive an emission-line redshift of 4.291±0.002, based on the emission lines of Lyβ, O VI, Lyα, and C IV, with the highest weight given to the C IV line. Two Lyα absorption lines, at λ6350.5 and λ6372.8 (z = 4.224 and 4.242, respectively), can be seen immediately blueward of the Lyα emission line, though our spectrum has too low a signal-to-noise to allow us to say anything conclusive on the rest of the Lyα forest region. A group of faint, presumably foreground, galaxies is seen within a few arcsecs of the quasar (figure 4). It is possible, although highly speculative, that this bright quasar has been gravitationally magnified.

BRI 1500+08: The spectrum has been Gaussian smoothed with σ = 2 pixels. We derive an emission-line redshift of 3.96±0.02 based on the Lyα, C IV and Si IV + O IV lines. The C IV and Si IV + O IV lines are heavily affected by atmospheric absorption, making the redshift less certain. We detect an absorption system at 8140 and 8159Å which we identify as Mg II absorption at z=1.91. This identification is made more certain by the presence of Fe II absorption at 7565, 6935, and 6822Å (rest wavelengths of 2600, 2383, and 2344Å respectively).

BRI 2235−03: We derive an emission-line redshift of 4.24±0.02 based on the Lyα, Si IV + O IV, and C IV lines. This object shows features typical of BAL quasars. Notice the broad absorption feature at ∼6700Å, probably due to Si IV + O IV absorption and the absorption at ∼7450Å and ∼7800Å probably due to

C IV. The value of D_A given in Table 1 for this object is very uncertain because the continuum is difficult to define.

So far we have failed to detect BRI 0111−28. It could have been overlooked due to some chip defect. More likely, it is lower down on our candidate list and we have been unable to obtain a spectrum to date.

R band magnitudes computed using aperture photometry from the initial Palomar 60 inch data give R = 18.70±0.09 for BRI 0103+00, R = 18.65±0.09 for BRI 0151−00, R = 18.29±0.09 for BRI 0241−01, R = 18.79±0.05 for BRI 1050−00, and R = 18.84±0.07 for BRI 1500+08. All data in the BRI 1013+00 field were nonphotometric. We have adopted R = 19.1±0.2 for this object. Follow-up imaging of four BRI quasars was performed at the Palomar 60 inch telescope using direct imaging in the Gunn-Thuan r band under photometric conditions on UT 1993 September 12-13 and December 10. Aperture photometry on these objects gives r = 18.94±0.03 for BRI 0103+00, r = 18.76 ± 0.03 for BRI 0151−00, r = 19.04 ±0.02 for BRI 1500+ 08, and r = 18.72±0.05 for BRI 2235−03. After applying the r band photometry for BRI 2235−03 to adjust the flux zero points of its spectrum, we find R=18.6±0.2. R band magnitudes for the seven quasars are listed in Table 4.2.

Astrometry provided by the GASP (Guide Stars Selection System Astrometric Support Program developed by STScI) program was used to determine accurate coordinates for at least six bright stars in each of our fields, with the exception of BRI 0241-01. We then performed a least squares fit to transform from the rectangular coordinate system of our CCD data to equatorial coordinates. Coordinates for the objects are listed in Table 4.2. Positions given are accurate to better than 0.1^s in right ascension and 1 arcsec in declination. The coordinates for BRI 0241−01 were found by identifying this object on a DPOSS scan (Reid

& Djorgovski 1993) and using astrometric solutions provided by STScI. These coordinates are supposed to be good to 0.5″ r.m.s. accuracy (Lasker et al., *priv. comm.*).

4.3.2 Follow-up Observations of BRI 2235−03

Moderate resolution spectroscopy was obtained for BRI 2235−03 on the night of UT 1993 August 21 in nonphotometric weather at the ESO NTT with the EMMI spectrograph. In the blue (4300 - 6800Å) a grism with a dispersion of 1.8 Å/pixel was used while in the red (6200 - 8500Å) a different grism gave 1.6 Å/pixel. Wavelength calibration, using a polynomial fit to helium and argon arcs, has residuals of ∼0.2Å (blue) and ∼0.8Å (red). The two spectra were combined after extraction by coaveraging overlapping regions. Numerous Lyα forest lines are detected in this spectrum (Figure 4.4, Table 4.3). Two absorption systems are also readily detected by the presence of C IV doublets at ∼6511Å ($z = 3.20$) and 6588Å ($z = 3.25$) (denoted by arrows in figure 4.4) with corresponding Lyα absorption at 5109Å and 5170Å.

Deep R and I band imaging was obtained on UT 1993 August 21 with EMMI with a scale of 0.347 arcsec/pixel, revealing a faint ($\sim 23^m$) galaxy 1.8 arcsec south of the quasar (figure 4.5). In the low resolution spectra of BRI 2235−03, the slit was oriented north-south, catching this galaxy as well. The spectrum of this object shows no obvious emission, but it has detectable continuum emission blueward of where the Ly limit (912Å) would be if the object were at the redshift of BRI 2235−03. Therefore, it is unlikely that this object is at the same redshift as the quasar and it must be a foreground galaxy. It is possible that this galaxy is responsible for one of the absorption systems seen in the spectra of the quasar.

The spectrum of BRI 2235−03 has a continuum that rises sharply to the red (Figure 4.2g). This prompted us to obtain infrared imaging of this field.

This imaging was performed at the Palomar 200 inch telescope on the night of UT 1993 November 24 giving $J = 16.73 \pm 0.05$, $H = 16.00 \pm 0.07$, and $K = 15.33 \pm 0.05$. These magnitudes as well as R and I magnitudes are plotted in Figure 4.6 in terms of the specific power, computed as $P_{\nu_0} = 4\pi {D_L}^2 f_{\nu_0}$, and the specific luminosity, $\nu_0 P_{\nu_0}$, vs. ν_0 (emitted frequency). D_L is the luminosity distance. We have assumed $H_0 = 75$km/sec/Mpc and $q_0 = 0.1$.

As a comparison, PC 1247+3406, the most distant quasar known, and Q 0051−279 are also plotted in Figure 4.6. Infrared magnitudes of PC 1247+3406 obtained on UT 1992 March 18 at the Palomar 200 inch telescope were found to be $J = 18.5 \pm 0.1$, $H = 17.9 \pm 0.1$, and $K = 17.2 \pm 0.1$. Optical data for PC 1247+3406 can be found in Schneider et al. (1991b). For Q 0051−279, infrared data were taken from Carico et al. (1988) and optical data from Warren et al. (1987b). The slope of the infrared region of the BRI 2235−03 data is comparable to that of the other two quasars presented. However, the BRI 2235−03 spectrum rises sharply from the optical to the infrared, making it a very red object.

At the redshift of BRI 2235−03, the K band is roughly equivalent to the rest frame B band. Therefore, L_{bol} can be computed as $L_{bol} = 16\nu_0 P_{\nu_0}$ (Chokshi & Turner 1992). For BRI 2235−03, we find $L_{bol} = 1.0 \times 10^{49}$ergs/sec $= 2.6 \times 10^{15} L_\odot$, assuming a cosmology of $H_0 = 75$km/sec/Mpc and $q_0 = 0.1$. This makes it one of the most luminous objects known, comparable to IRAS F10214+4724 (Rowan-Robinson et al. 1993), HS 1946+7658 (Hagen et al. 1992), Q 0000−26 (Webb et al. 1988).

4.4 Concluding Remarks

We have verified the utility of the wide-field, multicolor CCD imaging method for searches for $z > 4$ quasars. Multicolor CCD imaging using relatively small telescopes with reimaging optics or Schmidt telescopes is a competitive technique for high-redshift quasar searches, filling the niche between photographic (Schmidt plate) surveys which cover large areas but do not go very deep, and surveys using large telescopes which go to faint levels but which cover relatively small areas. In the course of this survey, we have identified seven BRI quasars. One of them, BRI 2235−03, is one of the most luminous objects now known, with $L_{bol} = 1.0 \times 10^{49}$ergs/sec $= 2.6 \times 10^{15} L_{\odot}$.

TABLE 4.1: Emission-line Redshifts

QSO	Line	λ_{obs} (Å)	z
BRI 0103+00	Lyα	6605	4.433±0.005
	O I + Si II	7097	4.434±0.005
	C IV	8415	4.432±0.005
	Adopted redshift =		4.433±0.005
BRI 0151−00	Lyα	6323	4.201±0.005
	O I + Si II	6779	4.191±0.005
	Si IV + O IV	7286	4.197±0.005
	C IV	8049	4.196±0.005
	C III]	9906	4.189±0.005
	Adopted redshift =		4.196±0.005
BRI 0241−01	Lyα	6174	4.079±0.005
	Si IV + O IV	7070	4.042±0.005
	C IV	7810	4.042±0.005
	C III]	9673	4.067±0.010
	Adopted redshift =		4.042±0.005
BRI 1013−00	Lyα	6571	4.405±0.010
	N V	6660	4.371±0.010
	C IV	8355	4.392±0.010
	Adopted redshift =		4.381±0.010
BRI 1050+00	Lyβ	5434.5	4.298±0.002
	O VI	5487.2	4.288±0.002
	Lyα	6436.N	4.294±0.002
	C IV	8197.N	4.290±0.002
	Adopted redshift =		4.291±0.002
BRI 1500+08	Lyα	6023	3.95±0.02
	Si IV + O IV	6965	3.97±0.02
	C IV	7676	3.96±0.02
	Adopted redshift =		3.96±0.02
BRI 2235−03	Ly Limit	4770	4.23±0.02
	Lyα	6370	4.24±0.02
	Si IV + O IV	7325	4.23±0.02
	C IV	8093	4.22±0.02
	Adopted redshift =		4.23±0.02

TABLE 4.2: Coordinates, redshifts, R magnitudes, and continuum depressions, D_A, for the quasars

QSO	α (B1950)	δ (B1950)	z	R	D_A
BRI 0103+00	01 03 45.3	+00 32 21	4.433±0.005	18.70±0.09	0.62
BRI 0151−00	01 51 05.9	−00 25 44	4.196±0.005	18.65±0.09	0.68
BRI 0241−01	02 41 29.3	−01 46 42	4.042±0.005	18.29±0.09	0.52
BRI 1013+00	10 13 15.0	+00 35 18	4.381±0.010	19.1±0.2	0.67
BRI 1050−00	10 50 46.7	−00 00 02	4.291±0.002	18.79±0.05	0.65
BRI 1500+08	15 00 18.2	+08 24 49	3.96±0.02	18.84±0.07	0.62
BRI 2235−03	22 35 47.5	−03 01 30	4.23±0.02	18.6±0.2	0.78

TABLE 4.3:
Detected Lyα forest lines for BRI 2235−03 (Å)

5109.4	5133.3	5170.3	5206.7
5230.0	5251.2	5269.7	5345.0
5373.5	5420.8	5432.8	5451.6
5481.5	5510.1	5555.2	5577.4
5656.1	5676.0	5695.3	5828.9
5871.6	5900.0	5940.8	6017.8
6032.1	6087.0	6160.2	6183.8
6190.8	6212.0	6227.5	6245.3
6270.6	6287.7	6308.8	6343.7
6361.5	6381.9		

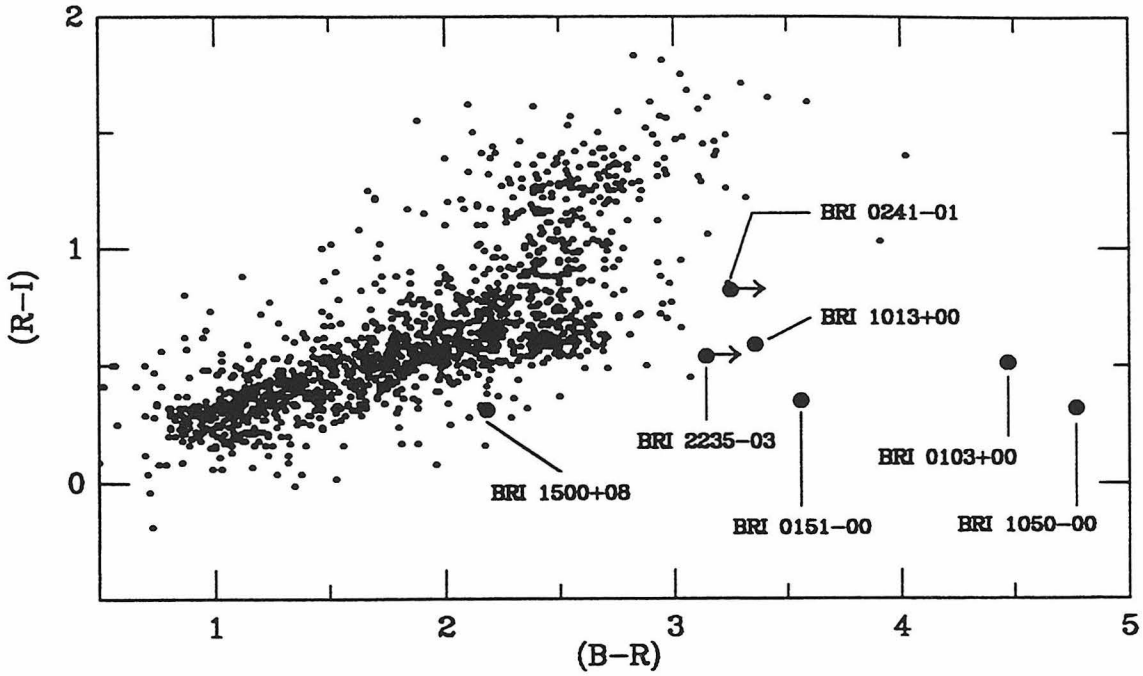

Figure 4.1: BRI Color-Color Diagram

A representative *BRI* color-color diagram containing objects in the fields around four of the BRI quasars along with the seven rediscovered BRI quasars (large, filled circles). Arrows designate that the $(B-R)$ color is a lower limit.

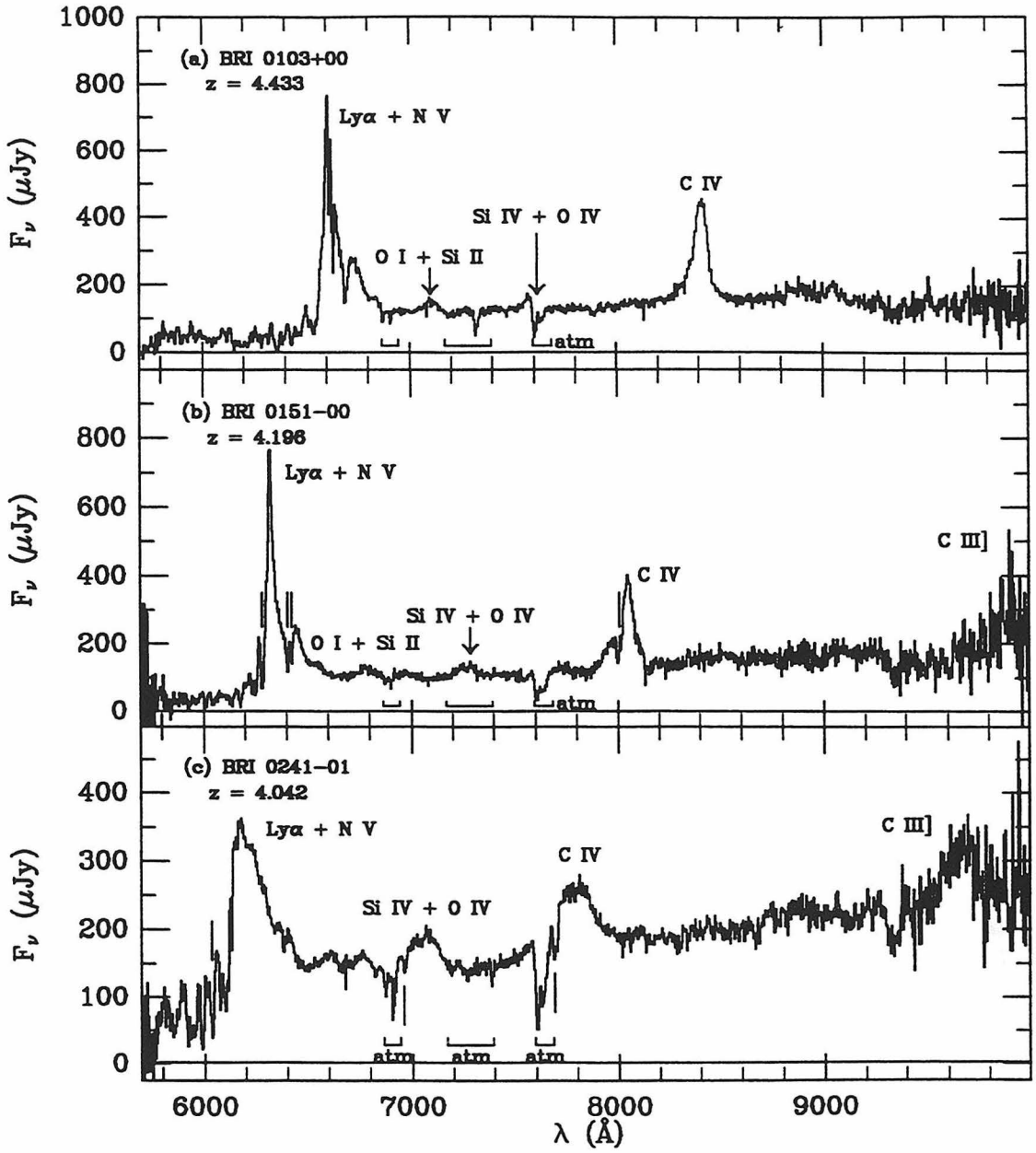
(a) BRI 0103+00
z = 4.433
Lyα + N V
C IV
Si IV + O IV
O I + Si II
atm
(b) BRI 0151−00
z = 4.196
Lyα + N V
C III]
C IV
Si IV + O IV
O I + Si II
atm
(c) BRI 0241−01
z = 4.042
Lyα + N V
C III]
C IV
Si IV + O IV
atm
atm
atm
F_ν (μJy)
λ (Å)
1000
800
600
400
200
0
300
100
6000
7000
8000
9000

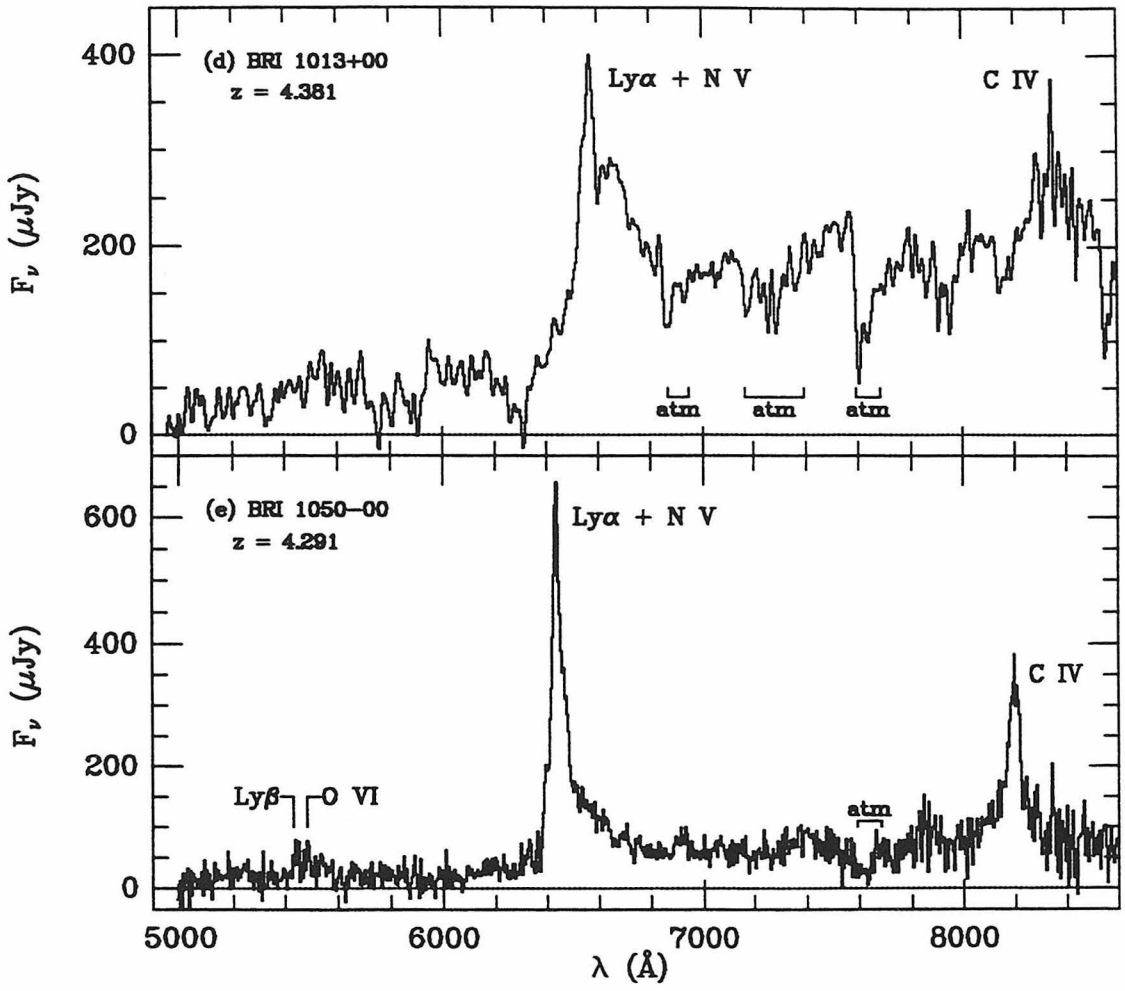
(d) BRI 1013+00
z = 4.381
Lyα + N V
C IV
atm
atm
atm
(e) BRI 1050−00
z = 4.291
Lyα + N V
C IV
Lyβ
O VI
atm
400
200
0
600
400
200
0
5000
6000
7000
8000
λ (Å)
F_ν (μJy)
F_ν (μJy)

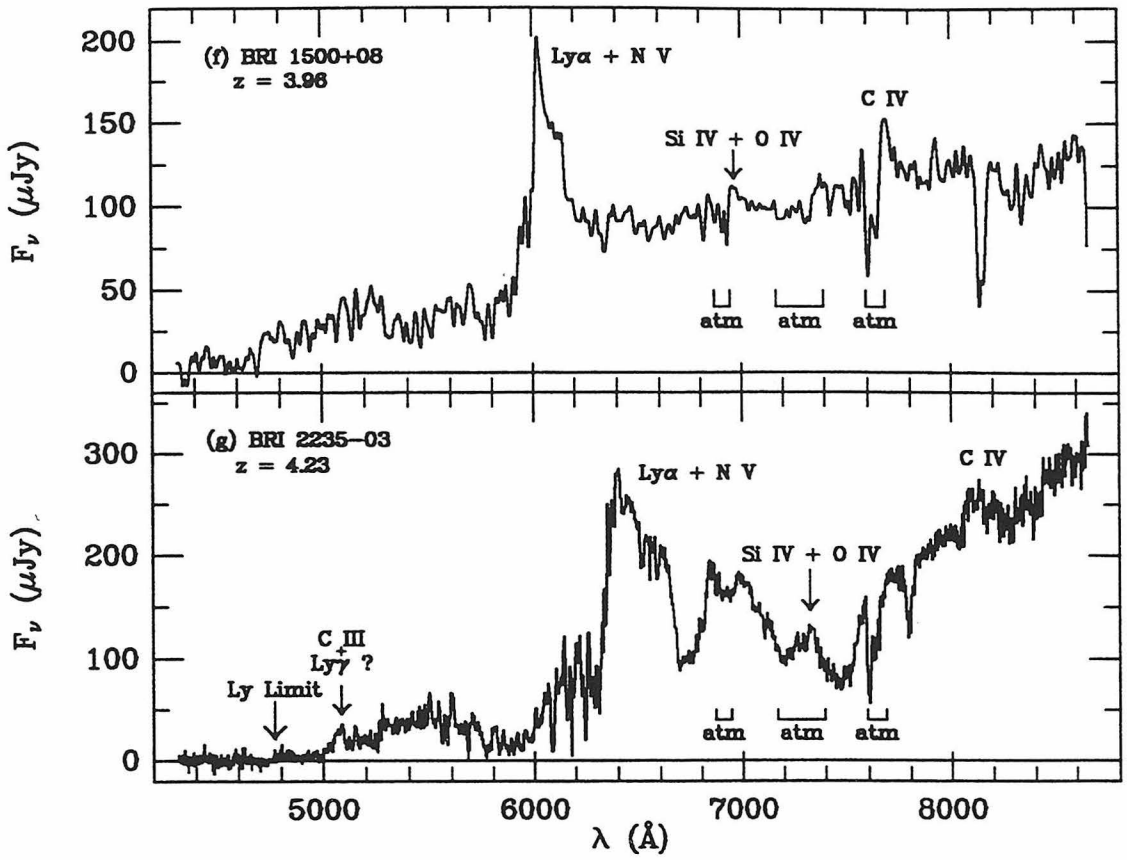

Figure 4.2: Spectra of BRI Quasars

Low resolution spectra of the rediscovered BRI quasars. (a) A 1500s EMMI spectrum of BRI 0103+00. (b) A 1200s EMMI spectrum of BRI 0150−00. (c) A 1800s EMMI spectrum of BRI 0241−01. (d) A 5400s 4Shooter spectrum of BRI 1013+00, Gaussian smoothed with $\sigma = 1$ pixel. (e) A 1200s 4Shooter spectrum of BRI 1050−00. (f) A 2700s EMMI spectrum of BRI 1500+08. The spectrum has been Gaussian smoothed with $\sigma = 2$ pixels. (g) A 7200s EMMI spectrum of BRI 2235−03. Emission lines are labeled.

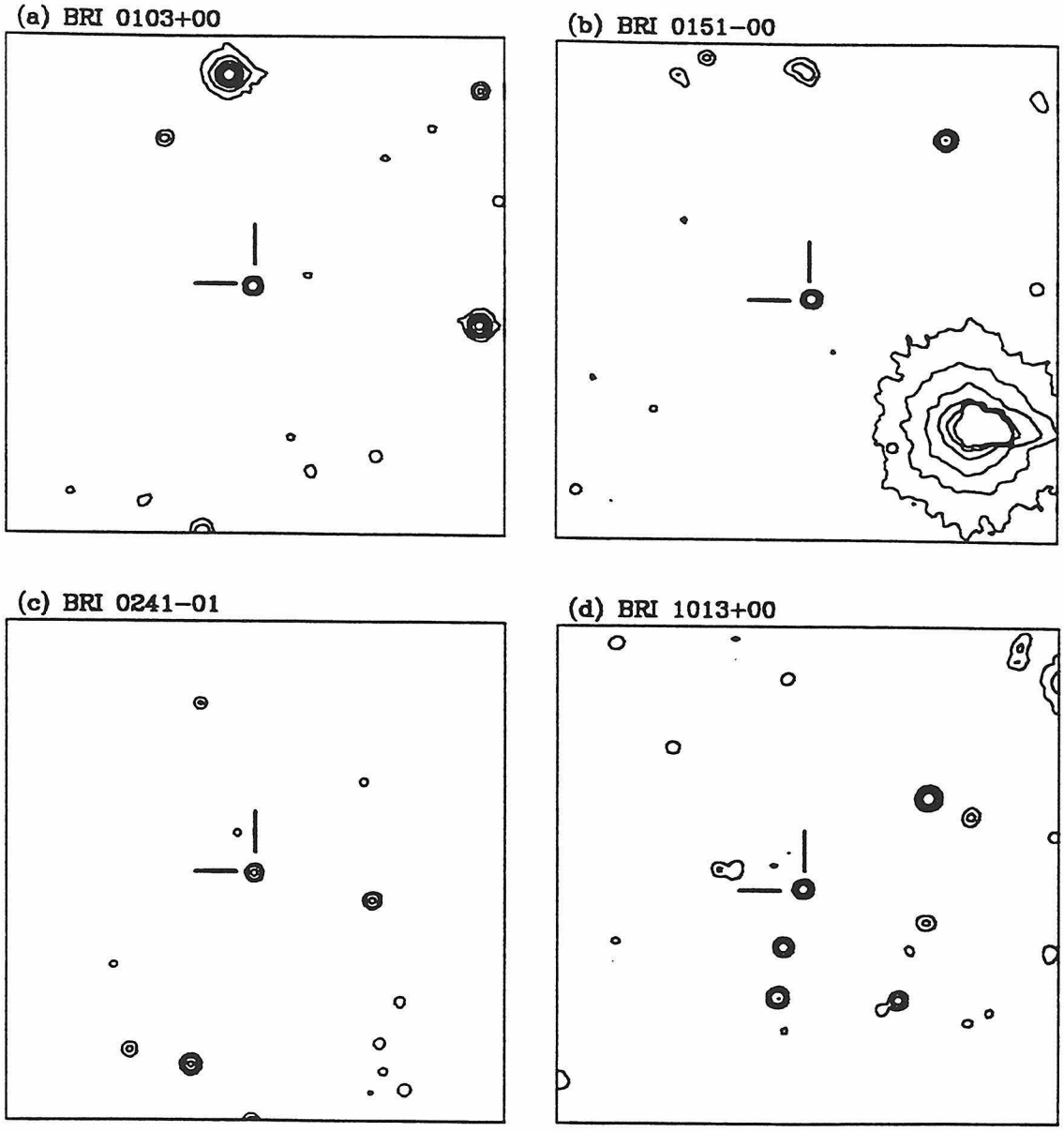
(a) BRI 0103+00
(b) BRI 0151−00
(c) BRI 0241−01
(d) BRI 1013+00

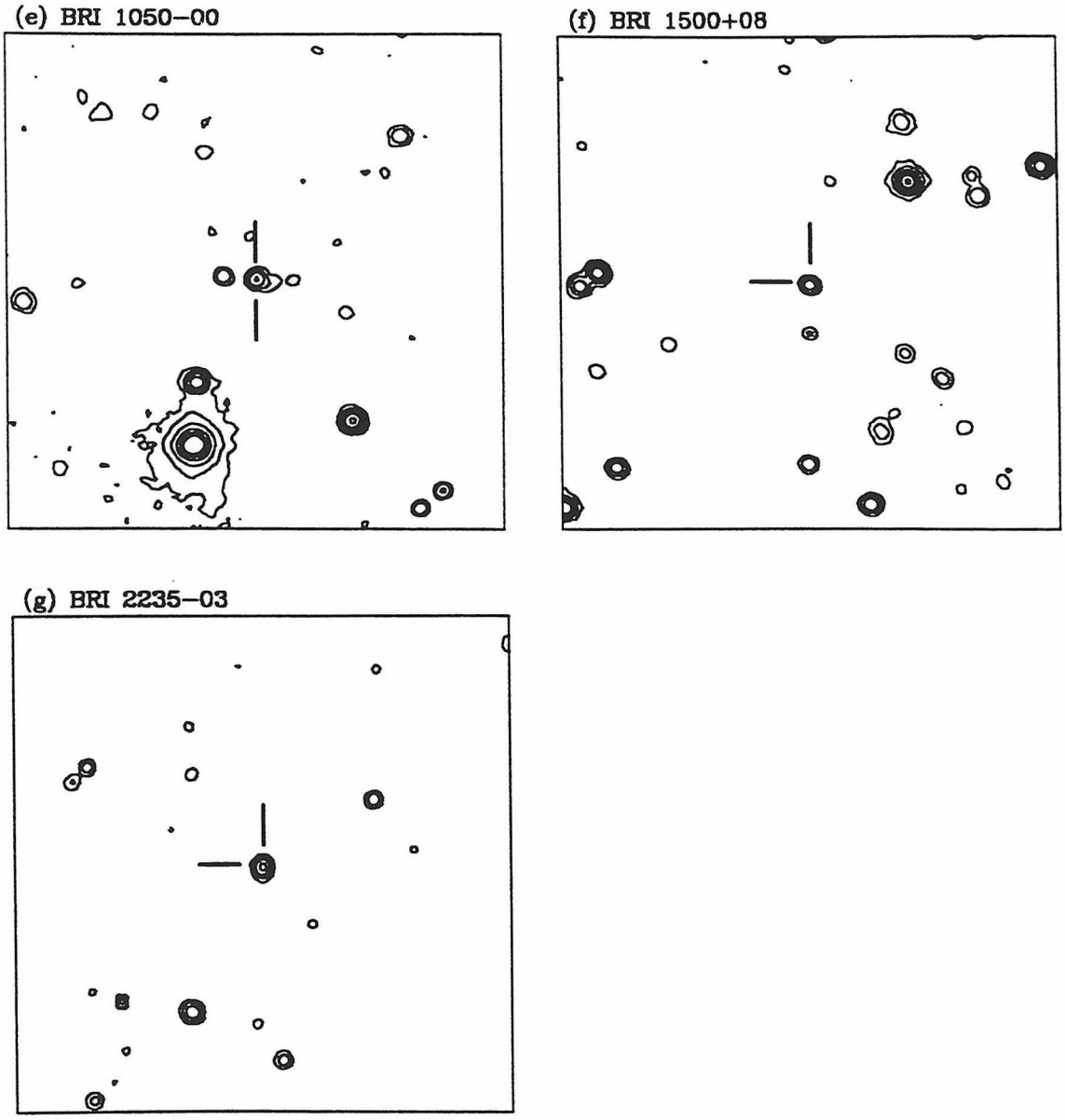

Figure 4.3: Finding Charts for the BRI Quasars

Contour plots of the fields around the seven rediscovered BRI quasars. All images are 2 arcmin square with north up and east to the left.

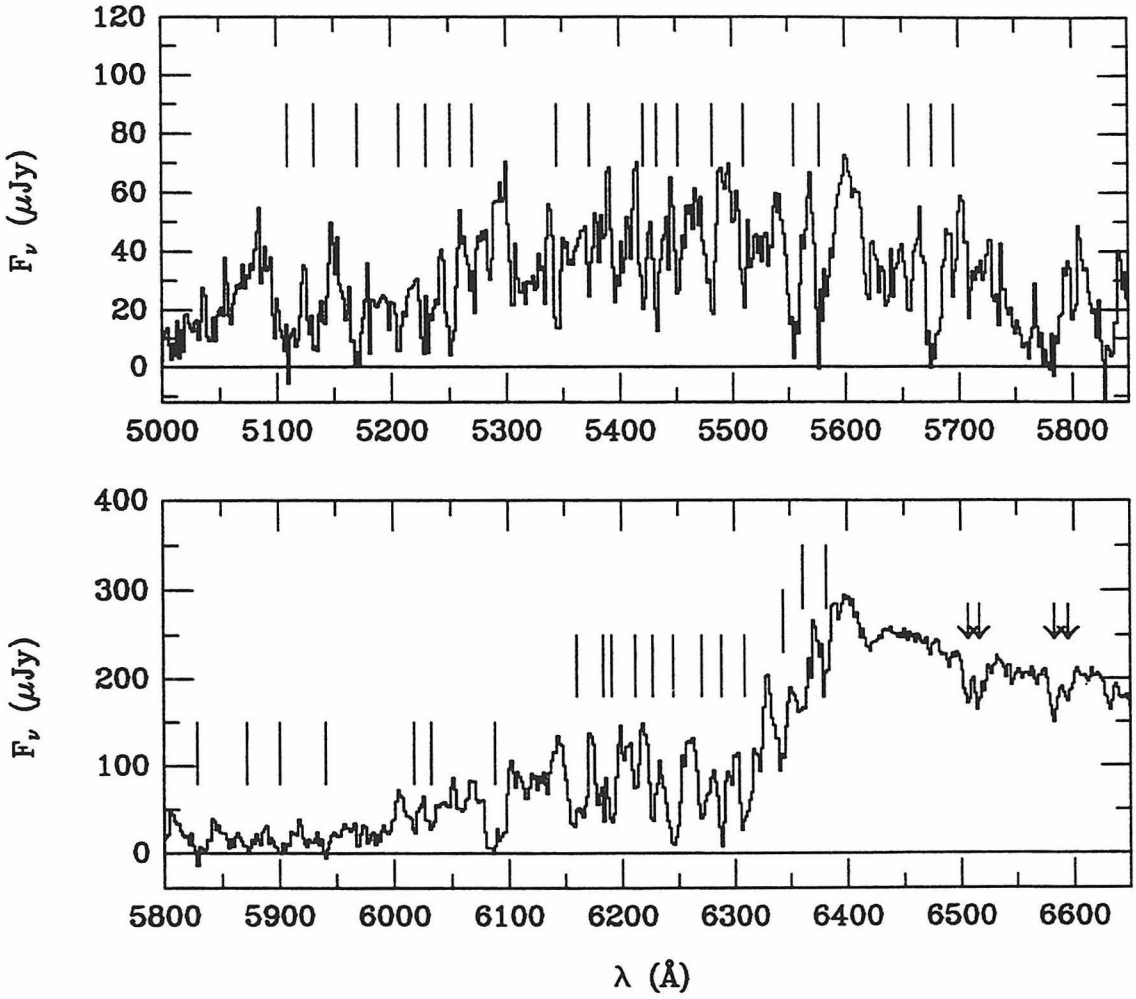

Figure 4.4: Moderate Resolution Spectrum of BRI 2235−03

Moderate resolution spectrum of the quasar BRI 2235−03 taken with the EMMI spectrograph at the ESO NTT. The vertical lines mark detected Lyα absorption features. The arrows indicate two sets of C IV doublets.

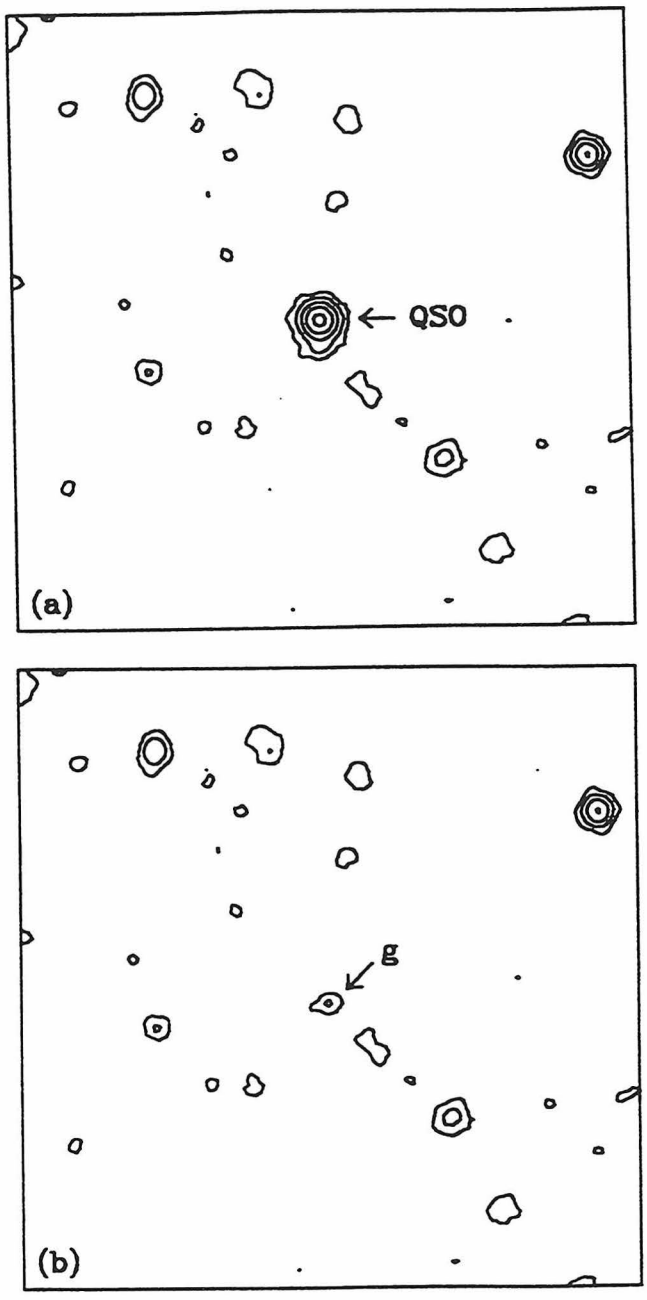

Figure 4.5: The Galaxy South of BRI 2235−03

(a) A 1080s combined R and I image of BRI 2235−03 taken at the ESO NTT on UT 1993 August 20 and 21. (b) The same image with the quasar subtracted using a model PSF. Note the faint galaxy (designated "g") directly south of the quasar. The images are 1 arcmin square with north up and east to the left.

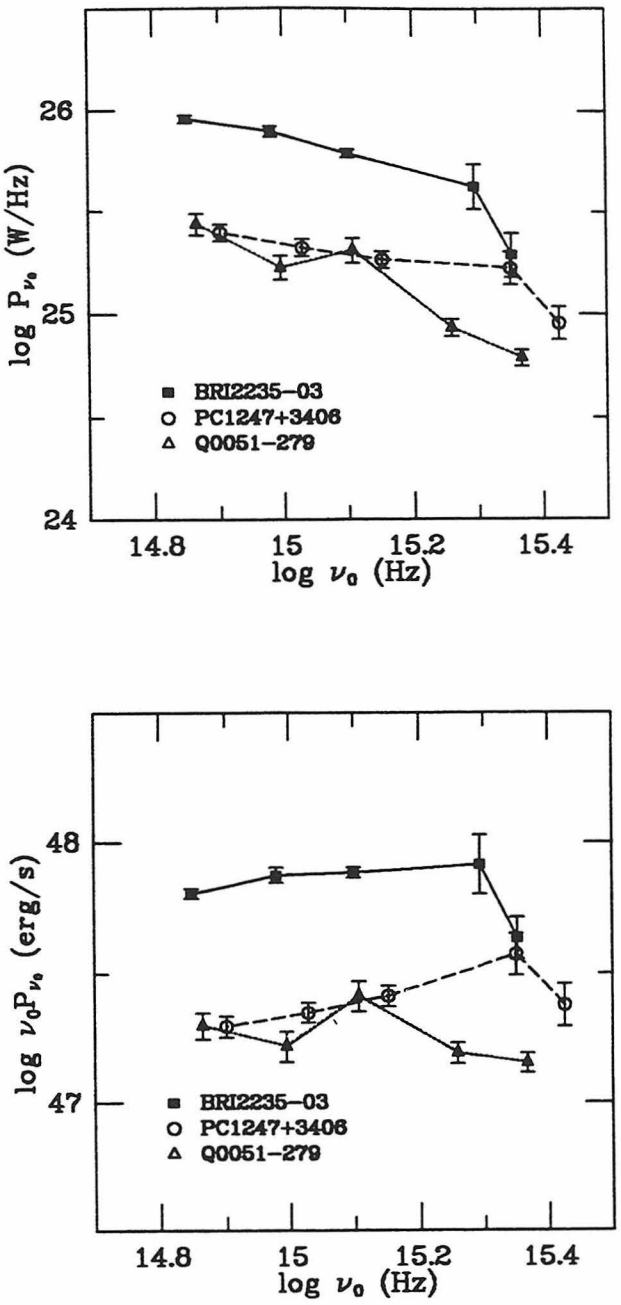

Figure 4.6: Power Spectra

Spectra of the three quasars BRI 2235−03 (filled squares), PC 1247+3406 (open circles), and Q 0051−279 (open triangles) plotted in terms of the specific power, P_{ν_0}, and the specific luminosity, $\nu_0 P_{\nu_0}$, vs. the emitted frequency, ν_0.

Chapter 5

Conclusions and Prospects for the Future

We have conducted two multicolor surveys for quasars at $4 \lesssim z \lesssim 5$, one at bright magnitudes ($r < 19.6^m$, corresponding to $M_B < -27^m$ at these redshifts), and one at faint magnitudes ($r \sim 23^m$, corresponding to $-26^m < M_B < -24^m$ at these redshifts). These two surveys compliment the CCD grism survey of Schmidt et al. (1995, SSG), which is sensitive to quasars with $-27.5^m < M_B < -26^m$ at $z > 4$. When taken together, these three surveys show a consistent picture of a decrease in quasar space densities from $z = 2$ to $z = 4$.

The Warren et al. (1994, WHO) and SSG groups have both computed the QLF from $z \sim 2.5$ to $z \sim 4.5$. Both groups find evidence for a decrease in quasar space densities beyond $z \sim 3$. Our findings provide further evidence in support of this picture. We see a decrease in the number of quasars from $z = 2$ to $z = 4$ at both faint and bright magnitudes, and find no evidence for differential evolution (luminosity dependent density evolution) in the population. This is in direct contrast with Irwin et al. (1991, IMH), who argue that no evolution occurs between $z = 2$ and $z = 4$.

The DPOSS and IMH surveys employ an almost identical technique, and are sensitive to the same redshift and magnitude ranges. The two surveys are in fact recovering roughly the same number of quasars per effective area covered. This would suggest that the two surveys are finding similar space densities of quasars

at $z \gtrsim 4$, but are interpreting the results in a different way. We surmise that the probable cause of this discrepancy is due to the adaptation of different methods when computing M_B for the detected quasars. For example, BRI 0103+0032 is common to both surveys. We find $M_B = -27.4^m$ for this quasar. IMH, on the other hand, compute $M_B = -28.4^m$ (M. Irwin, private communication), a difference of 1^m. This would certainly explain the apparent discrepancy. Since we have adopted the same procedure for computing M_B as SSG, the discrepancy between SSG and IMH is presumably also due to this M_B problem. Therefore, one need not assume that SSG are missing weak-lined objects, as IMH have suggested, and the need to invoke luminosity dependent density evolution from $z = 2$ to $z = 4$ is eliminated.

The CCD survey for faint quasars at $4 < z < 5$ covers 0.69 square degrees, just enough area to meaningfully constrain quasar space densities at these magnitudes. Assuming that none of our remaining candidates are high redshift quasars, our results are consistent with a pure density evolution decrease in the number of objects from $z = 2$ to $z = 4$ at faint magnitudes as well. The current coverage of our CCD survey is not enough to significantly constrain quasar clustering at $z \gtrsim 4$. As the number of known quasars at $z > 4$ increases, surveys such as this one will be able to test for such clustering, placing strong constraints on theories of galaxy and structure formation.

The decline in the density of quasars at $z > 3$ could indicate a peak in the quasar population at these redshifts and possibly mark the epoch of peak structure and galaxy formation in the universe. However, Fall & Pei (1993) argue that obscuration by dust could cause optical surveys for quasars at $z = 3$ to miss $10-70\%$ of bright quasars, and at $z > 4$, the number could be as high as 90%. For extreme obscuration, they find that the number of quasars missed could increase by a factor of seven from $z = 2$ to $z = 4$, which is the apparent decrease that we find. As this is their extreme case, dust obscuration could just account for the

decrease that we are seeing. However, their results at $z = 4$ are extrapolations from $z = 3$, making this interpretation even more tentative. None of the $z > 4$ quasars show evidence of appreciable reddening.

Whether this apparent decline in the number of quasars at $z > 3$ is caused by a real decrease in the space density or by obscuration, it is clear that the study of quasars at these epochs will lead to a better understanding of these objects as well as the universe at its earliest stages. To this end, we are continuing the DPOSS search for bright quasars, by following-up candidates in the 27 fields reported here and by covering additional fields. This will provide additional high-z quasars for use as probes in investigations of the universe at redshifts out to $z \sim 4$ such as absorption line and lensing studies, and will allow us to determine quasar space densities at high redshift to a higher accuracy.

We also plan to use the DPOSS quasars as well as the BRI quasars reported in Chapter 4 in targeted searches for quasar clusters and normal galaxies at high redshift, both in the optical and near infrared. The near infrared studies will also yield information about the true rest frame B magnitudes of the quasars, as the K band is roughly equivalent to the rest frame B band. This may lead to a truer determination of the degree of the decline in quasar space densities beyond $z \sim 3$, and will enable determinations of the slopes of our quasar continuua, enabling us to more precisely model the quasar spectra and compute better estimates of their selection probabilities.

We will also continue to obtain spectra for our current CCD candidates. The CCD studies of both Chapter 3 and 4 have demonstrated that large format CCD's will permit us to both determine quasar space densities at faint magnitudes and eventually constrain quasar clustering at high redshift. At least one other survey for faint quasars is underway, and the future will certainly bring others.

We are now beginning a project in collaboration with P. Osmer and M.G. Smith to look for quasars at $z > 5$ by combining the DPOSS gri band data with

z band wide field CCD data. As a compliment to this survey for bright quasars, we are also beginning a multicolor search for faint quasars at $z > 5$ using 4-meter class CCD imaging. Such projects will provide objects with which to study the universe at even greater look back times, and will also help to determine the form of the decline in quasar space densities, hopefully lending clues to its nature.

If the decrease in quasar space densities continues at greater redshifts, larger areas will need to be surveyed in order to determine or constrain their space densities. CCD surveys covering a few square degrees are already feasible, and CCD technology continues to improve. Such surveys will certainly lead to a better determination of the density of quasars at $z \sim 4$ and beyond.

Bibliography

Avni, Y. & Bahcall, J.N. 1980, ApJ, 235, 694

Bahcall, N.A. & Chokshi, A. 1991, ApJ, 380, L9

Bahcall, N.A. & Soneira, R.M. 1983, ApJ, 270, 20

Baldwin, J.A. & Stone, R.P.S. 1984, MNRAS, 206, 241

Bechtold, J., Green, R.F., Weymann, R.J., Schmidt, M., Estabrook, F.B., Sherman, R.D., Wahlquist, H.D., & Heckman, T.M. 1984, ApJ, 281, 76

Boyle, B.J. 1991, in J.D. Barrow, L. Mestel, & P.A. Thomas (ed), *Proc. Texas/ESO-CERN Symposium on Relativistic Astrophysics, Cosmology, and Fundamental Physics*, Ann. NY Acad. Sci., 647, 14

Boyle, B.J., Shanks, T., & Peterson, B.A. 1988, MNRAS, 235, 935

Carico, D.P., Soifer, B.T., & Matthews, K. 1988, AJ, 95, 1599

Chokshi, A. & Turner, E.L. 1992, MNRAS, 259, 421

Cole, S. & Kaiser, N. 1989, MNRAS, 237, 1127

Crampton, D.C. (ed.), 1991, *The Space Distribution of Quasars*, ASPCS, 21

Crampton, D.C., Cowley, A.P., & Hartwick, F.D.A. 1989, ApJ, 345, 59

Cristiani, S., Giallongo, E., Buson, L.M., Gouiffes, C., & La Franca, F. 1993, A&A, 268, 86

Dalton, G.B., Croft, R.A.C., Efstathiou, G., Sutherland, W.J., Maddox, S.J., & Davis, M. 1994, MNRAS, 271, L47

Darling, J., de Carvalho, R.R., Kennefick, J.D., & Djorgovski, S.G. 1996, BAAS, submitted

Djorgovski, S., Lasker, B., Weir, N., Postman, M., Reid, I.N., & Laidler, V. 1992a, BAAS, 24, 750

Djorgovski, S., Smith, J.D., & Thompson, D.J. 1991, in D. Crampton (ed.), The Space Distribution of Quasars, ASPCS, 21, 325

Djorgovski, S., Thompson, D., & Smith, J.D. 1992b, in B. Rocca-Volmerange, B. Guiderdoni, M. Dennefeld, J. Tran Thanh Van (eds.), First Light in the Universe: Stars or QSO's?, Proceedings of the eighth IAP Astrophysics Meeting, 67

Efstathiou, G. & Rees, M.J. 1988, MNRAS, 230, 5

Fall, S.M. & Pei, Y.C. 1993, ApJ, 402, 479

Foltz, C.B., Chaffee, F.H., Hewett, P.C., MacAlpine, G.M., Turnshek, D.A., Weymann, R.J., & Anderson, S.F. 1987, AJ, 94, 1423

Giallongo, E. & Cristiani, S. 1990, MNRAS, 247, 696

Haehnelt, M.G. & Rees, M.J. 1993, MNRAS, 263, 168

Hagen, H.J., Cordis, L., Engels, D., Groote, D., Haug, U., Heber, U., Kohler, Th., Wisotzki, L., & Reimers, D. 1992, AA, 253, L5

Hall, P.B., Osmer, P.S., Green, R.F., Porter, A.C., & Warren, S.J. 1996, ApJS, submitted

Hamuy, M., Walker, A.R., Suntzeff, N.B., Gigoux, P., Heathcote, S.R., & Phillips, M.M. 1992, PASP, 104, 533

Hartwick, F.D.A. & Schade, D. 1990, ARAA, 28, 437

Hawkins, M.R.S. & Véron, P. 1993, MNRAS, 260, 202

Hawkins, M.R.S. & Véron, P. 1995, MNRAS, 275, 1102

Henry J.P. et al. 1994, AJ, 107, 1270

Hewett, P.C. & Foltz, C.B. 1994, PASP, 106, 113

Hewett, P.C, Foltz, C.B., & Chaffee, F.H. 1993, ApJ, 406, L43

Hook, I.M., McMahon, R.G., Boyle, B.J., & Irwin, M.J. 1994, MNRAS, 268, 305

Hoyle, F. & Fowler, W.A. 1963, Nat, 197, 533

Iovino, A., Shaver, P.A., & Cristiani, S. 1991, in D. Crampton (ed.), *The Space Distribution of Quasars*, ASPCS, 21, 202

Irwin, M. & McMahon, R. 1990, RGO, Gemini #30, 6

Irwin, M., McMahon, R., & Hazard, C. 1991, in D. Crampton (ed.), *The Space Distribution of Quasars*, ASPCS, 21, 117

Jarvis, J. & Tyson, J. 1979, *SPIE Proc. on Instrumentation in Astronomy IV*, 172, 422

Kaiser, N. 1984, ApJ, 284, L9

Katz, N., Quinn, T., Bertschinger, E., & Gelb, J.M. 1994, MNRAS, 270, L71

Kennefick, D. 1996a, Ph.D. thesis, California Institute of Technology

Kennefick, J.D., Djorgovski, S.G., & Meylan, G. 1996b, AJ, submitted

Kennefick, J.D., de Carvalho, R.R., Djorgovski, S.G., Wilber, M.M., Dickson, E.S, Weir, N., Fayyad, U., & Roden, J. 1995a, AJ, 110, 78

Kennefick, J.D., Djorgovski, S.G., & de Carvalho, R.R. 1995b, AJ, in press

Kent, S.M. 1985, PASP, 97, 165

Koo, D.C. & Kron, R.G. 1982, AA, 105, 107

Landolt, A.U. 1992, AJ, 104, 340

Lasker, B., Djorgovski, S., Postman, M., Laidler, V., Weir, N., Reid, I.N., & Sturch, C. 1992, BAAS, 24, 741

Lu, L., Sargent, W.L.W., & Womble, D.S. 1996, in preparation

Lu, L., Wolfe, A.M., & Turnshek, D.A. 1991, ApJ, 367, 19

Lynden-Bell, D. 1969, Nat, 223, 690

Martinez, V.J. & Coles, P. 1994, ApJ, 437, 550

Mathez, G. 1978, AA, 68, 17

McCarthy, P.J., Dickinson, M., Filippenka, A.V., Spinrad, H., & van Breugel, W.J.M. 1988, ApJ, 328, L29

McMahon, R.G., Omomt, A., Bergeron, J., Kreysa, E., & Haslan, C.G.T. 1994 MNRAS, 267, L9

Moller, P. & Warren, S. 1991, in D. Crampton (ed.), *The Space Distribution of Quasars*, ASPCS, 21, 96

O'Brien, P.T., Gondhalekar, P.M., & Wilson, R. 1988, MNRAS, 233, 801

Oke, J.B. 1974, ApJS, 27, 21

Oke, J.B. & Gunn, J.E. 1983, ApJ 266, 713

Oke, J.B. & Korycanski, D.G. 1982, ApJ, 255, 11

Osmer, P.S. 1982, ApJ, 253, 28

Osmer, P.S., Green, R.F., Hall, P.B., Porter, A.C., & Warren, S.J. 1996, ApJ, submitted

Peebles, P.J.E. 1980, *The Large-Scale Structure of the Universe*, Princeton Univ. Press

Peebles, P.J.E .1993, *Principles of Physical Cosmology*, Princeton Univ. Press

Rees, M.J. 1992, in B. Rocca-Volmerange, B. Guiderdoni, M. Dennefeld, J. Tran Thanh Van (eds.), First Light in the Universe: Stars or QSO's?, Proceedings of the eighth IAP Astrophysics Meeting, 203

Reid, I.N. et al. 1991, PASP, 331, 465

Reid, I.N. & Djorgovski, S. (for the POSS-II photographic and digital survey teams) 1993, in B.T. Soifer (ed.), *Sky Surveys: Protostars to Protogalaxies*, ASPCS, 43, 125

Robinson, I., Schild, A., & Schucking, E.L. (eds.) 1965, *Quasi-Stellar Sources and Gravitational Collapse*, University of Chicago Press

Rowan-Robinson, M., Efstathiou, A., Lawrence, A., Oliver, S., Taylor, A., Broadhurst, T.J., McMahon, R.G., Benn, C.R., Condon, J.J., Lonsdale, C.J., Hacking, P., Conrow, T., Saunders, W.S., Clements, D.L., Ellis, R.S., & Robson, I. 1993, MNRAS, 261, 513

Sandage, A. 1965, ApJ, 141, 1560

Sandage, A. & Luyten, W.J. 1967, ApJ, 148, 767

Sandage, A. & Véron, P. 1965, ApJ, 142, 412

Schmidt, M. 1963, Nat, 197, 1040

Schmidt, M. 1968, ApJ, 151, 393

Schmidt, M. & Green, R. 1983, ApJ, 269, 352

Schmidt, M., Schneider, D.P., & Gunn, J.E. 1987, ApJ, 321, L7

Schmidt, M., Schneider, D.P., & Gunn, J.E. 1995, AJ, 110, 68

Schneider, D.P., Schmidt, M., & Gunn, J.E. 1989, AJ, 98, 1507

Schneider, D.P., Schmidt, M., & Gunn, J.E. 1991a, AJ, 101, 2004

Schneider, D.P., Schmidt, M., & Gunn, J.E. 1991b, AJ, 102, 837

Schneider, D.P., Schmidt, M., & Gunn, J.E. 1994, AJ, 107, 1245

Shaver, P.A. 1995, in H. Bohringer et al. (eds.), *17th Texas Symposium on Relativistic Astrophysics and Cosmology*, Ann. New York Academy of Science

Small, T.A. & Blandford, R.D. 1992, MNRAS, 259, 725

Smith, J.D., Thompson, D., & Djorgovski, S. 1994a, AJ, 107, 24

Smith, J.D., Djorgovski, S., Thompson, D., Brisken, W., Neugebauer, G., Matthews, K., Meylan, G., Piotto, G., & Suntzeff, N. 1994b, AJ, 108, 1147

Smith, J.D., Thompson, D., & Djorgovski, S. 1993, in B. T. Soifer (ed.), Sky Surveys: Protostars to Protogalaxies, ASPCS, 43, 189

Steidel, C.C., & Sargent, W.L.W. 1987, ApJ, 313, 171

Stetson, P.B., 1987, PASP, 99,191

Stone, R.P.S. 1974, ApJ 193, 135

Stone, R.P.S. & Baldwin, J.A. 1983, MNRAS, 204, 347

Storrie-Lombardi, L.J. 1994, Ph.D. thesis, Cambridge University

Storrie-Lombardi, L.J., McMahon, R.G., Irwin, M.J., & Hazard, C. 1994, ApJ, 427, L13

Thompson, D. 1995, Ph.D. thesis, California Institute of Technology

Thompson, D., Djorgovski, S., & Trauger, J. 1995, AJ, 110, 963

Thuan, T.X. & Gunn, J. 1976, PASP, 88,543

Trevese, D., Pittella, G., Kron, R.G., Koo, D.C., & Bershady, M. 1989, AJ, 98, 108

Turner, E.L. 1991, AJ, 101, 5

Turnshek, D.A. 1988, in J.C. Blade, D.A. Turnshek, & C.A. Norman (eds.), *QSO Absorption Lines: Probing the Universe*, *STScI Symp. Series*, Cambridge University Press, 17

Usher, P.D. & Mitchell, K.J. 1978, ApJ, 223, 1

Valdes, F. 1982, *SPIE Proc. on Instrumentation in Astronomy IV*, 331,465

Warren, S.J. & Hewett, P.C. 1990, Rep. Prog. Physics, 53, 1095

Warren, S.J., Hewett, P.C., Irwin, M.J., McMahon, R.G., Bridgeland, M.T., Bunclark, P.S., & Kibblewhite, E.J. 1987a, Nat, 325, 131

Warren, S.J., Hewett, P.C., Irwin, M.J., & Osmer, P.S. 1991a, ApJS, 76, 1

Warren, S.J., Hewett, P.C., & Osmer, P.S. 1991b, ApJS, 76, 23

Warren, S.J., Hewett, P.C., & Osmer, P.S. 1994, ApJ, 421, 412

Warren, S.J., Hewett, P.C., Osmer, P. S., & Irwin, M. J. 1987b, Nat, 330, 453

Webb, J.K., Parnell, H.C., Carswell, R.F., McMahon, R.G., Irwin, M.J., Hazard, C., Ferlet, R., & Vidal-Madjar, A. 1988, The Messenger, 51, 15

Weir, N. 1994, Ph.D. thesis, California Institute of Technology

Weir, N., Fayyad, U.M., & Djorgovski, S. 1995a, AJ, 109, 2401

Weir, N., Djorgovski, S., & Fayyad, U.M. 1995b, AJ, 110, 1

Weir, N., Djorgovski, S., Fayyad, U., & Roden, J. 1995c, PASP, in press

Wilkes, B.J. 1986, MNRAS, 218, 331

Williger, G.M., Baldwin, J.A., Carswell, R.F., Cooke, A.J., Hazard, C., Irwin, M.J., McMahon, R.G., Storrie-Lombardi, L., 1994, ApJ, 428, 574

Zuo, L. & Lu, L. 1993, ApJ, 418, 601